MONTANA STATE UNIVERSITY

Measuring surface temperature of isolated neutron stars and related problems
by Marcus Alton Teter

A dissertation submitted in partial fulfillment of the requirements for the degree of Doctor of Philosophy in Physics
Montana State University

Abstract:
New and exciting results for measuring neutron star surface temperatures began with the successful launch of the Chandra X-ray observatory. Among these results are new detections of neutron star surface temperatures which have made it possible to seriously test neutron star thermal evolution theories. The important new temperature determination of the Vela pulsar (Pavlov, et al., 2001a) requires a non-standard cooling scenario to explain it.

Apart from this result, we have measured PSR B1055-52's surface temperature in this thesis, determining that it can be explained by standard cooling with heating. Our spectral fit of the combined data from ROSAT and Chandra have shown that a three component model, two thermal blackbodies and an non-thermal power-law, is required to explain the data. Furthermore, our phase resolved spectroscopy has begun to shed light on the geometry of the hot spot on PSR B1055-52's surface as well as the structure of the magnetospheric radiation. Also, there is strong evidence for a thermal distribution over its surface. Most importantly, the fact that PSR B1055-52 does not have a hydrogen atmosphere has been firmly established.

To reconcile these two key observations, on the Vela pulsar and PSR B1055-52, we tested neutron star cooling with neutrino processes including the Cooper pair neutrino emission process. Overall, it has been found that a phase change associated with pions being present in the cores of more massive neutron stars explains all current of the data. A transition from neutron matter to pion condensates in the central stellar core explains the difference between standard and non-standard cooling scenarios, because the superfluid suppression of pion cooling will reduce the emissivity of the pion direct URCA process substantially. A neutron star with a mass of 1.2M with a medium stiffness equation of state and a T72 type neutron superfluid models the standard cooling case well. A neutron star of 1.4M, with a pion core, with the same type of equation of state modified for pion matter and a modified El-0.6 pion superfluid model is the best option for the non-standard case. The results also suggest that the equation of state for neutron stars may have to be stiffer than medium.

Furthermore, our observational results from two other sources, SGR 1900+14 and 1E1207.4-5209, have helped us to expand the understanding of isolated neutron stars. The Chandra observation of SGR 1900+14 has strengthened the case that it is a magnetar, as the pulsed fraction and the spectral fits suggest a blackbody plus power-law model is prefered. Also, our analysis of the Chandra data of 1E1207.4-5209 suggests that it should have a hydrogen atmosphere. Future observations will certainly give even better insight to both of these objects, as well as PSR B1055-52.

MEASURING SURFACE TEMPERATURE OF ISOLATED NEUTRON STARS AND RELATED PROBLEMS.

by

Marcus Alton Teter

A dissertation submitted in partial fulfillment
of the requirements for the degree

of

Doctor of Philosophy

in

Physics

MONTANA STATE UNIVERSITY — BOZEMAN
Bozeman, Montana

December 2001

APPROVAL

of a dissertation submitted by

Marcus Alton Teter

This dissertation has been read by each member of the dissertation committee, and has been found to be satisfactory regarding content, English usage, format, citations, bibliographic style and consistency, and is ready for submission to the College of Graduate Studies.

Sachiko Tsuruta, Ph. D. _____ 12/3/2001
(Signature) Date

Approved for the Department of Physics

John C. Hermanson, Ph. D. _____ 12-3-01
(Signature) Date

Approved for the College of Graduate Studies

Bruce R. McLeod, Ph. D. _____ 12-10-01
(Signature) Date

STATEMENT OF PERMISSION TO USE

In presenting this dissertation in partial fulfillment of the requirements for a doctoral degree at Montana State University — Bozeman, I agree that the Library shall make it available to borrowers under rules of the Library. I further agree that copying of this thesis is allowable only for scholarly purposes, consistent with "fair use" as prescribed in the U. S. Copyright Law. Requests for extensive copying or reproduction of this thesis should be referred to University Microfilms International, 300 North Zeeb Road, Ann Arbor, Michigan, 48106, to whom I have granted "the exclusive right to reproduce and distribute my dissertation in and from microform along with the non-exclusive right to reproduce and distribute my abstract in any format in whole or in part."

Signature M. a. Peterson

Date 3 DEC 2001

ACKNOWLEDGEMENTS

I would like to thank Dr. G. Pavlov at The Pennsylvania State University department of Astronomy for his advise on the *Chandra* data analysis.

This research was sponsored in part by SAO grants GO0-1131A and GO0-1012X.

TABLE OF CONTENTS

1 INTRODUCTION 1

2 *CHANDRA* X-RAY OBSERVATORY 12
Introduction 12
Data Reduction 14

3 *CHANDRA* OBSERVATION OF PSR B1055-52 20
Introduction 20
Previous Observations and Results 20
Our *Chandra* Observation and Data Reduction 24
Our Results 26
One-Dimensional Spatial Results 26
Timing Results 28
Phase Integrated Spectral Analysis 31
Phase Resolved Spectroscopy 41
Discussion 45

4 *CHANDRA* OBSERVATIONS OF SGR 1900+14 51
Introduction 51
Magnetars 51
Soft Gamma-ray Repeaters(SGR) 52
Previous Outbursts of SGR 1900+14 53
April 2001 Event 54
Our Results 55
Our Timing Results 56
Our Phase Integrated Spectral Analysis 63

Our Phase Resolved Spectral Analysis 66
Discussion 68

5 *CHANDRA* OBSERVATIONS OF 1E1207.4-5209 72
Introduction 72
Earlier Observations and Results 73
Chandra Observation and Previous Results 73
Our New Results from the *Chandra* Observation 74
Results of Our Timing Analysis 75
Results of Our Phase Integrated Spectral Analysis 75
Results of Our Phase Resolved Spectral Analysis 78
Discussion 79

6 FUTURE OBSERVATIONS 83
Future Missions 83
Future Observations of Neutron Stars 83

7 COOPER PAIR NEUTRINO EMISSIVITY AND COOLING OF NEUTRON STARS 86
Introduction 86
Theoretical Background 87
Standard Neutrino Emission Mechanisms 89
Non-standard Neutrino Emission Mechanisms 90
Cooper Pair Neutrino Emission Mechanisms 92
Superfluid Models 97
Effects Upon Standard Cooling 99
Effects Upon Non-Standard Cooling 101
Discussion 108

8 SUMMARY 114
BIBLIOGRAPHY 119

LIST OF TABLES

1.1 List of isolated neutron star detections and a sample of upper limits. Numbered sources are detections, and lettered sources are upper limits. 5

1.2 Listing of standard and non-standard neutrino emission processes. . 6

3.1 Summary of X-ray spectral results from previous observations. OF93 used *ROSAT* PSPC data only, while all others used a combined *ROSAT* PSPC and *ASCA* SIS data set. 23

3.2 Summary of X-ray spectral results from combined *ROSAT* and *Chandra* analysis using models from previous work. A single blackbody component is labeled as BB, and a single power-law component is labeled as PO. The hydrogen column density is n_H. The soft blackbody apparent temperature are labeled kT_S and radius R_S. Similarly, the values for the hard blackbody are labeled with kT_H and R_H. The power-law index is Γ, and the power-law normalization is N_Γ. The fit statistic is χ^2, the degrees of freedom is d.o.f., and $\chi^2_\nu = \chi^2/\text{d.o.f.}$. . . 33

3.3 Summary of X-ray spectral results from combined *ROSAT* and *Chandra* analysis using 3 component model. 36

3.4 Summary of X-ray spectral results from phase resolved *Chandra* analysis using 3 component model, case 1. The fixed parameters are n_H=1.3 $\times 10^{20} cm^{-2}$, R_s=11.6 km at 1 kpc, kT_H=0.14 keV , and Γ=1.66. . . 42

3.5 Summary of X-ray spectral results from phase resolved *Chandra* analysis using 3 component model, case 2. The fixed parameters are n_H=1.3 $\times 10^{20} cm^{-2}$, kT_s=72 eV, R_H=0.82 km at 1 kpc , and Γ=1.66. 42

4.1 Single power-law fit for both observations. The values in the parenthesis are best fit values using the fixed $n_{H,22}$ value from the combined fit. 64

4.2 Blackbody plus power-law fit for both observations. As before, the values in the parenthesis are for the best fit values using the fixed value for $n_{H,22}$ 67

4.3 Phase resolved spectral results for power-law model with $n_{H,22}$ fixed at the phase integrated value of 2.85. 67

LIST OF FIGURES

1.1 Standard cooling curve including the current detections (numbers) and upper limits (letters). See table 1.1 for description of the data. The standard cooling curve is for a $1.4M_{\odot}$ neutron star with an FP EOS and a T72 superfluid model. 4

2.1 *Chandra* CC mode image of 1E1207.4-5209 without correction for spacecraft dither and SIM motion. The image is a negative linear grey scale. The horizontal scale is position at 0.″5 per pixel, and the vertical is time at 2.8 ms per pixel. 16

2.2 *Chandra* CC mode image of 1E1207.4-5209 with correction for spacecraft dither and SIM motion. 17

3.1 One dimensional continuous clocking (CC) mode image of PSR B1055-52. 27

3.2 Z_1^2 (Rayleigh) statistic as a function of frequency for the *Chandra* data set near the radio ephemeris. 29

3.3 Energy resolved light curves of the *Chandra* observation. 30

3.4 Pulsed fraction as a function of energy for the *Chandra* observation . 32

3.5 Results from PSR B1055-52 combined *ROSAT* and *Chandra* analysis using a two component model, two blackbodies. Notice the deviation of high energy photons in the residual. 34

3.6 PSR B1055-52 combined *ROSAT* and *Chandra* analysis using 2 component, blackbody plus power-law with fixed index, Γ=1.5. The distinctive sinusoidal distribution of the residuals indicate a poor fit. . . 35

3.7 Results from our PSR B1055-52 combined *ROSAT* PSPC and *Chandra* ACIS-S3 analysis using three component, two blackbodies plus power-law, model. The top panel shows the raw *ROSAT* (low energy) and *Chandra* (high energy) data sets. The middle panel shows the residual for the fit. The lower panel shows the unfolded spectra with telescope response taken into account. The 3 curves are the soft blackbody component (long dash), the hard blackbody component (dash), and the power-law component (dot). The sum of the three components is the solid line. 38

3.8 Confidence contours for soft blackbody for phase integrated spectrum. The contours are for $n_{H,20}$ versus kT_S and R_S versus kT_S, where $n_{H,20}$ = n_H /10^{20} cm^{-2} and R_S is the soft blackbody radius in km at 1 kpc. The contours are 1 (inner), 1.6 (middle) and 2.6 σ (outer) using a 3 parameter fit. 39

3.9 Confidence contours for the hard blackbody and power-law normalization for the phase integrated spectrum. The contours are for N_Γ versus kT_H and R_H versus kT_H. Again, the contours are using a 3 parameter fit. 40

3.10 Phase resolved spectroscopy results case 1. The fixed parameters are labeled within the panels. The hydrogen column density, n_H was fixed at a value of 1.3 $\times 10^{20} cm^{-2}$. 43

3.11 Phase resolved spectroscopy results case 2. Again, the hydrogen column density, n_H was fixed at a value of 1.3 $\times 10^{20} cm^{-2}$. 44

3.12 Phase variation of blackbody bolometric fluxes (Case I). For the blackbody components the flux was computed by fixing the other parameters to their best fit values for each phase. The errors in the flux were estimated from a χ^2_{min} + 1 contour for the model component. The cgs units are ergs s^{-2} cm^{-2}. 46

3.13 Phase variation of blackbody bolometric fluxes (Case II). See caption for figure 3.12 for details. 47

4.1 Comparison between first (top panel) and second (bottom panel) observation's Z_1^2 statistic. Both are compared to the best fit frequency for observation 1, $f_{0,1} = 0.1933143^{+1.0e-06}_{-1.3e-06}$ Hz. Note the slight shift for the second observation. 57

4.2 Light curve for the first *Chandra* observation. 58

4.3 Light curve for the second *Chandra* observation. 59

4.4 Energy resolved light curves for the first *Chandra* observation. There are insufficient counts below 1 keV and above 8 keV. 60

4.5 Energy resolved light curves for the second *Chandra* observation. The reduction of the observation time leads to an increase of uncertainty. 61

4.6 Energy resolved pulsed fraction for both of the *Chandra* observations. Notice the significant change in the 4-5 keV range. 63

4.7 Combined fit of both *Chandra* observations with a single power-law model. 65

4.8 Combined fit of both *Chandra* observations with a blackbody plus power-law model. 66

5.1 The spectrum of 1E1207.4-5209 *Chandra* data shows the absorption feature which prevented fitting. There is a large deviation in the residual in the range 1.2-1.5 keV. 76

5.2 Fit of absorption edge model for 1E1207.4-5209. The last data point shows the beginning of the background dominated region, but was ignored for fitting purposes. The edge can be seen in the top panel where the best fit line steps down. 78

5.3 Phase resolved spectral fits for 1E1207.4-5209 . The cgs units of flux is erg $s^{-1}cm^{-2}$. The blackbody radius assumes a distance of 15 kpc. 80

7.1 Neutrino emissivity for neutron superfluidity of types A, B, and C. The superfluid critical temperature is chosen to be $T_n^{cr} = 10^9$ K, and the Cooper pair emission mechanism is shut down beyond T_n^{cr} because of no superfluidity above the critical temperature. 95

7.2 Comparison between modified URCA and type B superfluid with superfluid critical temperature of $T_n^{cr} = 10^9$ K. 96

7.3 Comparison between several example superfluid models. For reference nuclear density is 2.8×10^{14} (g cm^{-3}). The models with solid lines are for pions, while all others are neutron $^3P_2$ superfluids. 98

7.4 Standard cooling is shown for a $1.4M_\odot$, FP EOS star with a T72 superfluid. The solid line is the standard cooling curve. The dashed line is the standard cooling including the Cooper pair neutrino emissivity. See figure 1.1 and table 1.1 for summary of data points. 101

7.5 Standard cooling is shown for a $1.4M_\odot$ star with a PS EOS and a T72 superfluid. The solid line is the standard cooling curve. The dashed line is the standard cooling including the Cooper pair neutrino emissivity. See figure 1.1 and table 1.1 for summary of data points. . 102

7.6 Pion cooling with E1 superfluid model a $1.4M_\odot$ star with for the FP EOS. The dotted curve is for standard cooling for a star with $1.4M_\odot$ FP EOS and a T72 superfluid model without Cooper pair emission. The dashed curve is the E1 superfluid suppression for pion cooling with the LM factor $\tilde{g}' = 0.6$ without the Cooper pair effect. The solid curve includes the effect of Cooper pair neutrino emission on pion cooling. See figure 1.1 and table 1.1 for summary of data points. 107

7.7 Pion cooling with the modified E1 superfluid model a star with the pion FP EOS and $1.4M_\odot$. The heavy solid curve is for standard cooling with a T72 superfluid and $1.2M_\odot$, including Cooper pair emission. The other curves are for nonstandard (pion) cooling with the LM, $\tilde{g}' = 0.6$. Each curve represents a different value of ΔT: dotted (ΔT=0), long dashed (ΔT=0.2), chain (ΔT=0.4), dashed (ΔT=0.6), and solid (ΔT=0.8). 109

7.8 Interior temperatures of non-standard and standard cooling as a function of internal density. The labels are the age in log (years). See text for explanation. 110

7.9 Comparisons between equations of state. The critical density for pions, ρ_{crit}, establishes the correct equation of state for neutron stars with masses near $1.4M_{\odot}$. EOSs become unstable when their masses begin to decrease with increasing density. 112

ABSTRACT

New and exciting results for measuring neutron star surface temperatures began with the successful launch of the *Chandra* X-ray observatory. Among these results are new detections of neutron star surface temperatures which have made it possible to seriously test neutron star thermal evolution theories. The important new temperature determination of the Vela pulsar (Pavlov, et al., 2001a) requires a non-standard cooling scenario to explain it.

Apart from this result, we have measured PSR B1055-52's surface temperature in this thesis, determining that it can be explained by standard cooling with heating. Our spectral fit of the combined data from *ROSAT* and *Chandra* have shown that a three component model, two thermal blackbodies and an non-thermal power-law, is required to explain the data. Furthermore, our phase resolved spectroscopy has begun to shed light on the geometry of the hot spot on PSR B1055-52's surface as well as the structure of the magnetospheric radiation. Also, there is strong evidence for a thermal distribution over its surface. Most importantly, the fact that PSR B1055-52 does not have a hydrogen atmosphere has been firmly established.

To reconcile these two key observations, on the Vela pulsar and PSR B1055-52, we tested neutron star cooling with neutrino processes including the Cooper pair neutrino emission process. Overall, it has been found that a phase change associated with pions being present in the cores of more massive neutron stars explains all current of the data. A transition from neutron matter to pion condensates in the central stellar core explains the difference between standard and non-standard cooling scenarios, because the superfluid suppression of pion cooling will reduce the emissivity of the pion direct URCA process substantially. A neutron star with a mass of $1.2M_{\odot}$ with a medium stiffness equation of state and a T72 type neutron superfluid models the standard cooling case well. A neutron star of $1.4M_{\odot}$, with a pion core, with the same type of equation of state modified for pion matter and a modified E1-0.6 pion superfluid model is the best option for the non-standard case. The results also suggest that the equation of state for neutron stars may have to be stiffer than medium.

Furthermore, our observational results from two other sources, SGR 1900+14 and 1E1207.4-5209, have helped us to expand the understanding of isolated neutron stars. The *Chandra* observation of SGR 1900+14 has strengthened the case that it is a magnetar, as the pulsed fraction and the spectral fits suggest a blackbody plus power-law model is prefered. Also, our analysis of the *Chandra* data of 1E1207.4-5209 suggests that it should have a hydrogen atmosphere. Future observations will certainly give even better insight to both of these objects, as well as PSR B1055-52.

CHAPTER 1

INTRODUCTION

The ability of measuring an isolated neutron star surface temperature has become a much easier task in recent years, because of the improvements in the orbiting observatories. The original *EINSTEIN* observatory, launched in 1978, gave the first indication of neutron star surface temperatures. It established upper temperature limits for many neutron stars, and created the first hope of beginning to reconcile theory with observation (e.g. Nomoto & Tsuruta 1981, 1986). Later, with the launch of *ROSAT*, the Röntgen Satellite developed mainly by Germany, the United States and the United Kingdom which was launched in 1990, three convincing detections were made for pulsars PSR B0656+14, PSR B1055-52, and Geminga. Afterwards, a few more neutron star's surface temperature measurements followed with the launch of *ASCA*, the fourth Japanese X-ray astronomy mission launched in 1993, and ground based optical telescopes. Finally, the introduction of *Chandra*, detailed in chapter 2, and *XMM-Newton*, the European Space agency's X-ray multi-mirror satellite, have improved the detection capabilities beyond all previous levels.

Neutron stars are thought to be born in supernova explosions. They are what

remains of the core of the progenitor star. If the core is above a certain mass, which remains uncertain but is estimated to be $\sim$2-3$M_{\odot}$, the core will collapse into a black hole; otherwise, a neutron star is formed. The neutron star will begin life at extremely high temperatures, with core temperatures as high as $\sim 10^{10-11}$ K, and cool off by various mechanisms.

The importance of detecting a neutron star's surface temperature relates to their thermal evolution. A neutron star first cools via various neutrino emission mechanisms, from the interior of the star, before the photon radiation from the surface becomes the dominant cooling process (Tsuruta, 1979). The first thermal evolution calculations (Tsuruta, 1964) showed that a neutron star should be visible as an X-ray source for about a million years. Among the important factors which seriously affect the nature of thermal evolution are the neutrino emission processes, the superfluidity of the core particles, the composition, and the mass of the neutron star.

The conventional neutrino cooling mechanisms, adopted in the earlier and most of the subsequent cooling calculations, such as the modified URCA, plasmon neutrino and bremsstrahlung processes, are called 'standard' cooling. On the other hand, the more exotic and extremely fast cooling processes, such as the URCA process involving pions, kaons, and quarks, and the direct URCA process involving nucleons and hyperons, are called 'nonstandard' processes (Tsuruta, 1998).

Once all neutrino cooling rates have decreased below the surface photon cooling rate, the photon cooling from the surface of the star takes over, dictating the remainder of the thermal evolution. Even though at earlier times the neutrino mechanisms

control the thermal evolution, the neutron star will emit photons from its surface. Consequently, through much of their earlier thermal history, neutron stars should remain visible as X-ray sources.

Measuring an isolated neutron star's temperature becomes important to test various thermal evolution theories. If a neutron star cools slowly through the standard cooling, its surface temperature will be higher than if it cools rapidly through non-standard cooling. Overall, early upper limits and detections showed that the standard cooling process would explain all the data, except for the Vela pulsar's upper limit. Later, as more observed temperatures became available, possible exceptions to standard cooling began to be discussed. Although, thermal evolution has been primarily a theoretical problem for many years, dating back to the nineteen-sixties (Tsuruta, 1964). It has only recently become a serious observational problem, with the addition of many more detections.

Figure 1.1 shows a typical standard cooling curve along with upper limits and detections of various isolated neutron stars. The upper limits shown here are mostly from *ROSAT* and combined *ROSAT* and *ASCA* observations. For RCW 103, both the upper limit based upon earlier *EINSTEIN* observation (c) and the new upper limit based upon new results (c*) using *XMM-Newton* (Slane, 2001) are shown. In addition to the original three detections, PSR B1055-52 (6), PSR B0656+14 (4), and Geminga (5), additional new detections have been established. The new point, Vela (3) from the *Chandra* observation, together with the new RCW 103 upper limit (c*) are the most important addition to the detection list, as its surface temperature

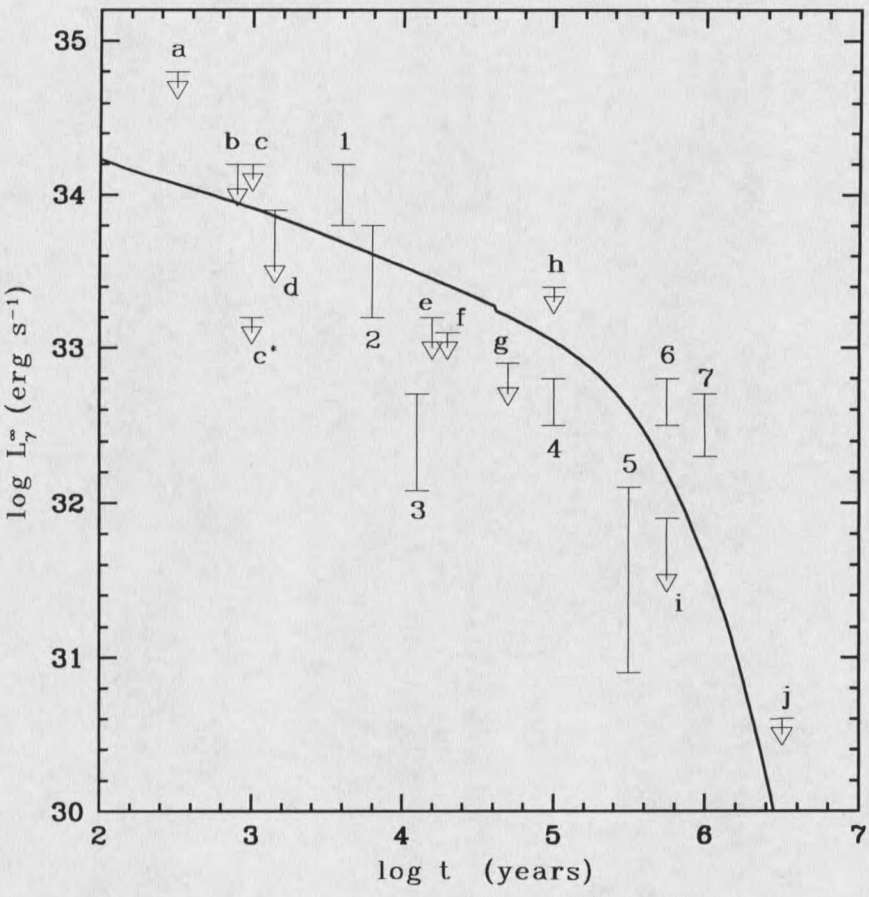

Figure 1.1: Standard cooling curve including the current detections (numbers) and upper limits (letters). See table 1.1 for description of the data. The standard cooling curve is for a $1.4M_\odot$ neutron star with an FP EOS and a T72 superfluid model.

makes it an important candidate for non-standard cooling. The point source in Cas A (a), is included as an upper limit, even though the case for Cas A being a neutron star is far from certain (e.g. Pavlov et al, 2000, Umeda et al, 2000). Table 1.1 gives a summary of all the detections and upper limits.

The cooling curves are made using our 'exact' evolutionary code, where no isothermal approximation is made. This differs from isothermal codes because it includes the finite time scale of thermal conduction through the neutron star crust. The conduc-

Table 1.1: List of isolated neutron star detections and a sample of upper limits. Numbered sources are detections, and lettered sources are upper limits.

Source	Name	Reference
1	RX J0822-43	Zavlin, Trümper, & Pavlov, 1999
2	1E1207.4-5209	Zavlin, Pavlov & Trümper, 1998
3	Vela	Pavlov et al., 2001a
4	PSR B0656+14	Becker, 1995
5	Geminga	Becker, 1995
6	PSR B1055-52	Ögelman & Finley, 1993
7	PSR RX J185635-3754	Walter, Wolk, & Neuhäuser, 1996
a	Cas A point source	Pavlov et al., 2000
b	Crab pulsar	Becker, 1995
c	RCW 103	Tuohy & Garmire, 1980
c*	RCW 103	Slane, 2001
d	PSR B1509-58	Becker, 1995
e	PSR B1706-44	Becker, 1995
f	PSR B1823-13	Finley, Srinivasan, & Park, 1993
g	PSR B2234+61	Becker, 1995
h	PSR B1951+32	Becker, 1995
i	PSR B0355+54	Becker, 1995
j	PSR B1929+10	Becker, 1995

tion time scale depends upon the neutron star model of the equation of state (EOS) detailing the pressures associated with the strong nuclear force. For the softest EOS, BPS (Baym, Pethick & Sutherland, 1971), the conduction time scale is $\sim$100 years. For the FP (Friedman and Pandharipande, 1981) EOS, which is of medium stiffness, it is $\sim$1000 years. For the PS (Pandharipande, Pines & Smith, 1976) EOS, for stiff matter, it is up to $\sim 10^4$ years. The cooling curves for the exact and the isothermal codes converge after those times. At present various neutron star EOSs are available (e.g. Wiringa, Fiks, & Fabrocini, 1988, and Nishizaki, Takatsuka, & Hiura, 1994), but we chose BPS, FP, and PS as representative EOSs for comparison to previous

results (e.g. Tsuruta, 1998).

Table 1.2 gives a listing of the standard and non-standard neutrino processes. The standard cooling is dominated by the modified URCA neutrino process (Friman

Table 1.2: Listing of standard and non-standard neutrino emission processes.

Standard	Non-standard
Modified URCA	Direct URCA (nucleons)
n-n bremsstrahlung	Pion URCA
n-p bremsstrahlung	Kaon URCA
plasmon neutrino	Hyperon URCA
Nuclear URCA	Quark URCA
e^--heavy ion bremsstrahlung	
e^--e^+ pair neutrino	
photo-neutrino	

and Maxwell, 1979, FM79 hereafter). The other processes are the neutron-neutron neutrino bremsstrahlung, neutron-proton neutrino bremsstrahlung (FM79), nuclear URCA (Tsuruta and Cameron, 1965), the electron-heavy ion neutrino bremsstrahlung (Itoh and Kohyama, 1984), and the plasmon neutrino, photo-neutrino, and electron-positron pair neutrino processes (Munakata et al., 1985). Overall, the modified URCA, and the neutron-neutron and neutron-proton neutrino bremsstrahlung processes in the central core produce the highest neutrino emissivity, though all of the standard cooling processes are accounted for in the cooling code used for this work. However, during the earliest stage of cooling when the information on the cooling in the central core has yet to be transmitted to the surface due to the finite time scale of thermal conduction, the surface cools due to the plasmon neutrino, the nuclear

URCA, and the electron-heavy ion bremsstrahlung processes operating in the inner crust.

The non-standard cooling has many options depending upon the composition of the core of a neutron star. By assuming the core is entirely nucleons with sufficiently high proton concentration, the validity of the direct URCA process for nucleons is pointed out (Lattimer et al., 1991). If the core is composed of pions, then the pion direct URCA process can take place (Muto, et al. 1988). Similarly, if kaons or quark matter is present, then corresponding kaon or quark direct URCA process is possible (Tatsumi, 1988 and Iwamoto, 1980).

To match the new observations, the choice of non-standard cooling has to be made; however, all of the non-standard cooling scenarios cool entirely too fast to be considered without some sort of suppression of their rates (e.g. Tsuruta, 1998). Fortunately, the core of neutron stars are expected to be in a superfluid state. Unlike terrestrial superfluids, under the ultra-high densities present in neutron star cores that are higher than the density of an atomic nucleus, the temperature is relatively high when core particles become superfluid. Typical superfluid critical temperatures, T_{cr}, below which superfluidity sets in, occurs in some cases at $T_{cr} \sim 10^8$ K. Superfluid suppression of a non-standard neutrino emission mechanism slows the cooling rate such that non-standard cooling curves can approach the standard cooling curves. Some superfluid models have a very high T_{cr}, which essentially shuts down all the non-standard cooling process. Other superfluid models have T_{cr}s that are too low, which fail to suppress the non-standard cooling sufficiently to explain the data. The

challenge is to choose a superfluid model that has the right amount of suppression. Page (1990) began this exploration, showing cooling using various gap energies, and other authors have followed with improved physical models (e.g. Umeda, Tsuruta, & Nomoto, 1994, and Page, 1998).

From the observational standpoint, measurement of the relevant parameters has been improved with the newer generation of X-ray telescopes. First off, the distance to these objects has been difficult to measure. Using the fits for the observational data, there is a ratio of distance with some other parameter, which in turn is unknown. For example, a blackbody radiator model gives a normalization that is given by $(R_S/d)^2$, where R_S is the apparent effective radius at distance d. The apparent effective radius R_S relates to the real radius R by $R_S = e^{-\phi_s/c^2}R$, where $e^{\phi_s/c^2} = (1 - 2GM/Rc^2)^{1/2}$ is the surface red-shift factor, with M being the gravitational mass and G the gravitational constant. Often, the distance to the neutron star is inferred from assuming that the effective radius is $\sim$10 km. Other methods of estimating the distance are also used to verify this assumption, but lacking a direct distance measurement will not constrain the radius. However, the availability of multi-wavelength observations and improved spectral resolution of X-ray telescopes have helped constrain the normalization by giving better distances and lowering the uncertainty.

Furthermore, getting the temperature has been improved. Often there are local areas of increased temperature, hot-spots (e.g. Greiveldinger, et al., 1996), which makes the model fitting more difficult since both the hot-spot and the stellar surface

have to be simultaneously fitted. With a sufficiently high number of measured X-ray photons, separating the two components has became increasingly easier with improved spectral resolution. Additionally, the magnetic fields associated with many neutron stars are thought to be very high, $\sim 10^{12}$ Gauss for a typical pulsar. In such a high field, a magnetospheric pair plasma is thought to exist (e.g. Wang, et al., 1998). The non-thermal process involving this plasma does emit X-rays, so they also have to be considered when attempting to fit the data. Beyond this, there are also potential physical effects of the environment which might distort the direct measurement of the surface temperature; however, improved spatial resolution has helped to minimize this. The most notable is the effect of the interstellar medium. Neutral hydrogen absorbs radiation very efficiently in the ultraviolet range of energies, and this effect extends into the X-rays. Fitting the data requires including the effect of interstellar absorption, which can be constrained by multi-frequency observations.

Additionally, the neutron star's surface can modify the emitted radiation from a pure blackbody radiator. One of the most pronounced effects is that of an atmosphere (e.g. Romani, 1987). Fits of hydrogen atmosphere models have shown effective temperatures for several neutron stars that are lower than blackbodies (e.g. Pavlov et al., 1994). The most dramatic example of hydrogen atmosphere models is for the Vela pulsar, which has shown that its surface temperature is much lower and a radius that is much larger than what a blackbody model would predict (Pavlov et al., 2001a). Consequently, improvements in atmosphere models have made getting the effective temperature a much easier task.

If getting all of this information is difficult with just the X-ray spectrum, observational information from other wavelengths provides the clues to many of the challenges. For example, looking at the γ-ray energies will give clues about the magnetospheric radiation; furthermore, an optical and/or UV observation can also constrain the temperature as well as the magnetospheric radiation. Many of the isolated neutron stars also happen to be radio pulsars. Getting constraints on the rotation angles and magnetic axes from the radio observations give clearer pictures to the model that should fit the X-ray data. Periodic variation of X-rays from a pulsar allows timing analysis and production of light curves. *RXTE*, the Rossi X-ray timing explorer, which covers a higher X-ray energy band than does either *ROSAT* or *ASCA*, provides good timing information for brighter sources, as do *Chandra*'s capabilities. *Chandra* also provides the ability to begin the analysis of phase resolved spectroscopy which in turn should begin to put tighter constraints on the physical models.

In addition, observation has driven new theoretical considerations. The discovery of magnetars, isolated neutron stars with huge, $\sim> 10^{14}$ Gauss magnetic fields, led to drastic modification to thermal evolution theories, since magnetar surface temperatures were far in excess of temperatures predicted by standard cooling of non-magnetized neutron stars. Several authors (e.g. Heyl and Hernquist, 1997) have done extensive work on the cooling of a magnetar. Though magnetar thermal evolution is an important theoretical consideration, it is beyond the scope of the cooling theory presented herein.

For the thermal evolution theory of isolated neutron stars, observation will estab-

lish the extents for the neutron star surface temperatures. The theoretical challenge will be establishing thermal evolution theory which explains all of the data in a concise physically reasonable way.

The scope of our work includes both the observational and theoretical challenges in part. Our work to measure neutron star surface temperature using one of the newest tools, the *Chandra* X-ray observatory, will be presented in chapters 3-5, while chapter 2 introduces *Chandra* and chapter 6 discusses briefly the future of neutron star observations. The *Chandra* observation of PSR B1055-52, in chapter 3, shows that the surface temperature remains about the same as previous *ROSAT* and *ASCA* results, but we found a three component model to be the best fit to the data, contrary to their two component models. In chapter 4, we show our results of the *Chandra* data analysis of SGR 1900+14 immediately following its most recent outburst, indicating that the magnetar model is a good explanation for the results. Chapter 5 shows our new spectral results of the *Chandra* data analysis of 1E1207.4-5209, indicating that a hydrogen atmosphere is required. Chapter 7 presents our results for the theoretical challenge offered by the new observations, with the effects of Cooper pair neutrino emissivity. We show that the correct choice of superfluid with pion cooling can explain all the currently available data. A summary, in chapter 8, will give the key observational and theoretical results.

CHAPTER 2

CHANDRA X-RAY OBSERVATORY

Introduction

The *Chandra* X-ray Observatory (CXO) was formerly known as AXAF, the Advanced X-ray Astrophysics Facility. Its capabilities were intended as a combination of the *ROSAT* and *ASCA* energy range with improved spatial and spectral resolution, with a larger effective area. The spatial resolution was accomplished by the combination of the high resolution mirror assembly (HRMA) combined with the small pixel size of the Advanced CCD Imaging Spectrometer (ACIS) and with the High Resolution Camera (HRC) chips. Spectral information is complemented by two gratings, the Low Energy Transmission Grating (LETG) and the *Chandra* High Energy Transmission Grating (HETG).

The HRMA is a set of four paraboloid-hyperboloid (Wolter-1) nested pairs that are 1.2 meters in diameter. The mirrors are grazing-incidence so that the X-rays do not penetrate deep into the mirror material before being reflected. The mirrors are coated with iridium to a depth of 30 nm. The effective area of the mirrors runs from

$\sim$800 cm^2 at 0.5 keV and drops down to $\sim$400 cm^2 at 2.0 keV, then steadily drops off at higher energies. The large effective area of the mirror make the spatial and spectral resolution the best yet made.

At the rear of the telescope in the focal plane is the Scientific Instrument Module (SIM). The SIM contains the ACIS and HRC chips along with the LETG and HETG gratings. The various instruments can be brought into focus and can be used for observations depending upon the scientific objectives.

The ACIS is an array of 10 CCDs. Four of the CCDs are designed especially for imaging, being designated the ACIS-I. They are arranged in a square, 2 x 2 array, at the center of the focal plane. Below the ACIS-I on the focal plane, are the 6 ACIS-S CCDs, designed for spectral work in imaging mode or with one of the two gratings. Two of the CCDs are back illuminated, while the other 8 are front illuminated. The ACIS CCDs have excellent spatial resolution, $\sim$0.″5 full width half maximum (fwhm). The timing resolution is $\sim$3 s in imaging mode; however, the ACIS-S3 can be used in Continuous Clocking (CC) mode, improving the timing resolution to $\sim$3 ms, but the image is reduced to 1 dimension.

The HETG is the principle grating to be used with the ACIS-S CCD array. The grating is composed of two gratings for high and medium energies, the High Energy Grating (HEG) and the Medium Energy Grating (MEG). The HEG and MEG are offset from each other on the ACIS array to avoid overlap so that the spectral information can be used simultaneously.

The HRC consists of a set of two Micro-Channel Plate (MCP) type detectors. One

is optimized for imaging (HRC-I) and the other is a readout for the LETG (HRC-S). The HRC-I has the largest field of view of all of *Chandra* instruments giving a half degree by half degree image. The spatial resolution of the HRC detectors are $\sim 0\farcs4$ fwhm. The spectral range for the HRC is larger than that of the ACIS, but the spectral resolution is much less for the HRC-I. The timing resolution of the HRC is the best available on *Chandra* , having 16 μs resolution.

The LETG is the grating for the HRC-S detector, though it can be used with the ACIS-S array. The energy range with the HRC-S is 70-7290 eV and 200-8860 eV with the ACIS-S. The resolution for a spectral line in these ranges is $\sim$ 0.005 nm fwhm, having the highest resolving power available on *Chandra* at low energies (0.08-0.2keV). The LETG in combination with the HRC-S allows time resolved spectra and spatially resolved spectra of multiple sources (*Chandra* Proposers Observatory Guide, 2000).

Data Reduction

The data reduction for *Chandra* is an involved process for each of the different instruments and modes available. Since our work primarily involves the use of the ACIS-S3 chip in CC mode without any gratings, the discussion will be confined to procedures for that chip and mode. Similar procedures can be used for the ACIS in imaging mode. The analysis is performed using utilities from the *Chandra Interactive Analysis of Observations* (CIAO) software package, available from the *Chandra X-*

ray Center (CXC), and the xspec spectral analysis program, available from the High Energy Astrophysics Science Archive Research Center (HEASARC).

The raw data received by the CXC at Harvard University, is first run through some pre-processing, called pipeline processing, before being made available to the individual observers. This procedure sets up the data in a usable form for the user. The raw data, without any pipeline processing, is available, but its use is not recommended. Bias correction, overclock correction and coordinate transformations are applied to the data in this process. Also, any events which are certain to be considered bad due to background flares or solar activity are removed. Once the processing pipeline has been produced, the data is made available to the users (Data Products Guide, 2001).

The first important procedure that we must perform is to correct the observation for spacecraft dither and SIM motion. This affects the position and the time of the event, because the y-axes of the chip is used to compute time. Figure 2.1 shows the raw event file prior to the correction. Without the correction, the timing analysis is flawed, producing several periods near the actual period, and spectral analysis has a potential for flaws, because of the increased background. Correcting for this motion requires applying the following correction:

$$t_{corr} = t + t_o \; sin\xi \; (\alpha - \alpha_{med}) \; cos\delta_{med} - t_o \; cos\xi \; (\delta - \delta_{med}), \qquad (2.1)$$

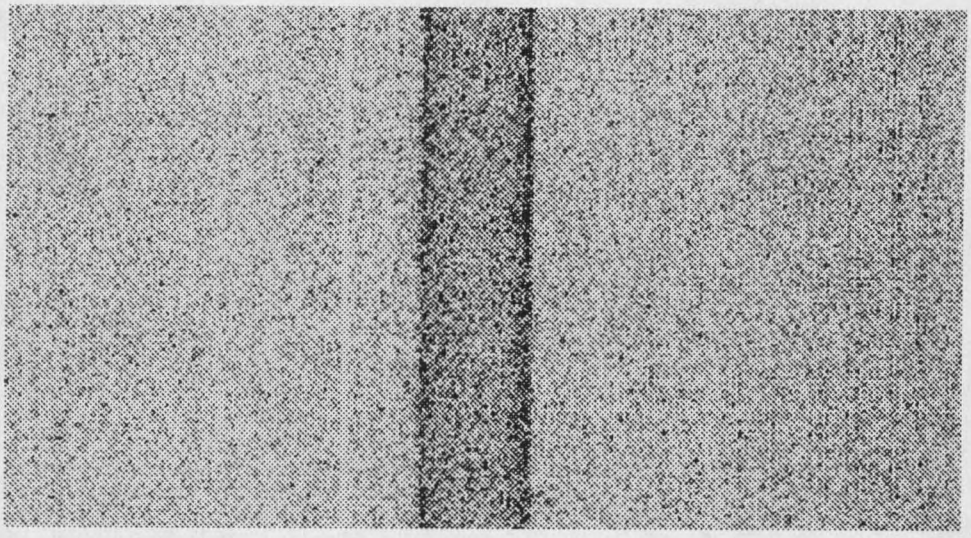

Figure 2.1: *Chandra* CC mode image of 1E1207.4-5209 without correction for spacecraft dither and SIM motion. The image is a negative linear grey scale. The horizontal scale is position at 0.″5 per pixel, and the vertical is time at 2.8 ms per pixel.

and

$$x_{corr} = x + x_o \, cos\xi \, (\alpha - \alpha_{med}) \, cos\delta_{med} - x_o \, sin\xi \, (\delta - \delta_{med}), \qquad (2.2)$$

where t is the spacecraft time, t_o = 20.857898 s, x_o = 7318.5607 pixels, α_{med} and δ_{med} are the median right ascension and declination for the spacecraft throughout the observation. Furthermore, ξ, α, and δ, are the spacecraft roll angle, right ascension, and declination of the spacecraft at the time of the event (Allen, 2000). Figure 2.2 shows the CC mode image after the appropriate corrections have been applied.

After corrections for the dither and SIM motion, the times must be corrected for accurate timing analysis. To get accurate timing analysis all motions of the spacecraft have to be taken into account and the resulting arrival times need to be computed with respect to a common reference point. The accepted reference is to compute the

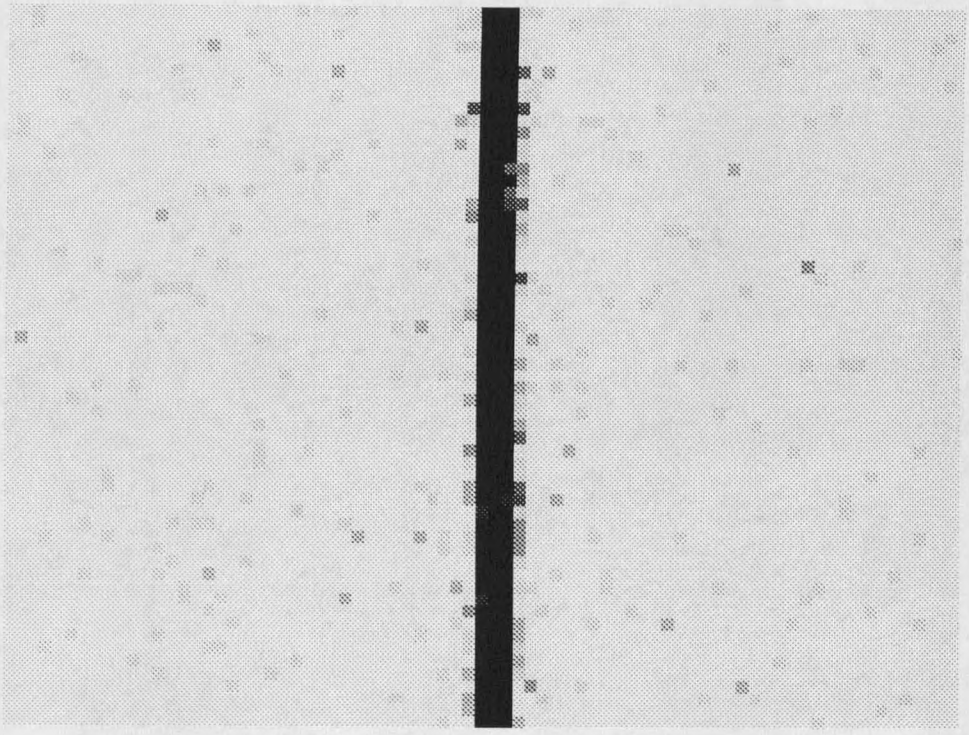

Figure 2.2: *Chandra* CC mode image of 1E1207.4-5209 with correction for spacecraft dither and SIM motion.

arrival times with respect to the solar system barycenter. This is accomplished using the AxBary utility provided with the CIAO software package. Once these important corrections have been made, the data is ready to be used for scientific analysis.

The CIAO package provides many tools for manipulating the data, the four most useful tools in pulsar data analysis are dmlist, dmcopy, dmextract, and dmstat. All of the tools have the ability to apply filters to the data files. The filtering can be done versus any column in the data file. It can be a spatial filter, removing contributions from all but a certain region of the chip, a timing filter, getting times of interest, or many others. The tool dmlist allows listing of the contents of a data file, providing

a quick way to write needed information to an ASCII text file. To copy the filtered contents from one data file to another, the tool dmcopy is useful. Extracting spectral information for use with xspec is accomplished using dmextract. Lastly, the tool dmstat gives the maximum, minimum, and mean values of specified columns in the data set.

The filtering allows a very small area to be determined as the source, while a wider area can be established as the background. Copying the source and backgrounds into separate files, further analysis can be easily achieved. The bulk of the source counts is typically in a one or two pixel width area in a CC mode image. The sources were extracted including a one or two pixel tail on either side of the source. Backgrounds were about five times the width of the source extraction, to account for the lower background count rates.

Timing analysis is accomplished by writing the source event times to a data file and then running various programs to determine the period and light curves. Once the period is determined, the phase of each photon can be determined easily. This information can be written back into the data file with use of many different utilities.

Spectral analysis was accomplished by extracting spectral files for both the source and background. Fitting of the spectra were all accomplished by use of the xspec program. Often, part of the spectrum was ignored during fitting. There are reasons for this. First, data above a certain energy is noisy because of the background beginning to dominate. Before any spectral fitting was done to any spectrum, background and source spectra were compared to see at what energy the background begins to

dominate. All source counts above that energy were rejected. Second, the spectral response of the telescope itself is still unknown in certain energy ranges. As of this writing, there is reason for a high uncertainty for the spectral responses below 0.5 keV. Determining accurate responses are difficult for this range because of a lack of spectral lines for calibration in this range.

CHAPTER 3

CHANDRA OBSERVATION OF PSR B1055-52

Introduction

PSR B1055-52 is especially interesting for this thesis because it is one of the three isolated radio pulsars whose surface radiation was detected by *ROSAT*, and because it is, together with SGR 1900+14 and 1E1207.4-5209, presented in chapters 4 and 5, one of the three X-ray sources whose *Chandra* data were analyzed by the author.

Previous Observations and Results

PSR B1055-52 is one of the earliest discovered radio pulsars. It was discovered by Vaughan & Large in 1972 and has been extensively monitored in the radio wavelengths. Furthermore, it was one of the targets observed by the Compton Gamma Ray Observatory (CGRO) (Kaspi 1994, D'Amico et al 1996). Recently, the Hubble Space Telescope (HST) managed to image the pulsar despite the bright stars within the field of view that had made previous ground based observations impossible. PSR B1055-52 has also been observed in the X-ray band, by *ROSAT*, *ASCA*, and *RXTE*.

Very recently, it has been a target of *Chandra* and *XMM-Newton*.

The radio observations of PSR B1055-52 have given a radio pulse profile consisting of a pulse and inter-pulse separated by 120^o in phase (Biggs 1990). Lynn & Manchester (1988) extensively modeled many radio pulsars and found that the polarization position angle from the magnetic poles leads to an angle between the rotation and magnetic axes to be $\sim 75^o$ for PSR B1055-52. Observations and modeling of the radio data have suggested that PSR B1055-52 rotates at an oblique angle between the rotation axes and the observation axes, of $\gamma \sim 65^o$. The pulse and inter-pulse, that are consistent from 60 MHz to 1.4 GHz, are naturally explained as beamed radiation from opposite poles of the magnetic field sweeping past the observer.

At the opposite end of the electromagnetic spectrum, the γ-ray observations of PSR B1055-52 have been extensive. It is one of at least seven spin-powered pulsars that have been detected at γ-ray energies (Fierro et al. 1993). Between 1991 and 1998, it was observed by CGRO, giving details of the pulsed γ-ray radiation (Ulmer 1994, Thompson et al. 1999). The important results are: (i) a main peak in phase with the radio, with a secondary peak that is 0.2 separated in phase, (ii) the γ-ray flux does not vary over large time scales, (iii) the energy spectrum is power-law with index $\Gamma = 1.58 \pm 0.15$, from $\sim$ 70 - 1000 MeV, and a break above 1000 MeV to an index of $\Gamma = 2.04 \pm 0.30$, and (iv) the observed γ-ray radiation represents 6 - 13% of the spin down luminosity, depending upon unknown beaming geometry and uncertain distance. The OSSE (48 - 184 keV) and COMPTEL (0.75 - 30 MeV) γ-ray light curves are noisy with only a visible pulse in the COMPTEL range; however, the

EGRET (> 240 MeV) γ-ray light curve has a narrow pulse width and two distinct peaks.

The optical/UV observation of PSR B1055-52 used HST (Mignani et al., 1997). The Faint Object Camera (FOC) observation using the U(F342) filter gave a magnitude of $m_{F342} = 24.88 \pm 0.1$, corresponding to a flux of 1.3×10^{-30} ergs cm^{-2} s^{-1} Hz^{-1}. We found the optical data point to lie upon a continuous power-law of index $\Gamma = 1.47$, from the γ-ray range, indicating that the optical and the γ-ray are both magnetospheric in origin. Furthermore, the optical flux is not consistent with the blackbody emission, as all reasonable temperatures and normalizations established from X-ray observation give a flux in the optical that is too low, indicating to us that the optical includes a magnetospheric component.

X-ray observations have been carried out by several satellites. Early observations included *EINSTEIN* (Cheng and Helfand 1983) and *EXOSAT* (Brinkman and Ögelman 1987) but were limited by poor statistics. The first significant observation was carried out in 1992 by Ögelman and Finley (1993, hereafter OF93) using *ROSAT* PSPC and HRI detectors. Later, *ASCA* observed PSR B1055-52 (Greiveldinger et al. 1996, hereafter G96), but poor spatial resolution and a low number of counts limited the results.

The spectral analysis of the *ROSAT* and *ASCA* observations are summarized in table 3.1. OF93 found that a single blackbody model fits the data to an energy of 0.7 keV but leaves significant residuals at higher energies. Their single power-law model fits the data well at all energies, but it would imply an optical flux far in excess of the

Table 3.1: Summary of X-ray spectral results from previous observations. OF93 used *ROSAT* PSPC data only, while all others used a combined *ROSAT* PSPC and *ASCA* SIS data set.

Model	n_H $\times 10^{20} cm^{-2}$	Model Parameter	flux keV cm^{-2} s^{-1}	Ref.
Blackbody	2.4 ± 0.8	$kT = 70 \pm 5eV$	$(4.8 \pm 1.2) \times 10^{-3}$	OF93
Power-law	5.7 ± 1.0	$\Gamma = 5.8 \pm 0.5$	$(1.9 \pm 0.9) \times 10^{-1}$	OF93
Blackbody(soft)		$kT_s = 60 \pm 5eV$	$(8 \pm 2) \times 10^{-3}$	
plus	3.5 ± 1.0			OF93
Blackbody(hard)		$kT_h = 200 \pm 100eV$	$(1.2 \pm 0.7) \times 10^{-3}$	
Blackbody(soft)		$kT_s = 68^{+5}_{-9}eV$	$3.8^{+0.4}_{-0.1} \times 10^{-2}$	
plus	2.6 ± 0.6			G96
Blackbody(hard)		$kT_h = 320^{+170}_{-100}eV$	$6.2^{+4.4}_{-1.9} \times 10^{-5}$	
Blackbody(soft)		$kT_s = 60 \pm 5eV$	$(7 \pm 2) \times 10^{-3}$	
plus	3.0 ± 1.0			OF93
Power-law(hard)		$\Gamma = 1.4 - 1.5$	$(3 \pm 2) \times 10^{-5}$	
Blackbody(soft)		$T_s = 68^{+5}_{-9}eV$	1.4×10^{-2}	
plus	...			W98
Power-law(hard)		$\Gamma = 1.5 \pm 0.3$	9.8×10^{-5}	

HST measurement. Furthermore, the light curves for the observation indicate that a single spectral component can not explain the data. Two component fits for *ROSAT* PSPC and *ROSAT* PSPC with *ASCA* SIS show that blackbody plus power-law and two blackbody models fit the data equally well (OF93), though G96 preferred the two blackbody model and Wang et al. (1998, hereafter W98) preferred the blackbody plus power-law model for separate reasons.

The timing analysis of the *ROSAT* observation of PSR B1055-52 has shown clearly at least two components. At energies lower than 0.5 keV, the light curve is broad and has a small pulse fraction of 0.1. At higher energies, above 0.5 keV, the light curve is narrower. At 0.5 keV the pulse fraction increases to nearly 0.8 at approximately

1.0 keV then decreases again. The higher energy peak is phase shifted by 110° from the low energy peak (OF93). Though the *ROSAT* low energy peak has been reported to be in phase with the radio, the result has not been able to be duplicated by subsequent investigation (Pavlov et al., 2001b). There are two reasons for this: (i) the *ROSAT* orbit information during the period of the observation is unknown, requiring an extrapolation of the orbit from earlier and later times when it is known, and (ii) the original *ROSAT* data set has been subsequently reprocessed to modern data formats in 1995, so it is uncertain if the timing information has been modified from the original 1993 data set. However, the relative phase of the *ROSAT* light curves are verified by the *Chandra* light curves (see *Chandra* timing analysis).

Our *Chandra* Observation and Data Reduction

We observed PSR B1055-52 with *Chandra* 's ACIS-S3 chip in continuous clocking (CC) mode on 5 January 2000 for a total of 39.9 ks, giving approximately 27000 counts from the pulsar. CC mode has a timing resolution of 2.85 ms, but sacrifices one dimension of spatial information for timing, leaving one dimensional spatial information. The photon arrival times and sky positions had not been corrected for spacecraft dither and the SIM motion at the CXC, so we made manual corrections for these (Allen 2000, Tenant 2001).

The one dimensional nature of the CC observation required special handling to determine the background, spectral response, and telescope ancillary response. First

off, by studying the *ROSAT* HRI image of the field of view, taking into account the *Chandra* orientation for the observation, we found no point sources near PSR B1055-52 that would contribute to the source; however, it would have been ideal to use a *Chandra* HRC to image the field for faint sources that *ROSAT* would not have been able to detect, but none was available. We assumed the background to be a contribution of the entire column of the ACIS-S3 chip along the source position; consequently, we chose a wide set of columns near the source position as the background. Even though the spectral response and the ancillary response are not necessarily the same along the column, the background subtraction will remove the unwanted counts from the source since the background is equally affected by the change of spectral and ancillary response. For the spectral and ancillary response, we determined the aim point for the observation and verified the location of the source upon the chip was verified by its 'chipx' coordinate and the roll angle for the spacecraft. The spectral and ancillary response were chosen specifically for this location on the chip, which is exactly the procedure used to determine the responses for a point source for the ACIS-S3 chip in imaging mode.

Once the source, background, and responses were chosen, a 1-D image, light curves, and spectra were made and analyzed. We also made phase resolved spectra by calculating the phase of each arriving photon and sorting the data according to phase (see results section for details).

As of this writing, the spectral responses for *Chandra* ACIS-S3 below 0.5 keV are unknown. The reason for the difficulty is the lack of spectral lines in this range to

calibrate the detector. Rather than attempting to correct the *Chandra* responses, we used the data set from the *ROSAT* PSPC observation for spectral analysis for the low energy range. The 1-D image and light curves were unaffected by the uncertainty. Since *ROSAT* PSPC timing information remains uncertain, only *Chandra* data set was used for phase resolved spectroscopy (Pavlov et al, 2001b).

Our Results

Our goals for the analysis of the PSR B1055-52 *Chandra* data involved several things. First, we would search the one-dimensional image for evidence of a compact nebula. Furthermore, we wanted to carry out a detailed timing analysis including energy resolved light curves and pulsed fractions. Next, we would embark on a detailed spectral analysis to resolve the discrepancy between the differing interpretations of G96 and W98 for the combined *ROSAT* and *ASCA* observations. Lastly, we would begin a phase resolved spectral analysis to constrain the geometry of the spectral components. In the following subsections, we present our results.

One-Dimensional Spatial Results

The one dimensional image, figure 3.1, shows the number of counts versus the chip x position on the ACIS-S3. The peak at chip pixel 294 has 6376 raw pulsar counts. The plot has been fit to a Gaussian curve that has a full-width-half-maximum (fwhm) of approximately 1 pixel, or 0.″5, confirming the ACIS-S3 resolution. A point source

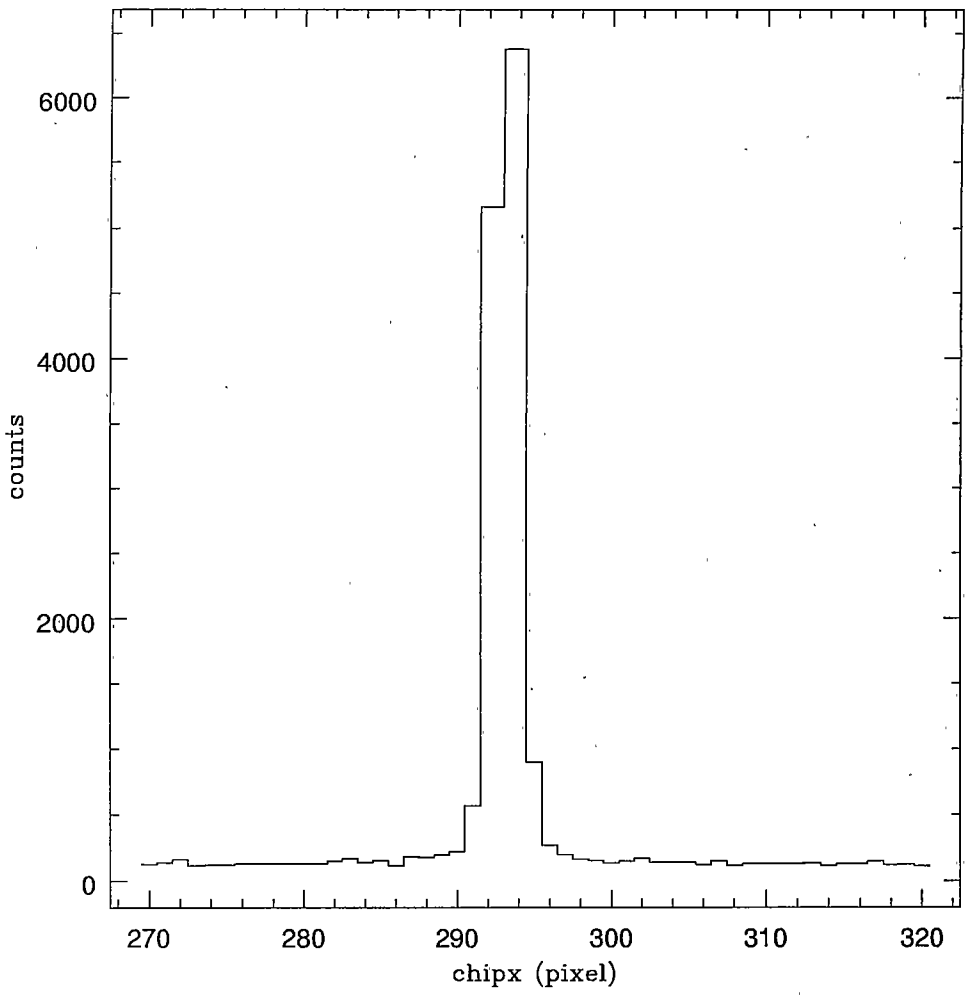

Figure 3.1: One dimensional continuous clocking (CC) mode image of PSR B1055-52.

should only be approximately 1 pixel wide.

The width of the tails in figure 3.1 suggests that there might be a compact nebula around PSR B1055-52, because of the increased counts that are at the base of our best fit Gaussian; however, the low number of counts and the high CC mode background made it impossible to prove. Hopefully, a high resolution image will be attempted at sometime in the future since the existence of compact nebulae around pulsars has

become an important topic because of the rich structure found in the compact nebula surrounding the Vela pulsar (Pavlov et al., 2001a).

Timing Results

We corrected the times to the solar system barycenter using the axBary utility which directly accounts for the spacecraft orbit and the orbit of the various bodies in the solar system, using the period and period derivative for PSR B1055-52 taken from the radio ephemeris of the Australian Pulsar Timing Archive. Careful analysis of the delay between the photon arriving on the ACIS-S3 chip and the time when the photon would be read out, allowed the computation of the phase of all X-ray photons with respect to the radio phase.

We checked the period of the *Chandra* data by examining the arrival times for periodicity near the radio ephemeris. The Z_1^2 (Rayleigh) test was used. Figure 3.2 shows the strong peak at 5.0732672 Hz, which is consistent with the radio ephemeris. The variable Z_1^2 has a probability density function equal to that of χ^2 with 2 degrees of freedom, thus obtaining a noise peak by chance in one trial is $exp(-Z_1^2/2)$. Consequently, for N independent trials the probability is $\rho = N\ exp(-Z_1^2/2)$ (Zavlin, et al, 2000). At the peak, $Z_1^2 = 462.220088$, so for one trial the probability for obtaining such a peak by chance is $\sim exp(-231.11)$. Consequently, we find a confidence, $C = (1 - \rho) \times 100\%$, for such a peak being the actual period of pulsations is nearly 100%.

Our light curves with respect to the radio phase are presented in figure 3.3. We

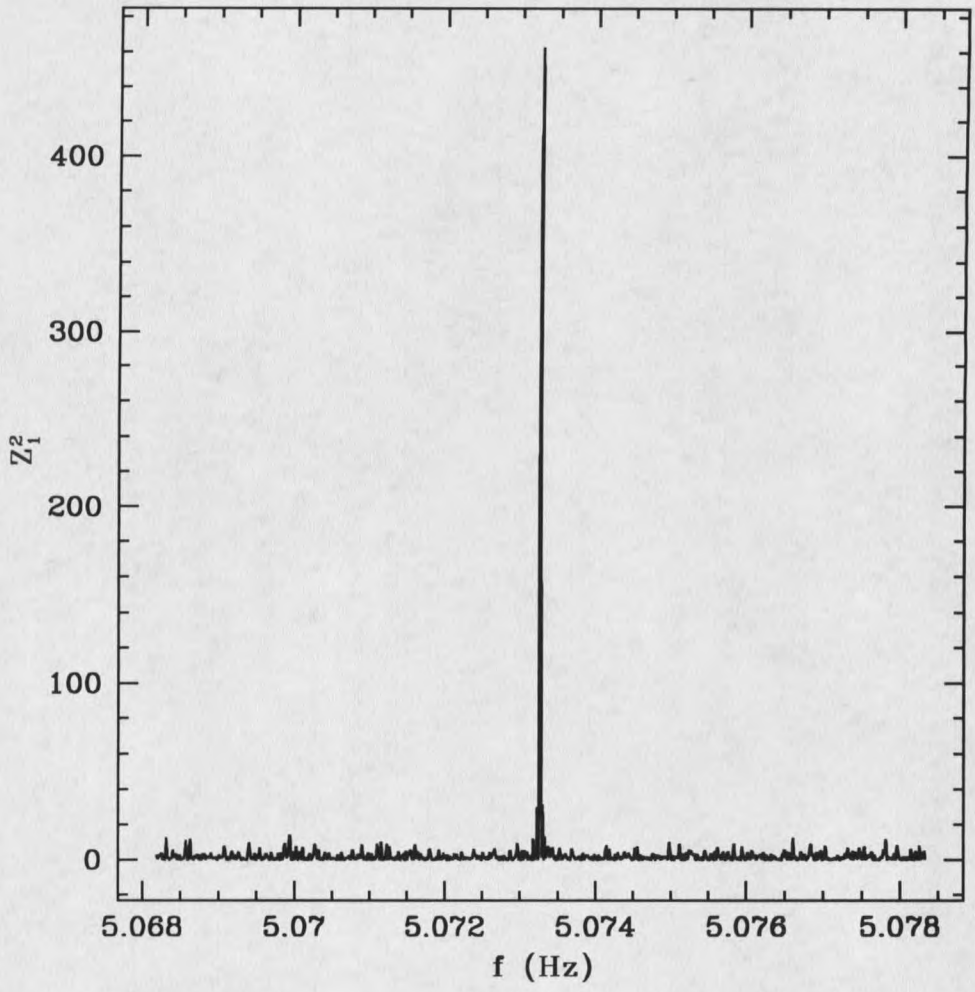

Figure 3.2: Z_1^2 (Rayleigh) statistic as a function of frequency for the *Chandra* data set near the radio ephemeris.

present the light curves using ten phase bins for the benefit of reader, while our analysis was performed using twenty phase bins and artificially smoothed light curves. Overall, they are very similar to the *ROSAT* light curves from OF93; however, the absolute phase of the *Chandra* light curves are different from those for *ROSAT* . The reason is because of the unknown orbit information for *ROSAT* during its observation of PSR B1055-52. The *Chandra* light curve is broad at low energy but narrows at

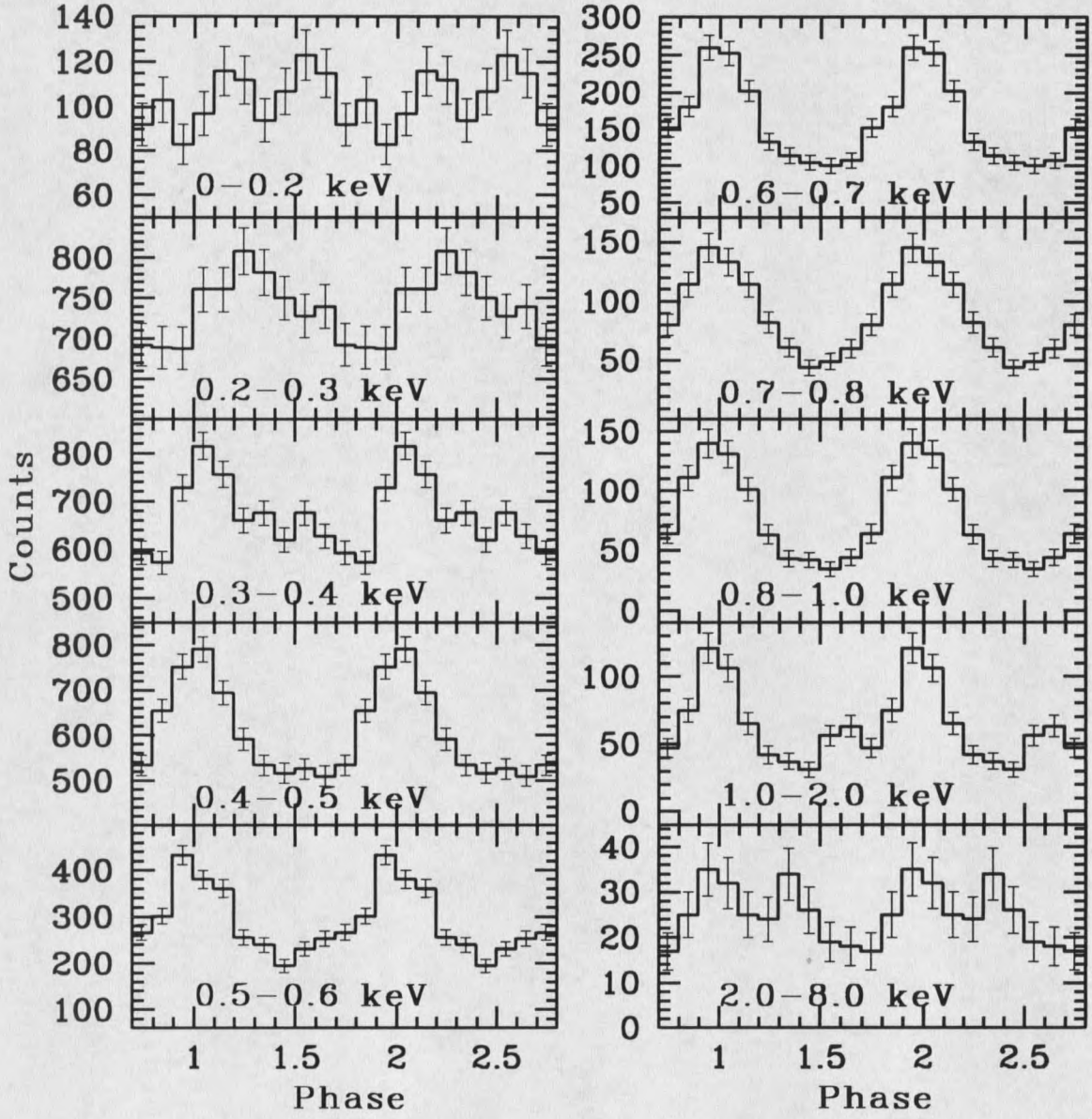

Figure 3.3: Energy resolved light curves of the *Chandra* observation.

higher energy before broadening again. There are two phase shifts present. One is at low energy, at ~0.3-0.4 keV of $\sim 100^o$, while the other is at higher energy but of smaller magnitude, ~0.8-1.0 keV of $\sim 35^o$. The second phase shift is not clearly visible in figure 3.3, but it is clear at higher phase resolution.

Figure 3.4 shows the pulsed fraction as a function of energy. As the energy increases from $\sim$ 0.4 keV to $\sim$ 1 keV, we find the pulsed fraction increasing from $\sim$ 15% to 50%. At higher energy, ~> 2.0 keV, the pulsed fraction decreases to $\sim$ 40%. OF93 found the pulsed fraction to reach $\sim$ 80%, but the low number of counts from the *ROSAT* observation makes the value very uncertain. But, our overall trend for the pulsed fraction is consistent with the earlier results of OF93.

Phase Integrated Spectral Analysis

To carry out spectral analysis of the lower energy part of spectrum for PSR B1055-52, we carried out a combined *ROSAT* and *Chandra* analysis. The *Chandra* data below 0.5 keV was ignored since we found the spectral response to be unreliable. Using *ROSAT* energies above 0.2 keV, we replaced the low energy *Chandra* data set. The data from all phases of the pulsar's rotation were used, thus giving a phase integrated spectrum. Subsequently, we analyzed the phase integrated data spectrum using previous models summarized in table 3.1. Our results are summarized in table 3.2.

A single blackbody model does not fit the spectral data, as the model deviated significantly from the data at nearly all energies. The best fit values of the parameters,

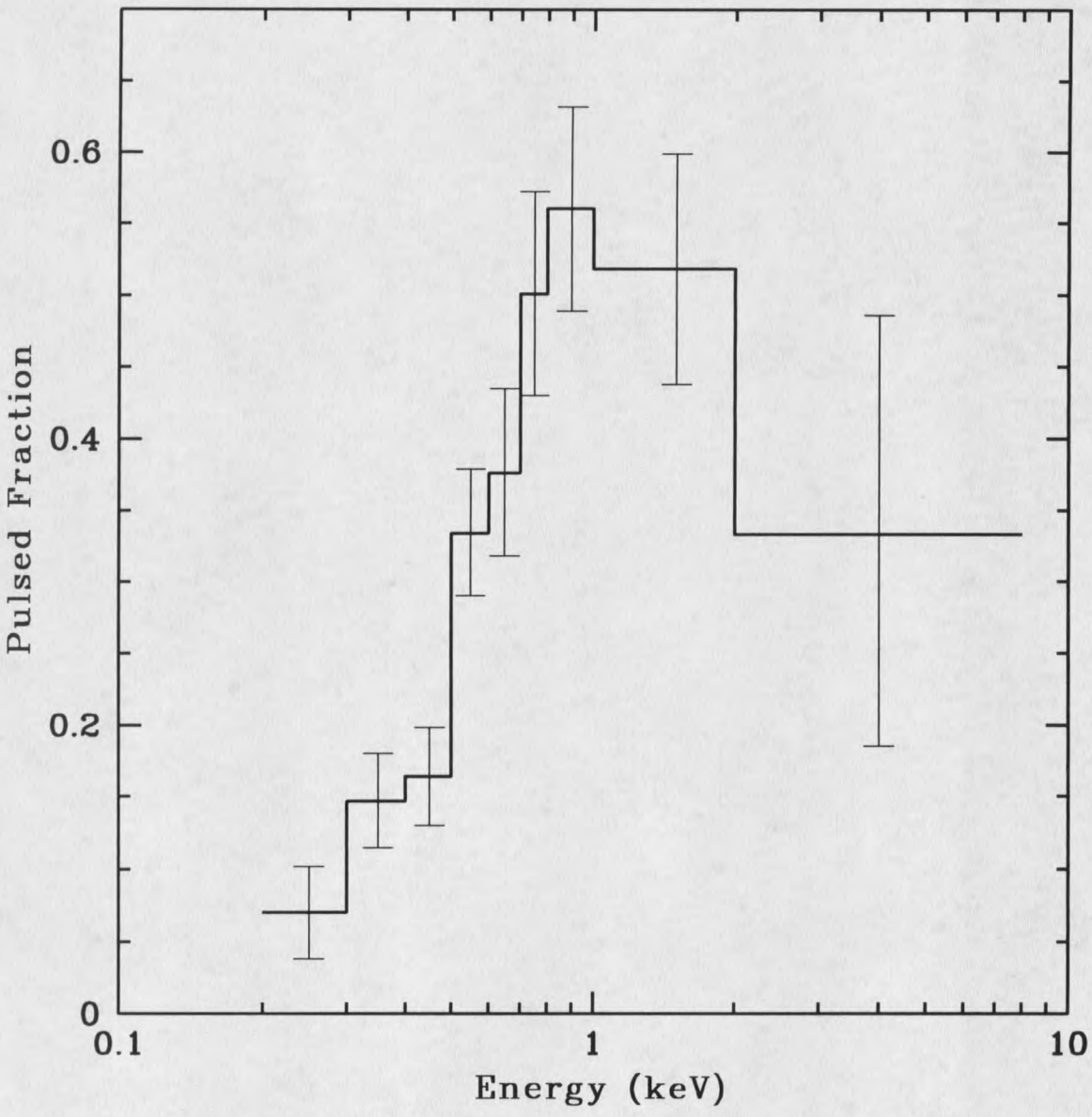

Figure 3.4: Pulsed fraction as a function of energy for the *Chandra* observation

Table 3.2: Summary of X-ray spectral results from combined *ROSAT* and *Chandra* analysis using models from previous work. A single blackbody component is labeled as BB, and a single power-law component is labeled as PO. The hydrogen column density is n_H. The soft blackbody apparent temperature are labeled kT_S and radius R_S. Similarly, the values for the hard blackbody are labeled with kT_H and R_H. The power-law index is Γ, and the power-law normalization is N_Γ. The fit statistic is χ^2, the degrees of freedom is d.o.f., and $\chi^2_\nu = \chi^2/\text{d.o.f.}$.

			Model	
Parameters	BB	PO	BB+BB	BB+PO
n_H (10^{20} cm^{-2})	34	6.2±0.3	$0.87^{+0.40}_{-0.31}$	1.4±0.5
kT_S (eV)	66	...	80^{+2}_{-4}	77±4
R_S (km at 1 kpc)	61	...	$8.5^{+1.9}_{-1.2}$	$9.3^{+2.2}_{-1.6}$
kT_H (keV)	...	...	$0.26^{+0.05}_{-0.04}$	...
R_H (km at 1 kpc)	...	...	$0.16^{+0.10}_{-0.06}$	...
Γ	...	5.7±0.1	...	$3.3^{+0.4}_{-0.5}$
N_Γ ($\times 10^{-5}$s^{-1} cm^{-2} at 1 keV)	...	$11.8^{+0.5}_{-0.4}$	...	$6.5^{+1.6}_{-1.3}$
χ^2	4206.	276.5	243.0	194.3
d.o.f.	139	139	137	137
χ^2_ν	30.26	1.989	1.774	1.418

as indicated by the large value for χ^2, ruled out this model. We found that a single power-law model faired much better, converging to $\chi^2 = 276.5$ for 139 degrees of freedom; however, we found a large deviation at energies above 1.5 keV suggesting that there was a missing component. Furthermore, the power-law index, $\Gamma = 5.67$, lacked an easy physical explanation.

We found two component models to be better, but not great. A two blackbody model converges to $\chi^2 = 243.0$ for 137 degrees of freedom, shown in figure 3.5. Again we found the residuals to deviate away from the data significantly at the higher energies, suggesting that the two blackbody model lacked a high energy component. A blackbody plus power-law model did better, with a $\chi^2 = 194.3$. However, the

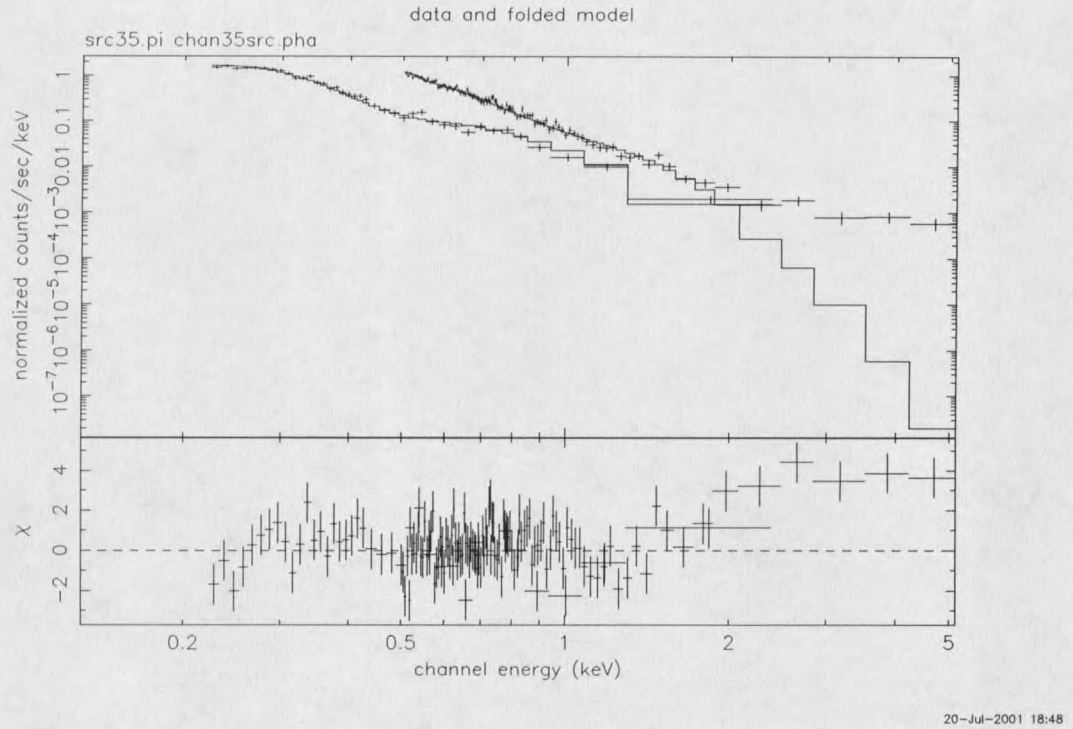

Figure 3.5: Results from PSR B1055-52 combined *ROSAT* and *Chandra* analysis using a two component model, two blackbodies. Notice the deviation of high energy photons in the residual.

power-law index, $\Gamma = 3.3$, was inconsistent with the expected index for the pair plasma in the magnetosphere, $1 < \Gamma < 2$; furthermore, we found a deviation of the fit at energies above 3.0 keV. To be consistent with the expected index, we attempted the blackbody plus power-law model with the index fixed at the value determined by W98, $\Gamma = 1.5$. Our results for the fixed index are shown in figure 3.6. with the index fixed. The residuals suggested that the model is not a good fit, because of their sinusoidal behavior. Though possible two component models were not exhausted, our results from the light curves suggested a three component model to account for the phase shifts and the energy dependence of the pulse fraction.

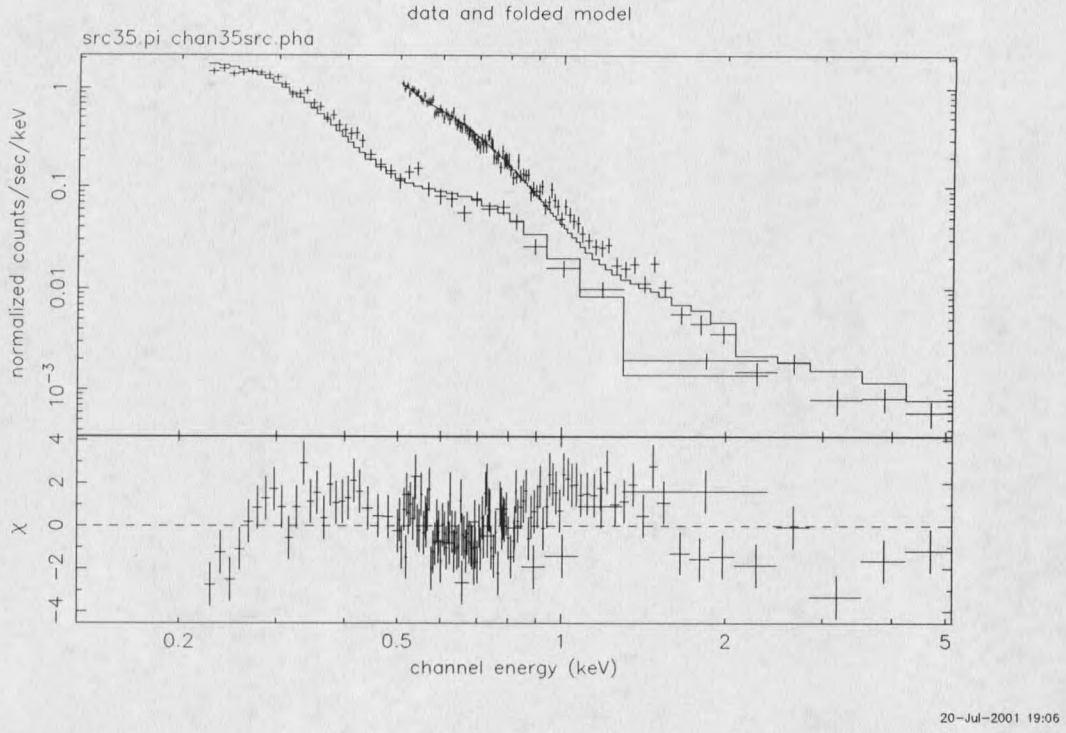

Figure 3.6: PSR B1055-52 combined *ROSAT* and *Chandra* analysis using 2 component, blackbody plus power-law with fixed index, Γ=1.5. The distinctive sinusoidal distribution of the residuals indicate a poor fit.

To make a three component model, we attempted a combination of G96 and W98 two component models. We began constructing our model with the power-law component, trying to extend it to the γ-rays. Our best power-law fit for the optical and the γ-ray observations suggest that the power-law component should have an index $\Gamma = 1.47$; however, the normalization for the best fit predicted a flux in the X-ray band that was higher than the flux for the *Chandra* data above 2.0 keV. Failing to connect the optical and the γ-rays through the X-rays with a single power-law, we concentrated our efforts upon the deviation found in the high, >2 keV, energies for the blackbody plus blackbody and the blackbody plus power-law fits. We assumed

that the missing component was a power-law and checked to see if its index would vary with phase. By calculating the hardness ratio defined as the ratio of the number of photons above and below a reference energy, we found that it did not vary more than its uncertainty for energies above 2 keV in five phase bins. Consequently, we regarded the slope of the power-law component as fixed. We determined the index by fitting the *Chandra* data above 2.0 keV with a single power-law model, finding the best fit for the power-law index to be $\Gamma = 1.66^{+0.57}_{-0.54}$. Since our power-law index was consistent with the expected value from the W98 magnetospheric pair plasma model, we chose two blackbodies as the remaining components.

The results of our three component fit are summarized in table 3.3. Since the

Table 3.3: Summary of X-ray spectral results from combined *ROSAT* and *Chandra* analysis using 3 component model.

Parameter	Value	
n_H	$1.3^{+0.5}_{-0.4}$	10^{20} cm^{-2}
kT_1	72.$\pm$10.	eV
R_1	12^{+3}_{-3}	km at 1 kpc
kT_2	$0.14^{+0.04}_{-0.03}$	keV
R_2	$0.8^{+0.8}_{-0.5}$	km at 1 kpc
Γ (fixed)	1.66	
N_Γ	$2.0^{+0.4}_{-0.5}$	10^{-5}keV^{-1}s^{-1}cm^{-2} at 1 keV
χ^2	144.08	
d.o.f.	134	
χ^2_ν	1.08	

power-law index was firmly established, our fits for the model considered it fixed.

The temperatures and the normalizations for our model seemed reasonable, based upon previous results for PSR B1055-52. We chose the distance of 1kpc based upon previous results (e.g. OF93), which was consistent with the expected radius of a neutron star. The fit for this model is in figure 3.7. We noticed that the model fits the data well over all of the energy range. It also showed the two blackbody components crossing at 0.8 keV, giving a natural explanation for the high energy phase shift in the light curves, if we assume that the two components are not exactly in phase with each other; however, we found no obvious explanation for the low energy phase shift with this model. The confidence contours for the fit parameters are shown in figures 3.8 and 3.9.

Another model, a blackbody plus two power-laws was attempted with reasonable fits. The results were suspect because of a photon index for one of the power-law components exceeded $\Gamma = 2$, as in the case with the two component blackbody plus a power-law. It failed to explain either of the phase shifts seen in the light curves.

A four component model was tried, three blackbodies and a power-law. The model was found to fit, explaining the 0.4 keV phase shift, but there was no compelling reason to accept the four component fit over the three component fit. An improved *Chandra* response matrix for low energy would be needed to consider such a model.

We considered a few other models, but they resulted in poor fits. Since the physical interpretation for the other models would be in doubt anyway, they aren't included within our results; however, the importance of the magnetic hydrogen atmosphere model results requires mentioning. The results were not rejected because of a poor

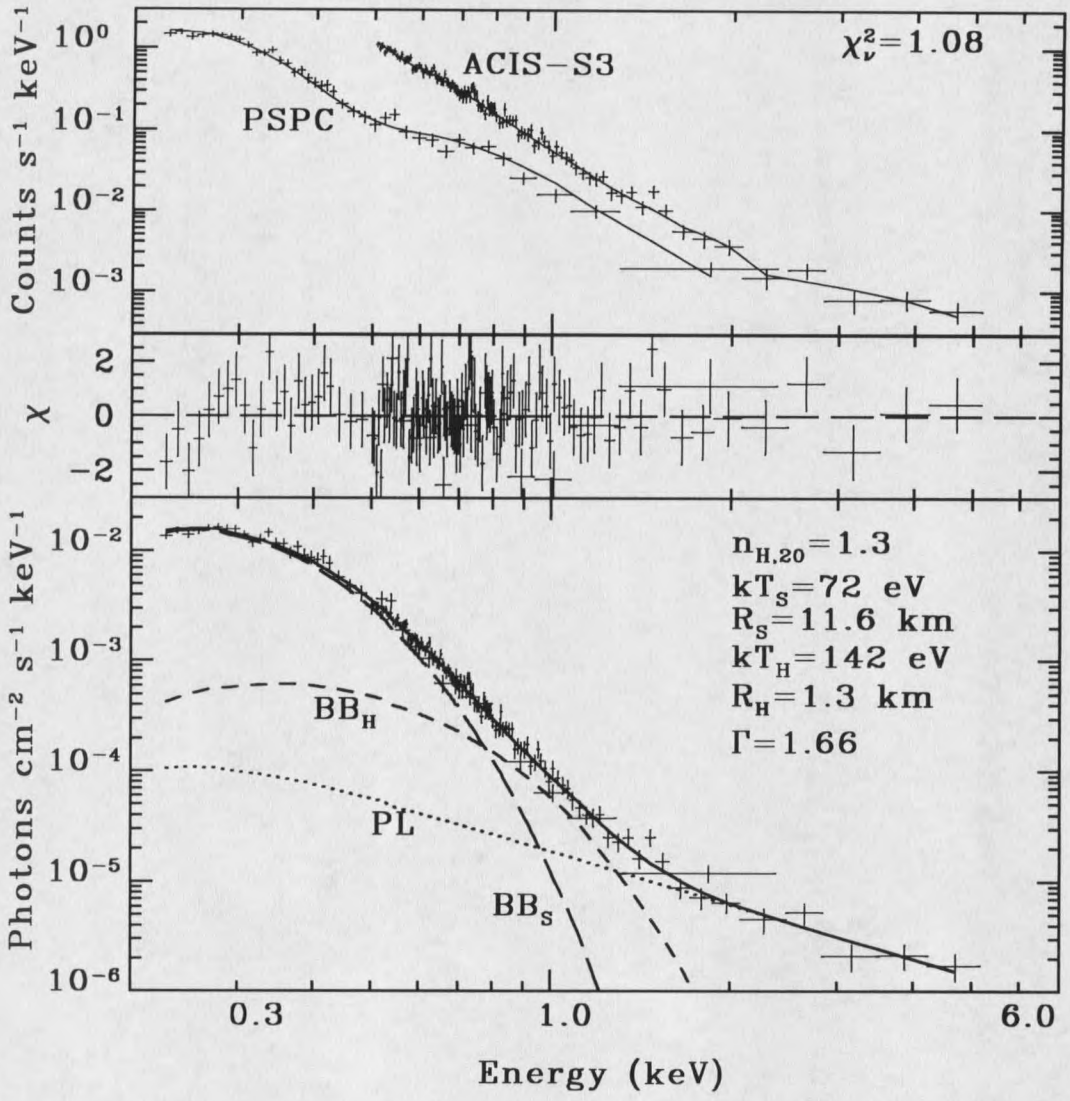

Figure 3.7: Results from our PSR B1055-52 combined *ROSAT* PSPC and *Chandra* ACIS-S3 analysis using three component, two blackbodies plus power-law, model. The top panel shows the raw *ROSAT* (low energy) and *Chandra* (high energy) data sets. The middle panel shows the residual for the fit. The lower panel shows the unfolded spectra with telescope response taken into account. The 3 curves are the soft blackbody component (long dash), the hard blackbody component (dash), and the power-law component (dot). The sum of the three components is the solid line.

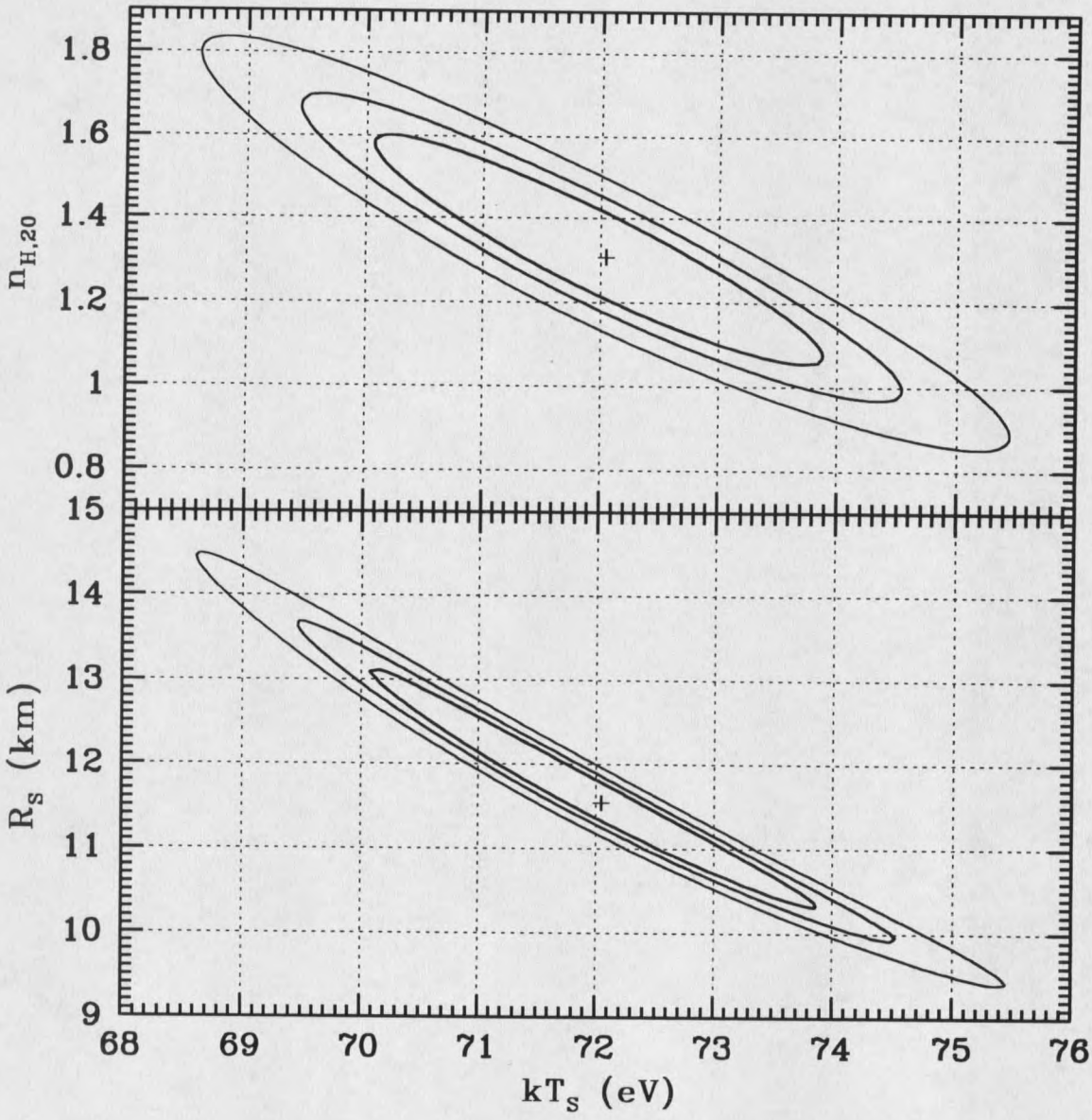

Figure 3.8: Confidence contours for soft blackbody for phase integrated spectrum. The contours are for $n_{H,20}$ versus kT_S and R_S versus kT_S, where $n_{H,20} = n_H / 10^{20}$ cm^{-2} and R_S is the soft blackbody radius in km at 1 kpc. The contours are 1 (inner), 1.6 (middle) and 2.6 σ (outer) using a 3 parameter fit.

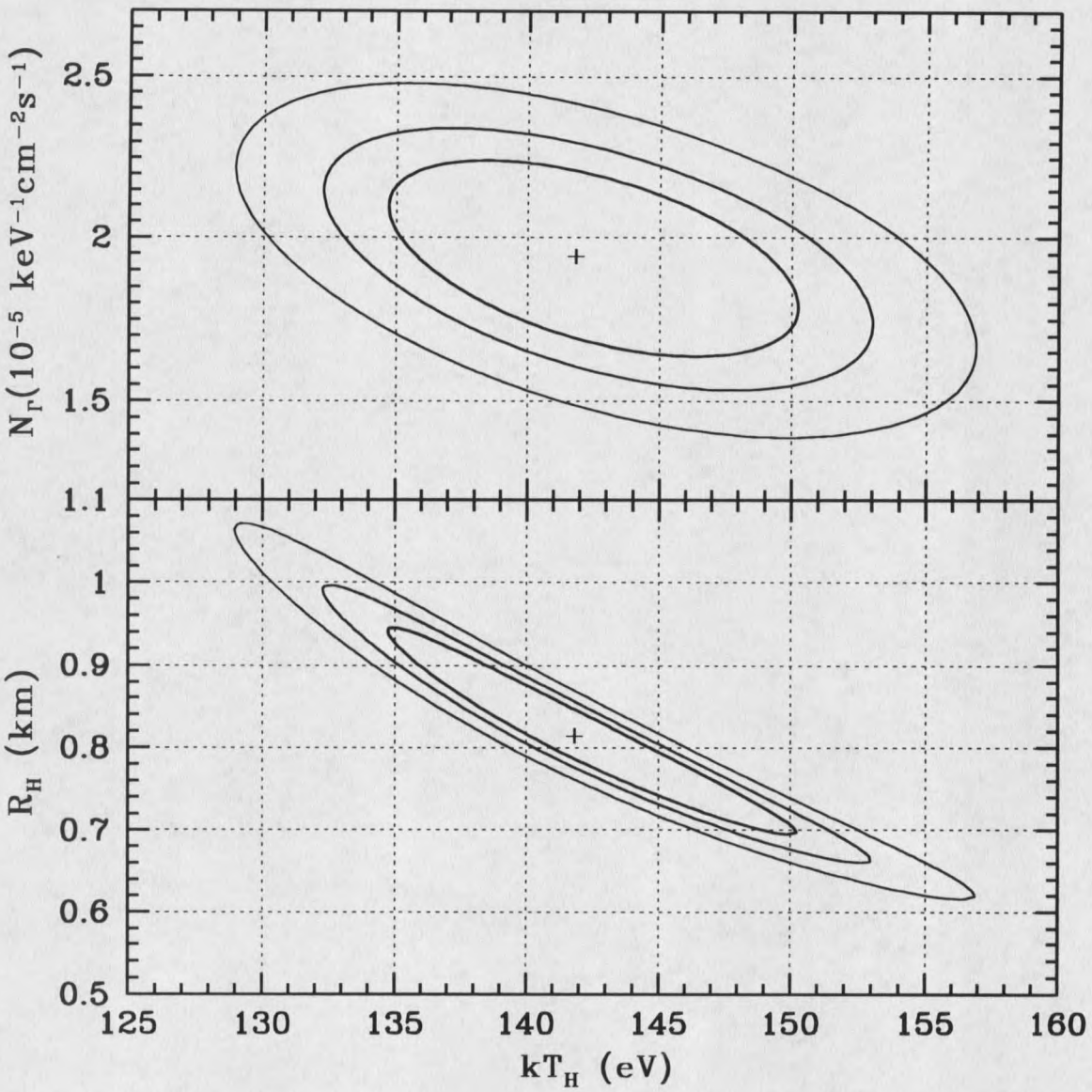

Figure 3.9: Confidence contours for the hard blackbody and power-law normalization for the phase integrated spectrum. The contours are for N_Γ versus kT_H and R_H versus kT_H. Again, the contours are using a 3 parameter fit.

fit but because of the distance of ~200 pc that the model predicted. The predicted distance was unacceptable because there would have been a detected large proper motion in the radio observations. No such proper motion has been reported, so the short distance is rejected.

Phase Resolved Spectroscopy

We attempted phase resolved spectroscopy to see the variation of spectral parameters with phase. For the phase resolved spectroscopy, the *ROSAT* data set was rejected because of its uncertain phase, so only *Chandra* data set above 0.5 keV was considered for the fitting. The observation was divided into five phase bins, concluding that five were optimal for error considerations. After dividing into phase bins the models were again tested for each phase, noting the fits and the differences between the varied model parameters. Only our three component model, two blackbodies plus a power-law, was used for phase resolved spectroscopy.

All of the model parameters could be varied from their phase integrated results with the exception of the hydrogen column density, n_H. Since n_H is a measurement of absorption between the observer and the target, we considered it to be independent of time. It might vary with time, but such variations should not be on the time scale of the observation, 30 ks, nor the period of the pulsar, ~200 ms. The variations of the interstellar medium would be irrelevant in this case. Subsequently, we regarded the phase integrated value of n_H as fixed.

Tables 3.4 and 3.5 shows the results for the phase resolved spectroscopy for fixing

a different set of parameters. In the first case, the soft blackbody normalization and the hard blackbody temperature were fixed. In the second case the soft blackbody temperature and hard blackbody normalization were fixed. Both cases left the model to be fit with a three parameter fit. We fixed the parameters to improve fitting accuracy with a low number of counts. The two cases were developed to avoid the prejudice imposed by fixing the parameters.

Table 3.4: Summary of X-ray spectral results from phase resolved *Chandra* analysis using 3 component model, case 1. The fixed parameters are n_H=1.3 $\times 10^{20} cm^{-2}$, R_s=11.6 km at 1 kpc, kT_H=0.14 keV , and Γ=1.66.

	Phase				
Parameters	-0.1 - 0.1	0.1 - 0.3	0.3 - 0.5	0.5 - 0.7	0.7 - 0.9
kT_s	73^{+1}_{-1}	73^{+1}_{-1}	71^{+1}_{-1}	71^{+1}_{-1}	72^{+1}_{-1}
R_H	$1.3^{+0.1}_{-0.1}$	$0.9^{+0.1}_{-0.1}$	$0.2^{+0.2}_{-0.2}$	$0.5^{+0.2}_{-0.2}$	$0.9^{+0.1}_{-0.1}$
N_Γ	$3.5^{+0.5}_{-1.4}$	$1.0^{+0.5}_{-1.0}$	$2.0^{+0.6}_{-0.6}$	$2.4^{+0.4}_{-1.0}$	$2.2^{+0.8}_{-0.8}$
χ^2	34.38	33.70	24.51	25.96	36.69
d.o.f.	48	31	20	22	34
χ^2_ν	0.72	1.09	1.23	1.18	1.08

Table 3.5: Summary of X-ray spectral results from phase resolved *Chandra* analysis using 3 component model, case 2. The fixed parameters are n_H=1.3 $\times 10^{20} cm^{-2}$, kT_s=72 eV, R_H=0.82 km at 1 kpc , and Γ=1.66.

	Phase				
Parameters	-0.1 - 0.1	0.1 - 0.3	0.3 - 0.5	0.5 - 0.7	0.7 - 0.9
R_s	$13.2^{+0.6}_{-0.6}$	$11.9^{+0.5}_{-0.5}$	$10.6^{+0.6}_{-0.6}$	$10.7^{+0.5}_{-0.7}$	$11.8^{+0.4}_{-0.5}$
kT_H	163^{+3}_{-5}	143^{+5}_{-4}	94^{+21}_{-94}	93^{+22}_{-93}	146^{+4}_{-5}
N_Γ	$3.0^{+0.7}_{-1.7}$	$0.6^{+0.8}_{-0.6}$	$2.1^{+0.2}_{-0.6}$	$2.0^{+0.5}_{-0.5}$	$2.2^{+0.7}_{-1.0}$
χ^2	42.64	33.19	24.46	24.44	37.62
d.o.f.	48	31	20	22	34
χ^2_ν	0.89	1.07	1.22	1.22	1.11

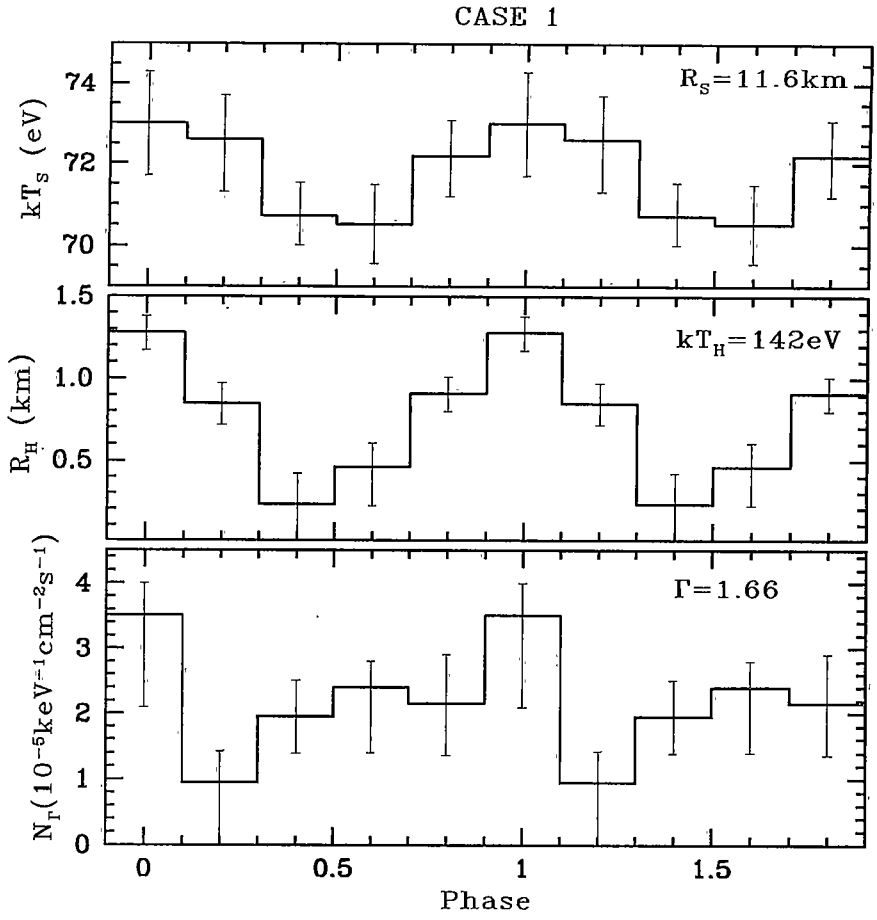

Figure 3.10: Phase resolved spectroscopy results case 1. The fixed parameters are labeled within the panels. The hydrogen column density, n_H was fixed at a value of $1.3 \times 10^{20} cm^{-2}$.

Figure 3.10 shows the first case where R_S and kT_H were held fixed. The variability of the free parameters are shown as a function of phase. The variation of the hard blackbody radius was found to be strong, while the soft blackbody temperature did not vary much more than its error. Figure 3.11 shows the second case where we held kT_S and R_H fixed. Again, we found that the soft blackbody component, in this case the radius, did not vary to a large extent. However, the hard blackbody temperature

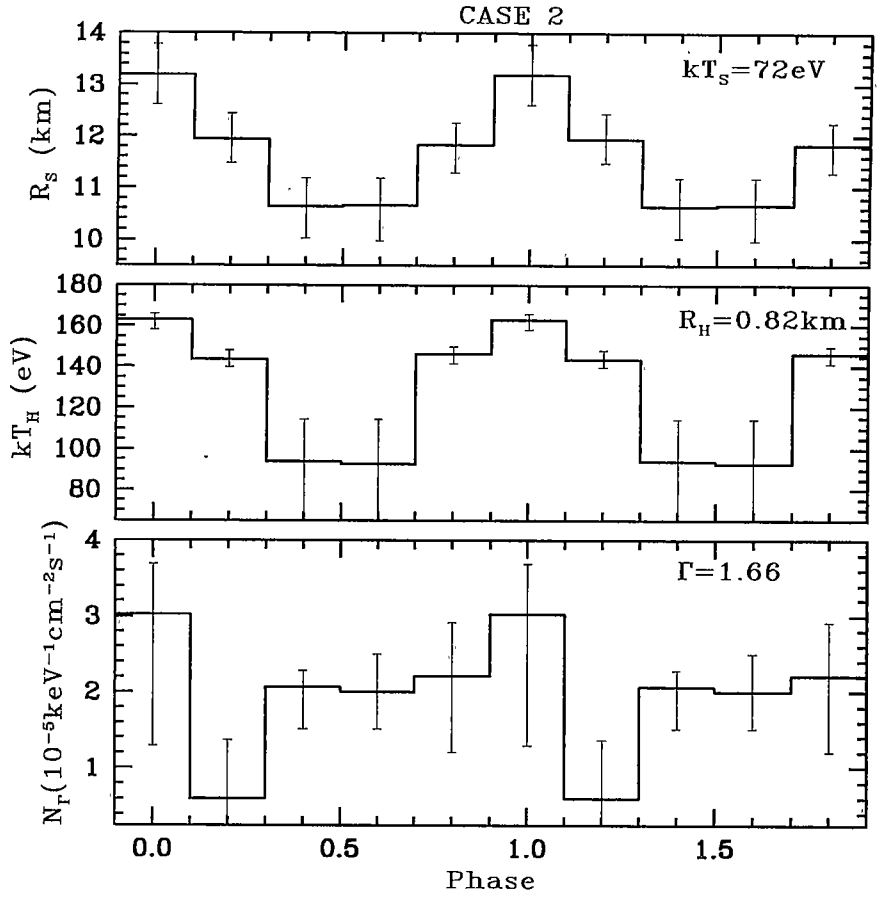

Figure 3.11: Phase resolved spectroscopy results case 2. Again, the hydrogen column density, n_H was fixed at a value of 1.3 $\times 10^{20} cm^{-2}$.

showed significant variation. In both cases the power-law normalization, N_Γ, showed similar variation with phase.

The bolometric flux of the individual components was calculated. In the case for the power-law component, the flux from 0.1 to 10 keV was found. Since the power-law index was fixed, then the flux behaves just like the power-law normalization, which has the units of flux at 1 keV. To conveniently construct the flux, we froze the parameters for the phase resolved spectra to their best fit values. Then, one component was fit to

the spectra. For example, to determine the soft blackbody bolometric flux in phase 0.7-0.9, first the spectral components were fixed at their best fit value. We then fit the soft blackbody temperature and normalization to the spectra. The final fit values were used to compute the flux for the soft blackbody at phase 0.7-0.9. The error for the flux was computed using a confidence contour for the component. We chose the contour as $\delta\chi^2 = 1$. By calculating the flux at points along the contour, the extremes of the flux were established as our upper and lower limits. The unabsorbed fluxes are presented in figures 3.12 and 3.13 as a function of phase.

For case 1, we found that the soft blackbody flux did not vary more than its uncertainty. The soft blackbody temperature was seen to have variability to nearly within its uncertainty. We concluded from Case 1 that all of the variability was due to the hard blackbody flux and the power-law. We considered this a contradiction because it did not explain variability of the light curves at the lower energy range.

In case 2, the soft blackbody flux was found to vary, but it was in phase with the hard blackbody flux. Though the phase resolution of the phase resolved spectroscopy was insufficient to view the high energy phase shift, at $\sim$ 0.8 keV, we found no indication of variation in the hard blackbody model to explain the large phase shift at low energy.

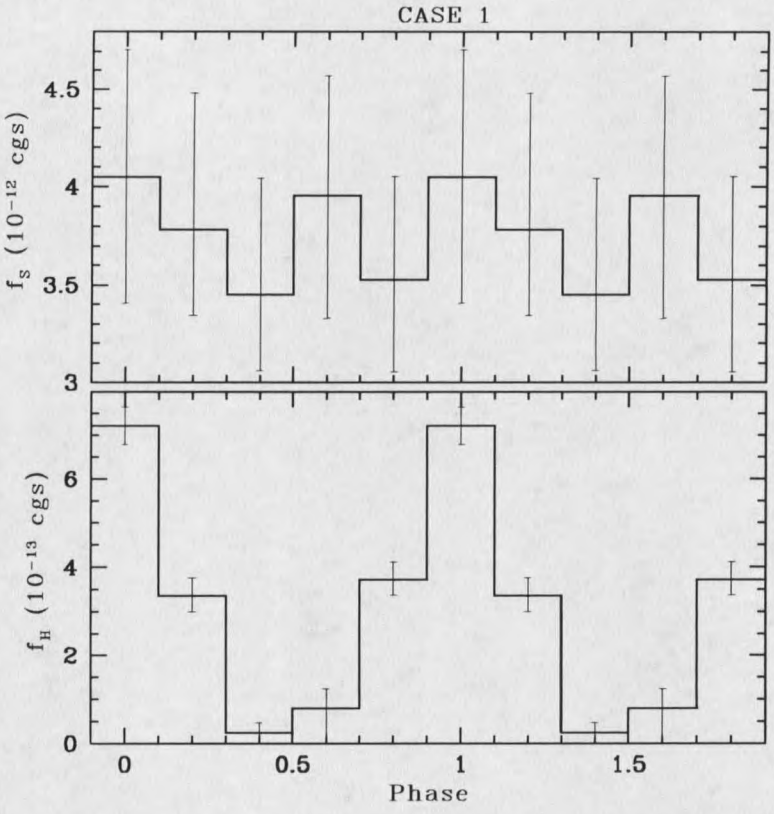

Figure 3.12: Phase variation of blackbody bolometric fluxes (Case I). For the blackbody components the flux was computed by fixing the other parameters to their best fit values for each phase. The errors in the flux were estimated from a $\chi^2_{min} + 1$ contour for the model component. The cgs units are ergs s^{-2} cm^{-2}.

Discussion

Earlier results suffered from poor counting statistics from the *ROSAT* and *ASCA* observations. Our findings from the combined *ROSAT* and *Chandra* data analysis show that two component models will not fit the data accurately. Neither the G96 two blackbody model, nor the W98 blackbody plus power-law model would fit the combined *ROSAT* and *Chandra* data. Using the G98 model, there is a significant deviation at high energy, while using the W98 model shows oscillatory behavior in

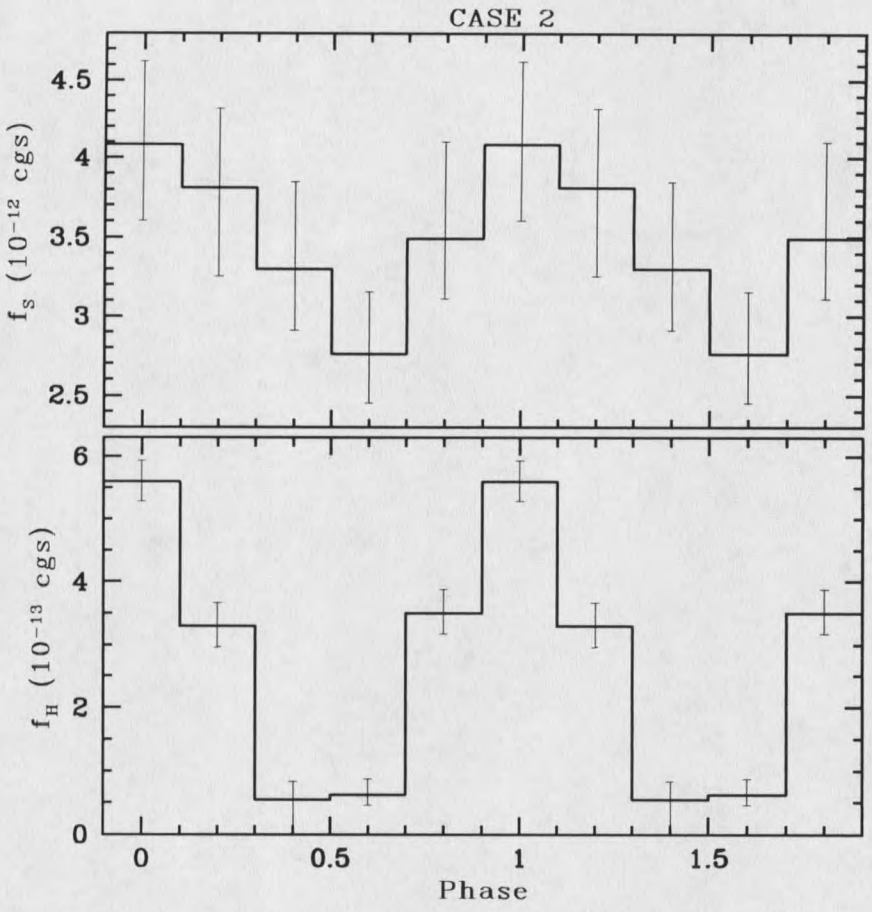

Figure 3.13: Phase variation of blackbody bolometric fluxes (Case II). See caption for figure 3.12 for details.

the residual. Furthermore, if we allowed the power-law index to vary, the best fit for the index is $\Gamma \sim 3$, which is inconsistent with non-thermal radiation expected from a magnetospheric pair plasma.

Our results for the phase integrated spectra for the combined *ROSAT* and *Chandra* observation require a three component model. First, the model requires a soft blackbody component, which we interpreted as thermal radiation from the neutron star surface. Secondly, a hard blackbody component is needed, which we considered

as a hot spot associated with one of the magnetic poles. Lastly, a power-law component is needed to account for the highest energy photons detected. The index, Γ=1.66, is consistent with a pair plasma for the magnetosphere.

Our temporal results, figures 3.3 and 3.4, show interesting trends. First, the pulsed fraction indicates a slow increase from 0.2 to 0.5 keV, to a value of $\sim$15%. Furthermore, the phase changes at approximately 0.4 keV with an angle of $\sim 100^o$. Above 0.5 keV, we found a sharp increase of pulsed fraction to about 50% at 0.8 keV, corresponding to the shift between the hard and soft blackbody components, see figure 3.7. We interpret the increasing pulsed fraction as the hard component becoming more dominant as the energy increases. It follows that the soft blackbody component could be interpreted as the overall neutron star surface with a temperature distribution, while the hard blackbody component represents a hot spot. The large pulsed fraction at 0.8 keV suggests, by our geometric models, that magnetic axes and the rotation axes are separated by a large angle. The decrease in pulsed fraction to about 40% above 2.0 keV, where the power-law component dominates, would be inconsistent with a higher pulsed fraction expected for the magnetospheric non-thermal radiation (Tsuruta, 1998), but the measured smaller pulsed fraction is due to a lack of counts at these higher energies.

The phase shift near 0.4 keV, with the lower energy peak lagging higher energy peak and the radio peak by $\sim 100^o$, has two possible explanations, an off-center magnetic dipole configuration (Halpern and Ruderman 1993), and multipole magnetic field structure (Page and Sarmiento 1996).

An off-center dipole configuration gives an easy explanation for the phase shift between the softer and harder components. If the dipole is off center toward one side of the star, the soft thermal component will tend to be hotter on one side than the other. Using the result of Greenstein and Hartke (1983) for the temperature modulation, $T(\theta) = (cos^2\theta + \chi_0 sin^2\theta)^{1/4} T_o$, with T_o being the surface temperature at the magnetic pole, χ_o being the ratio of parallel and perpendicular components of thermal conductivity, and θ being the angle between the magnetic field and the surface normal. Such a configuration would naturally explain the $\sim 100^o$ phase shift seen at 0.4 keV. This had been adapted to explain, in part, the phase shift for the Geminga pulsar (Halpern and Ruderman 1993).

A multipole magnetic field can be used to model complex temperature distributions upon neutron star surfaces. If a neutron star's magnetic field configuration is not a simple dipole, then the multipole field can be adapted to show many different distributions of temperature. The multipole field has up to five quadrapole field components with various strengths. Page and Sarmiento (1996) fit the multipole field to several pulsars using *ROSAT* data, including PSR B1055-52. The results showed that the phase shifts due to the temperature distribution of the multipole field case could be easily explained. However, the pulsed fraction required additional beaming to explain.

Our radius for PSR 1055-52 assumes an optimum distance of about 1 kpc. This could have easily been done by first assuming a radius for the neutron star and then computing the distance. For a stiff EOS, the neutron star is at its maximum radius.

Assuming a 1.4 solar mass ($M_{\odot}$) and a stiff EOS, the radius will be R=15km, and the distance d=1.3^{+4}_{-3} kpc. For a soft EOS with the same mass, R=7.7km, and a distance of d=0.7$\pm$0.2 pc. All are within the range of the distance established by other means (OF93).

CHAPTER 4

CHANDRA OBSERVATIONS OF SGR 1900+14

Introduction

Magnetars

Magnetars are a subclass of neutron stars with extremely high, $\sim> 10^{14}$ Gauss, magnetic fields. The huge magnetic field is expected to produce excessive heating in the magnetar due to the magnetic field decay, thereby giving it an extreme surface temperature. The ultra-high magnetic field also increases the conductivity enormously, resulting in a photon luminosity of 10^{35} erg s^{-1} (Kulkarni et al., 2000).

There are two types of sources that are thought to be magnetars, though some still disagree with this assessment (e.g. DeDeo, Psaltis & Narayan, 2001). They are anomalous X-ray pulsars (AXP) and soft gamma-ray repeaters (SGR). Kulkarni et al. (2000) have suggested that the only difference between the two is the magnetic field topology, where SGR derive their characteristic bursts from a tangled field rearranging in a catastrophic reconnection. Duncan (2001) pointed out that both AXP and SGR are associated with smaller SNR. Perna et al. (2001) has also showed that both AXP

and SGR data fit a magnetar model with consistent values for radius of a neutron star, with the exception of AXP RXS J1708-40.

Regardless, whether both AXP and SGR are magnetars, they are expected to become X-ray dark after a relatively short period. Assuming that a magnetar does not have an envelope of light elements, such as hydrogen or helium, they are expected to become X-ray dark within 10^6 years; however, if such an envelope exists then their observable lifetime will be as short as 10^4 years. Once the liquid interior of the magnetar cools sufficiently, it will halt ambipolar heating (Duncan 2001).

Soft Gamma-ray Repeaters(SGR)

Soft gamma ray repeaters (SGR) are γ-ray sources that have a spectrum of energies less than 100 keV. There are short and unpredictable outbursts of activity which last for days, or perhaps months, with long periods, years, of quiescence. There are four or five such sources detected, SGRs 1806-20, 1900+14, 0525-66, 1627-41, and possibly SGR 1801-23 (Duncan, 2001). All but SGR 1801-23 have had Super-Eddington luminosity, $L > L_{Eddington}$, bursts. SGRs 1900+14 and 0525-66 have had long duration giant flare events that are three orders of magnitude more energetic then the regular bursts (Hurley 1999). Flares have huge energies associated with them, $\sim 10^{44}$ ergs, while intermediate scale events are approximately two orders of magnitude less energetic. Bursts are the least energetic at $\sim 10^{41}$ ergs, but there seems to be a continuum of energies associated with these events (Kouveliotou, 2001).

Thompson and Duncan (1998) have pointed out that the nature of SGR is still

uncertain, but the magnetar model seems to be the most promising. Furthermore, they indicate that there is good evidence that all SGRs are associated with supernova remnants, and the large proper motion of SGR 0525-66 is inconsistent with a neutron star in a tight binary orbit. They also point out that the quiescent X-ray Luminosity of the plerion surrounding SGR 1806-20 cannot be powered by accretion. Furthermore, the X-ray flux from SGR in outburst is a million to a billion times the X-ray flux in quiescence (Thompson & Duncan, 1996).

Previous Outbursts of SGR 1900+14

SGR 1900+14 was discovered in 1979 when it burst 3 times (Mazets et al., 1979). In the following years, it was the least active of the SGRs, having only a series of bursts in 1992 (Kouveliotou et al., 1993), until May of 1998, when it had a large outburst. In the following August, SGR 1900+14 had a giant flare, the largest such event.

Prior to the 1998 events, the location of SGR 1900+14 was not precisely known. Data from the solar polar exploration satellite, *Ulysses*, the burst and transient source experiment on CGRO, BATSE, and the γ-ray burst detector, KONUS, on the Wind satellite gave its location to within a 1.6 arc minute circle near the SNR G42.8+0.6. The association between these two objects gives the SGR a transverse velocity 480-5500 km s^{-1}. The estimated velocities of other SGR are also high, so this is not unusual (Hurley et al., 1998a).

In 1998 *ASCA* was used to determine the location of the quiescent X-ray source

a month before the May outburst. The *ASCA* detection gave further evidence to the location of SGR 1900+14. The period was found to be P=5.1589715±0.0000008 s The best fit for the spectral data for the source was a power-law with photon index of 2.25±0.04 and hydrogen column density $n_{H,22} \equiv n_H/(10^{22} cm^{-2})$=2.16±0.07.

Several observations both prior to and after the 1998 outburst have established periods for SGR 1900+14. There is an increasing trend of the period over the times before and after the outburst; however, Woods et al. (1999) noticed a jump in the linear extrapolations of the periods immediately before and after the August outburst of ΔP=0.57 ms. They interpret it as a breaking glitch. Their extrapolated period derivative was 6.13×10^{-11} s s^{-1} before the August 1998 event, and 6.07×10^{-11} s s^{-1} after the event. Furthermore, they used *RXTE* to determine the period derivative of SGR 1900+14. Their period derivatives were found to be 8.2×10^{-11} s s^{-1} before the flare, and 5.93×10^{-11} s s^{-1} after the flare. In either case, the changes of the period derivative suggest that the spin-down rate of SGR 1900+14 is not steady.

April 2001 Event

Since 1998, SGR 1900+14 had been in quiescence. Then on 18 April 2001 at 7:55:12 UT, it became active again with a large flaring event detected by the Italian-Dutch satellite *BeppoSAX* using the γ-ray burst monitor, with a flux of 15400 counts per second for a duration of approximately 40 seconds (Frontera 2001). Data from *Ulysses* confirmed the giant γ-ray flare (Hurley 2001). The Schmidt telescope at Tautenburg was used in the I-band and did not find an optical point source down to

magnitude $I = 21$, within 18 hours of the flare (Klose 2001).

Subsequently, many instruments around the world began multi-frequency observations in the aftermath of the burst. *BeppoSAX* initiated a followup observation in the γ-ray band within 15 hours of the flare (Feroci 2001). Millimeter observations were done at the IRAM Plateau de Buré Interferometer on April 24, though no source was detected (Bremer 2001). Furthermore, the very large array *(VLA)* radio observation failed to detect the source (Fox et al. 2001). Other radio observations gave similar results (e.g. Kouveliotou et al. 2001).

In the X-ray, both *RXTE* and *Chandra* observed SGR 1900+14 twice within a week of the outburst. The second observations, on 30 April, overlapped. The two *Chandra* observations, 22 April and 30 April, were part of the Director's Discretionary Time (DDT) allocation, with lengths of 20.8 ks and 18.9 ks, respectively and were made available to the public domain almost immediately. The two *RXTE* observations began on 21 April and 30 April and lasted 15.2 and 15.6 ks respectively.

The *Chandra* observations were done in Continuous Clocking (CC) mode to provide 2.8 ms timing resolution. The excellent timing resolution of *RXTE* gave a good confirmation of the pulsation period detected from the source. The results which follow are from the two CC mode *Chandra* observations.

Our Results

We investigated the timing information of the two *Chandra* observations, attempting to see differences between the two observations. Our investigation of the spectral information, which focused upon seeing if there was a favored spectral fit clearly showed a blackbody component. Furthermore, with our phase resolved analysis, we hoped to uncover any information regarding the phase behavior of any of the spectral components, or a variation between the two observations.

Our Timing Results

We established the period of SGR 1900+14 by using the Z_1^2 (Rayleigh) statistic. Each observation was corrected for telescope dither and the times were corrected to the solar system barycenter. We present the results of the two observations in figure 4.1. The Z_1^2 is shown versus frequency compared to the frequency when Z_1^2 is maximum for the first observation. For the first observation we found that $f_{0,1} = 0.1933143^{+1.0e-06}_{-1.3e-06}$ Hz, corresponding to a period of $P_{0,1} = 5.172923^{+3.4e-5}_{-2.7e-5}$ s. In the second observation we found $f_{0,2} = 0.1933130^{+1.7e-06}_{-2.0e-06}$ Hz, corresponding to a period of $P_{0,2} = 5.172958^{+4.3e-5}_{-4.6e-5}$ s. We computed the errors by noting that Z_1^2 is equivalent to χ^2, so for a 1σ error, $\delta Z_1^2 \sim 1$.

Our periods for the two observations, combined with periods reported for the *BeppoSAX* observation (Feroci et al, 2001), and the two *RXTE* observations (Fox et al, 2001), show an increasing trend. A linear regression fit of the periods gives a period

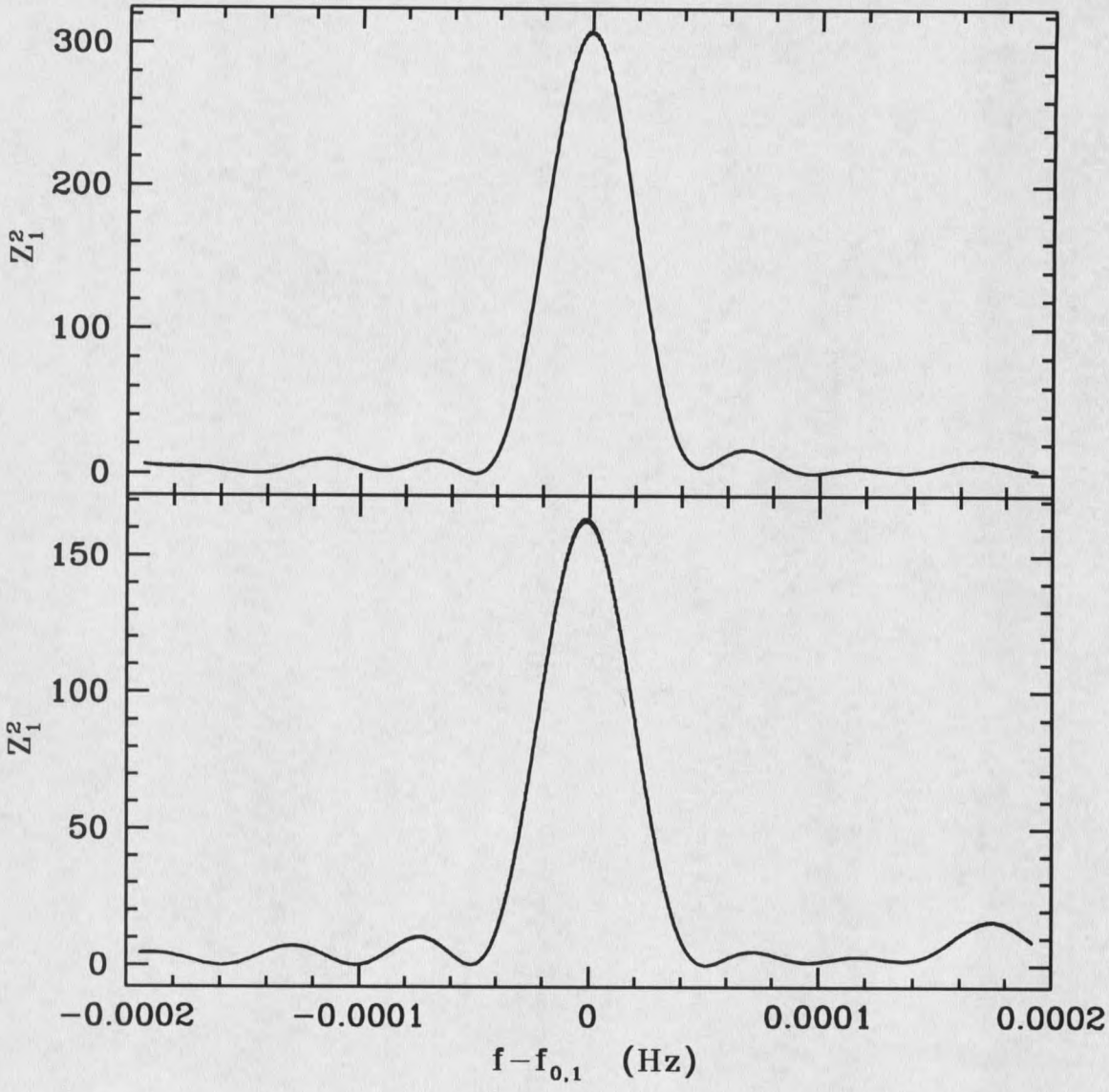

Figure 4.1: Comparison between first (top panel) and second (bottom panel) observation's Z_1^2 statistic. Both are compared to the best fit frequency for observation 1, $f_{0,1} = 0.1933143^{+1.0e-06}_{-1.3e-06}$ Hz. Note the slight shift for the second observation.

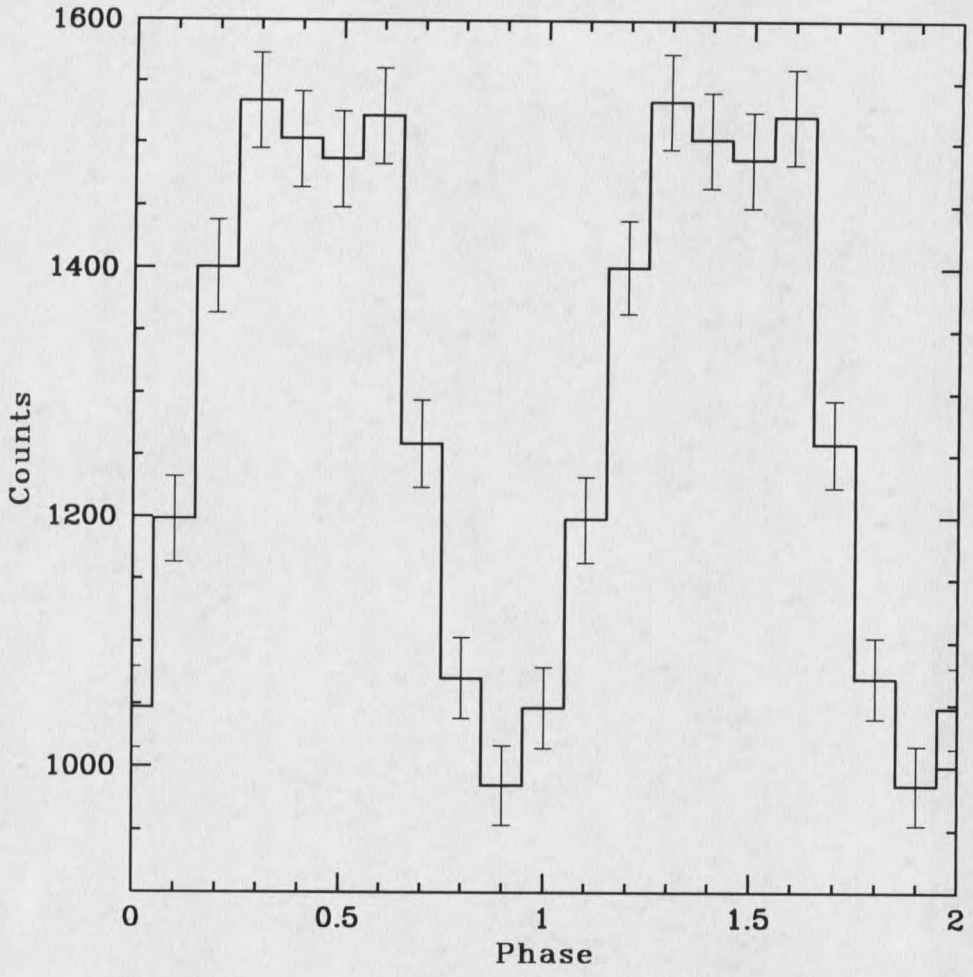

Figure 4.2: Light curve for the first *Chandra* observation.

derivative, $\dot{P} = 2.23 \pm 0.66 \times 10^{-11}\ s\ s^{-1}$. It is interesting to note that an extrapolation of the period derivatives from Woods et al. (1999) show a discrepancy of over 7 ms if extrapolated to the times of the 2001 observations. Our period derivative, however, is still well within the range of period derivatives seen in previous observations (e.g. Woods, et al. 1999).

Our timing analysis of both observations yielded energy resolved light curves. Figures 4.2 and 4.3 present our light curves for the entire *Chandra* range, 0.5-10.0

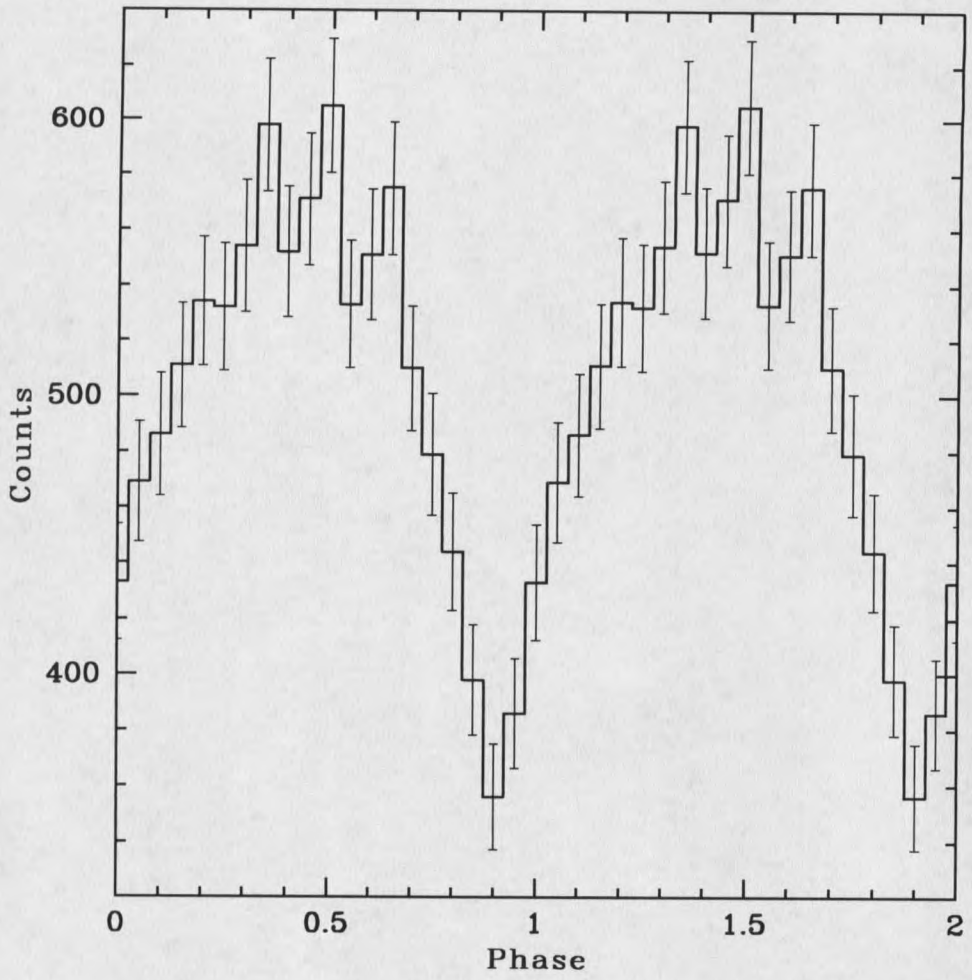

Figure 4.3: Light curve for the second *Chandra* observation.

keV, of the two data sets. Figures 4.4 and 4.5 show our light curves for the two observations as a function of energy. The light curves for the first and the second observation differ little except for count rate. Using the statistic S given by:

$$S = \sum_{i}^{I} \frac{(Nm_i - Mn_i)^2}{N^2 m_i + M^2 n_i} \tag{4.1}$$

where N=Σn_i and M=Σn_i, we quantified the difference between two light curves. It

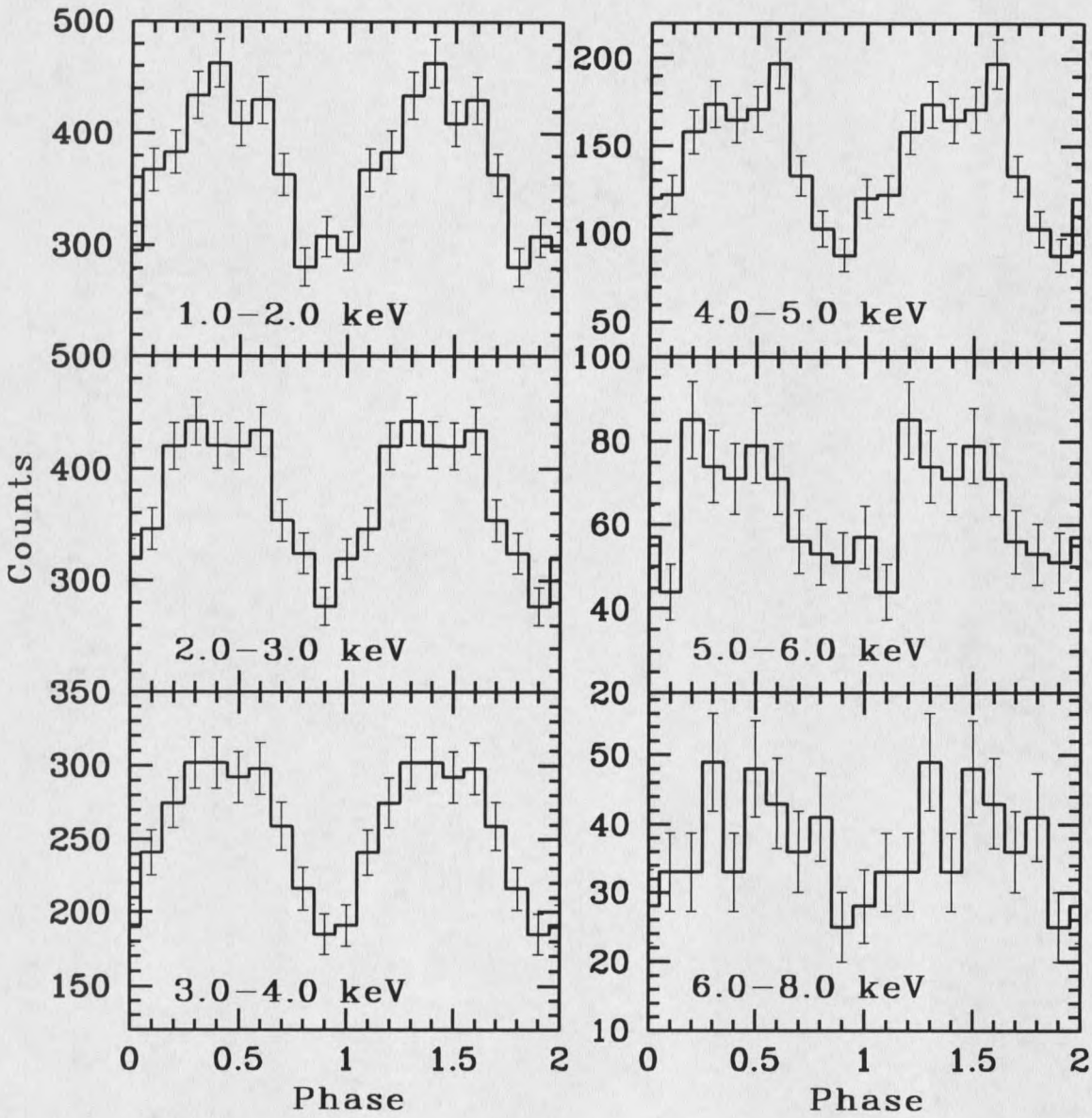

Figure 4.4: Energy resolved light curves for the first *Chandra* observation. There are insufficient counts below 1 keV and above 8 keV.

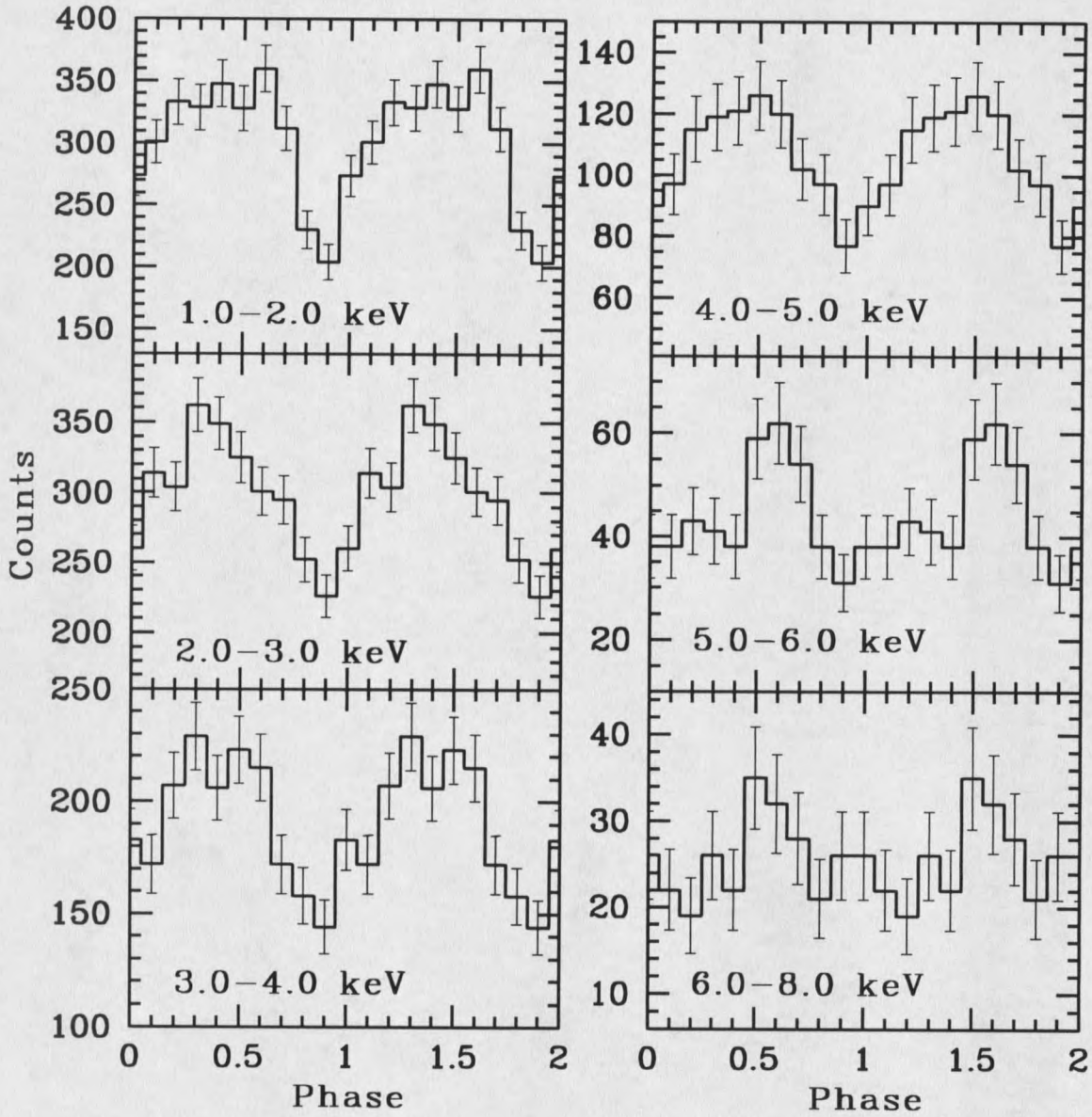

Figure 4.5: Energy resolved light curves for the second *Chandra* observation. The reduction of the observation time leads to an increase of uncertainty.

can be shown that S behaves as χ^2 so that the probability that two light curves are different depends on the value of S. The larger the result of S, the more probable that the two curves are different.

Using both the total light curve and the various schemes of energy resolved light curves, the maximum probability that we found for observation one differing from observation two was a little over 75%. Consequently, without a higher probability of difference, we regarded the light curves as the same, since there is still a 25% probability that they are indeed the same. We believe a more detailed statistical analysis should be done to determine if any differences can be extracted.

Our pulsed fraction calculations, however, suggested at least some difference between the two observations. Figure 4.6 shows our pulsed fractions as a function of energy for the two observations. We found a change in the fractional pulse for the two observations in the 4-5 keV range, suggesting that the more active state of the soft gamma ray repeater in the first observation has stronger pulsations in the 4-5 keV range than does the second observation. However, the uncertainty of our pulsed fraction overlaps slightly between the two observations making the change uncertain. We noted an interesting behavior present in the first observation that prevents the pulsed fraction from being constant over the entire energy range, as we found no horizontal line will pass through all the points in the top panel of figure 4.6.

Overall our timing analysis suggests that there is little difference in the light curves between the two observations, apart from the the overall flux and the pulsed fraction in the 4-5 keV range. For any differences to be apparent we left it to the phase

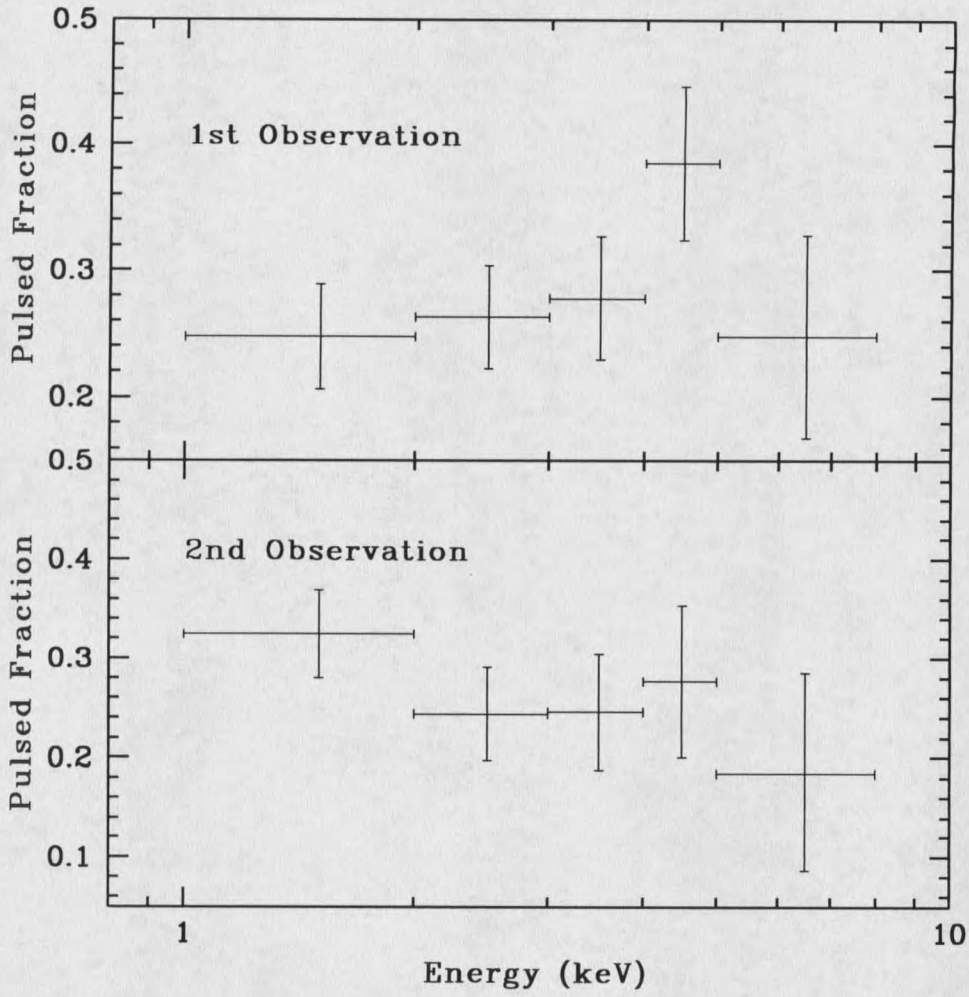

Figure 4.6: Energy resolved pulsed fraction for both of the *Chandra* observations. Notice the significant change in the 4-5 keV range.

resolved spectra to resolve them.

Our Phase Integrated Spectral Analysis

We found that a single blackbody does not fit the *Chandra* spectrum for either observation. In fact, the observations for the flare in the γ-rays suggests that some sort of power-law exists, which extends into the hard X-rays in the *RXTE* band.

Assuming that the power-law does continue to lower energy, we tried a single power-law model for both *Chandra* observations. Table 4.1 shows the results for a single power-law fit for both observations, and figure 4.7 shows our fit to the combined observation.

Table 4.1: Single power-law fit for both observations. The values in the parenthesis are best fit values using the fixed $n_{H,22}$ value from the combined fit.

	Obs 1+2	Obs 1	Obs 2
$n_{H,22}$	$2.850^{+0.098}_{-0.095}$	$2.81^{+0.13}_{-0.12}$	$2.90^{+0.15}_{-0.14}$
		(2.850)	(2.850)
Γ	$2.675^{+0.082}_{-0.080}$	2.61±0.11	$2.76^{+0.13}_{-0.12}$
		$(2.638^{+0.036}_{-0.037})$	(2.716±0.041)
N_Γ 10^{-2} keV $s^{-1}cm^{-2}$	$1.05^{+0.13}_{-0.11}$	$0.99^{+0.16}_{-0.14}$	$1.12^{+0.22}_{-0.18}$
		$(1.041^{+0.044}_{-0.043})$	$(1.054^{+0.050}_{-0.049})$
χ^2	445.5	226.7	193.4
		(227.1)	(193.8)
χ^2_ν	1.119	1.030	1.105
		(1.027)	(1.101)

Overall, we found that a single power-law fit works for both observations, as well as the combination of the two. A single power-law model, however, has a distinct difficulty in that it did not easily explain the pulsed fraction change that we found in the first observation. If only a power-law exists, we surmised that there are only two ways it could pulse. One was by changing its index, the other by changing its normalization. Even if both variations were present, we did not find a clear combination of the two which would fit the data, and match our pulsed fraction.

We attempted another model, a blackbody plus a power-law model, for both observations. Figure 4.8 shows our fit for this model. We kept the power-law an

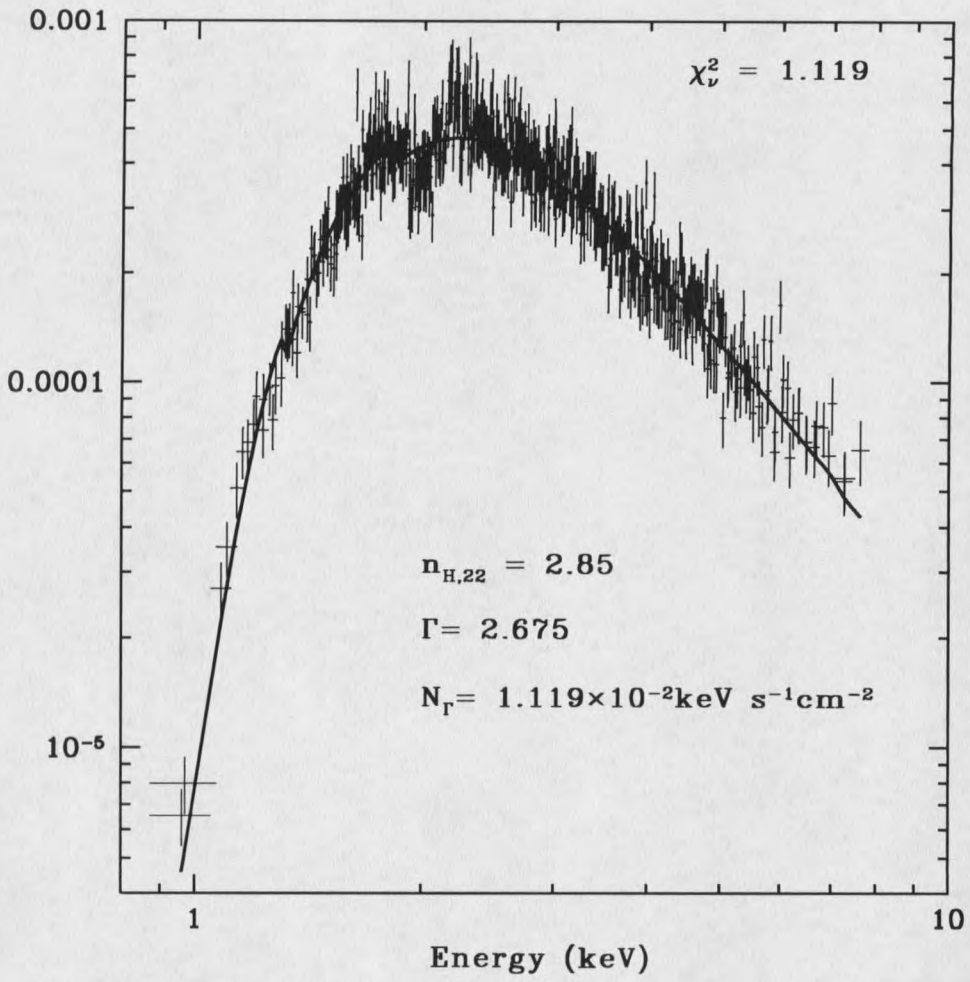

Figure 4.7: Combined fit of both *Chandra* observations with a single power-law model.

extension of the higher energy power-law found in the *RXTE* and BeppoSax data, and tested for the presence of a blackbody radiator. Overall, we found that this model also fit the data in all three cases with significant contribution from the blackbody. Our values for the fit parameters are summarized in table 4.2.

For the hydrogen column density, in both models the values for our fit are consistent with each other. For purposes of the phase resolved fits, we held n_H fixed at

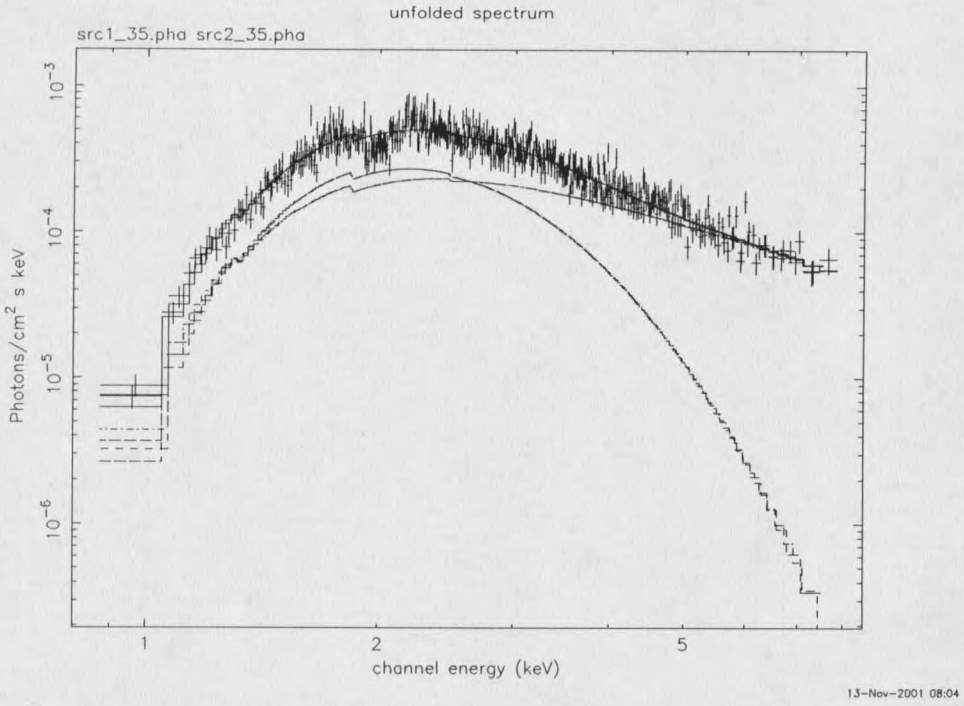

Figure 4.8: Combined fit of both *Chandra* observations with a blackbody plus power-law model.

the value that our combined fits of the two observations established. So for the single power-law model, we chose $n_{H,22} = 2.850$, and for the blackbody plus power-law model, we chose $n_{H,22} = 2.03$. Our fits using these values for $n_{H,22}$ are included in tables 4.1 and 4.2

Our Phase Resolved Spectral Analysis

We attempted phase resolved spectral analysis of SGR 1900+14, but the problem of relatively few counts restricted our analysis into two states, an *on* state, phases 0.1-0.6, and an *off* state, phases 0.6-1.1. Without benefit of a phase shift in the light curves, the best that we did was to show variability of the model parameters,

Table 4.2: Blackbody plus power-law fit for both observations. As before, the values in the parenthesis are for the best fit values using the fixed value for $n_{H,22}$

	Obs 1+2	Obs 1	Obs 2
$n_{H,22}$	$2.30^{+0.36}_{-0.19}$	$2.30^{+0.36}_{-0.29}$	$2.37^{+0.40}_{-0.35}$
		(2.30)	(2.30)
kT (keV)	$0.519^{+0.043}_{-0.077}$	$0.53^{+0.07}_{-0.12}$	$0.498^{+0.073}_{-0.083}$
		$(0.525^{+0.057}_{-0.028})$	$(0.511^{+0.031}_{-0.023})$
N_{BB} (km/10kpc)^2	$8.2^{+6.1}_{-1.6}$	$7.1^{+7.6}_{-5.8}$	$10.^{+11.}_{-5.}$
		$(7.1^{+3.1}_{-3.8})$	$(9.6^{+3.2}_{-3.9})$
Γ	$1.74^{+0.57}_{-0.40}$	$1.78^{+0.73}_{-0.56}$	$1.77^{+0.63}_{-0.78}$
		$(1.79^{+0.26}_{-0.25})$	$(1.66^{+0.31}_{-0.40})$
N_Γ (10^{-3} keV s^{-1}cm^{-2})	$2.0^{+3.5}_{-1.0}$	$2.3^{+6.1}_{-1.5}$	$2.0^{+4.0}_{-1.5}$
		$(2.3^{+1.2}_{-0.8})$	$(1.6^{+1.1}_{-0.8})$
χ^2	419.1	217.3	175.5
		(217.3)	(175.7)
χ^2_ν	1.058	0.997	1.014
		(0.992)	(1.009)

attempting to make a correspondence between them and the light curves.

For our power-law model, the hydrogen column density had been fixed at the phase integrated value, $n_{H,22}$=2.85. Our results of the phase resolved fits are presented in table 4.3. We saw a clear variation on both fitting parameters for the first obser-

Table 4.3: Phase resolved spectral results for power-law model with $n_{H,22}$ fixed at the phase integrated value of 2.85.

Parameter	Obs 1 on	Obs 1 off	Obs 2 on	Obs 2 off
Γ	2.54±0.05	2.69±0.05	2.72±0.05	2.68±0.06
N_Γ	0.96±0.05	1.08±0.06	1.08±0.06	$1.03^{+0.06}_{-0.03}$
χ^2	89.9	80.0	70.6	70.3
χ^2_ν	1.52	1.43	1.57	1.60

vation, but there was no detectable variation for the second observation beyond the uncertainty of the fit parameters. The significance of the 2σ variation of the power-law index is interesting, perhaps suggesting a distinctively softer spectrum when the

pulsar is in its *off* state. The less than 1σ variation present in the second observation had one obvious explanation: the second observation has much fewer counts than the first observation creating much more uncertainty in our fit parameters. Our larger values of χ^2_ν in the second observation were suggestive of this since the lower number of counts lead to more uncertainty and generally poorer fits.

For our blackbody plus power-law model the variation of the parameters vanishes within the uncertainty. The act of us adding two more free parameters to the fitting, increased the uncertainty because of the dependent nature of the fit variables. Subsequently, we could not claim anything regarding the blackbody plus power-law model with regard to its variability.

Discussion

Our results for period and period derivative are interesting. Using the results of Woods et al. (2001), we found that the resulting period would be lower by up to 7 ms. Similar results are apparent when we extrapolated our best fit period derivative back to their results. Since there has not been an event comparable to the August 1998 flare since then, we doubt that the discrepancy could be accounted for using a glitch model. We did notice that the pre-flare spin down rate of 8.2×10^{-11} s s^{-1} does give an expected period, when extrapolated forward to the *Chandra* observation times, closer to our 2001 results. Further investigations of the behavior of the period and period derivative should give some interesting results.

Our light curves for the two observations show little or no difference between the two observations. The four peak structure found in the 1998 *ASCA* observation (Hurley 1998c, figure 3) is not apparent in either observation. We speculate that the structure has simplified due to the giant flare in 1998, or the *Chandra* observations occurred after a burst event while the *ASCA* observation occurred before the May 1998 burst. Furthermore, *ASCA* had poor spatial resolution compared to *Chandra*, so the complex structure could be the result of background. Making any definite claims about the difference that we found between the light curves is limited by counting statistics. The 75% probability that the two light curves between 5.0-6.0 keV are different is exciting since the overall structure appears to change between the two observations. We are attempting a more detailed statistical analysis to determine if there is indeed a difference. Furthermore, the longer *Chandra* observation that is scheduled should show if the variability in shape persists over time, and the higher counting statistics for the longer observation could make it easier to show a statistical difference.

Our changes in the pulsed fraction between the two observations were not reported by any of the authors who have recently reported the results on these two public domain observations (Fox et al. 2001, and Kouveliotou et al. 2001). Kouveliotou et al. (2001) reported pulsed fractions for the first observation of 16.2%, for the 0.5-7.0 keV range, while our analysis showed a 27.1% pulsed fraction over a similar range. We note a similar difference for the second observation, their value of 14% versus our value of 29.3%. No energy resolved pulsed fractions were reported by either of the

authors so the nature of the differences between our analysis and their analysis can not be determined. Within the statistical error of the pulsed fraction, we find only the difference between the two observations in the 5.0-6.0 keV band. The possible energy dependence of the pulsed fraction may favor a two component model, but a proof will have to wait for a longer observation and a more detailed analysis of the existing data.

Two models used for spectral analysis by Fox et al. (2001) and Kouveliotou et al. (2001), and our analysis show no significant difference. For the single power-law model we find no proof of a change in power-law index between the two observations; furthermore, the power-law normalization also does not vary more than 1σ. These results are consistent with the 1998 *ASCA* observation (Hurley et al. 1998c). There is a difference, however, the 2001 *Chandra* observations show a significantly higher value for the hydrogen column density than the 1998 *ASCA* observations. We believe that the difference can be attributed to fitting, rather than anything physical.

For the blackbody plus power-law, the spectral analysis gives nearly identical results for both observations. Kouveliotou et al. (2001) showed that the temperature is lower if a certain range of data, 1.8-2.5 keV, is ignored because of the Si K edge from the detector and the Ir K edge from the mirror. Their result was 0.46 keV, and we confirmed their results; however, the uncertainty in our temperature without ignoring this range of data includes their result, and we find no evidence of excessive residuals at either the Si K edge or at the Ir K edge. Our radius of the blackbody at 5 kpc is between 1.3 and 1.9 km, which may indicate that the blackbody component is

a hot spot rather than radiation from the stellar surface as a whole; however, Perna et al. (2001) reports that their magnetar model to fit the *ASCA* data for SGR 1900+14 gives a radius near 10 km.

Our phase resolved results showed little because of poor counting statistics. Fox et al. (2001) showed that the power-law index in the single power-law model would vary significantly with phase using six phase bins. We found similar results for five phase bins, if the power-law index and normalization were treated as independent variables for the purposes of computing error. But, by adopting two free parameters that are dependent (Lampton et al., 1976), our power-law index did not vary from phase to phase within its uncertainty. An interesting result appeared in our phase resolved results for the first observation when two phases were used, one representing the *on* state, and the other representing an *off* state. We found a power-law index that had a phase shift that was significant to 2σ, our normalization showed a 1σ variation. The variation disappears during the second observation. The variable index may indicate that there are harder X-rays present in the first observation's *on* state.

We tried other models without success, but the list of possible models is far from exhausted. Overall, with our current results, the claim that SGR 1900+14 is a magnetar has been strengthened. Our energy dependent pulsed fraction is the easiest to explain with the magnetar case, being the variation of both the thermal and non-thermal components having a pulse. Furthermore, the blackbody plus power-law model does explain the data, suggesting a thermal component being visible.

CHAPTER 5

CHANDRA OBSERVATIONS OF 1E1207.4-5209

Introduction

Being a radio quiet compact central object of the supernova remnant (SNR) PKS 1209-51/52, 1E1207.4-5209 is a relatively newly discovered isolated neutron star. It is in a class of objects that are the compact central objects (CCO) of SNR, being either neutron stars, or black holes. These objects are typically soft in the X-rays which is apparently thermal. Often there is a lack of an optical counterpart and a lack of visible pulsar activity. Furthermore, the periods of these objects, when detected, range from 6 to 12 s, being much longer than the periods of radio pulsars (Zavlin et al., 2000). Some authors put these in a subclass of AXP (e.g., Mereghetti & Stella, 1995, and Gotthelf & Vasisht, 2000), which have been interpreted as isolated magnetars or accreting neutron stars with low magnetic fields.

Measuring the period of these sources and getting their spectral details has become important toward determining the nature of these objects. For example, the Cas A SNR CCO has not yet had a period determined (Pavlov et al., 2000, Chakrabarty

et al., 2000, and Umeda et al., 2000). RCW 103 has a very long period of 6 hours (Garmire et al., 2000). The Puppis A CCO has not had a period determined (Pavlov et al., 2000).

Earlier Observations and Results

The point source 1E1207.4-5209 associated with PKS 1208-51/52 was discovered by the *EINSTEIN Observatory* in the early eighties (Helfand & Becker, 1984), though no spectral details and timing were apparent from this observation. It is localized 6' off-center in the 81' diameter SNR. Later, 1E1207.4-5209 was observed by *ROSAT*, *ASCA*, and finally *Chandra* observed it in January of 2000.

Mereghetti, Bignami & Caraveo (1996) and Vesisht et al (1997) used the combined *ROSAT* and *ASCA* observations to establish a blackbody fit with kT$\sim$0.26 keV. The radius would be 1.5 km at 2 kpc distance, suggesting that the radiation was from hot spots on the neutron star surface. Later, Zavlin, Pavlov, & Trümper (1998) did a reanalysis of this data, using a hydrogen atmosphere model. They found that a typical neutron star mass and radius, $1.4M_{\odot}$ and 10 km, are obtained with a neutron star surface temperature of kT_{eff}= 0.12-0.16 keV and a distance of 1.6 to 3.3 kpc. Their blackbody results were reasonable in terms of temperature, kT_{eff}=0.36-0.40 keV, but the distance, 11-13 kpc, was large compared to other distance measurements.

Chandra Observation and Previous Results

In January of 2000, *Chandra* observed 1E1207.4-5209 in CC mode for 33 ks. The timing resolution allowed the period of the neutron star to be determined. Zavlin et al. (2000) established the period to a confidence level of 5.5σ. The period was found using the Z_1^2 statistic, and was found to be P=0.42412924 s $\pm$ 0.23 μs.

A light curve was also computed at this period. Their results showed a wide pulse profile with a low pulsed fraction at all energies. The strongest pulsed fraction is found in the 0.1-1.0 keV range. The energy dependence of the shape of the light curve appears to be slight, but gives no indication to the nature of the object.

Our New Results from the *Chandra* Observation

Our new goals for the analysis of the *Chandra* observation of 1E1207.4-5209 were focused on the spectral analysis of the collected data. Since Zavlin, Pavlov, & Trümper (1998) established that the most reasonable results for the combined *ROSAT* and *ASCA* data was a hydrogen atmosphere, we wanted to see if the same conclusion would be forthcoming from the *Chandra* analysis. Furthermore, because of the excellent timing resolution of the *Chandra* CC mode, we wanted to perform a preliminary phase resolved spectral analysis to see the variation of spectral components with phase.

Furthermore, the simplicity of the previous results as being a single blackbody radiator, or hydrogen atmosphere, suggested that we should look for other spectral

features which are not present in the lower resolution spectra of *ROSAT* and *ASCA*.

Results of Our Timing Analysis

We verified the period and nature of the light curve found by Zavlin et al. (2000), using the procedures outlined in the previous chapters. Furthermore, the CC mode time corrections developed by Allen (2000) were confirmed with the script by Tennant (2001), as our use of the Tennant (2001) script gave no discrepancy with the previously reported period of 1E1207.4-5209 .

Results of Our Phase Integrated Spectral Analysis

Our phase integrated spectral analysis turned out to be somewhat difficult, as no simple model would fit the data over the entire range. The most promising of all the models that we tried happened to be the blackbody model, having the best fit statistic; however, it did not fit the data. We found a spectral feature between 1.2 and 1.5 keV that prevented fitting. Our discovery of this feature was accidental. Since our fits were not converging, we had suspicion of a poor fit because of either the Si or Ir edge associated with the telescope; however, we accidentally ignored 1.2-1.5 keV range. After discovering the successful fit, an examination of the residuals of our ignored range of data with the successful fit parameters showed a large deviation in the 1.2-1.5 keV range. Figure 5.1 shows the deviation created by the spectral feature.

By ignoring the feature, we found a blackbody model does fit the spectrum. Our analysis found the hydrogen column density to have a value of $5.5^{+1.4}_{-1.3} \times 10^{20} \mathrm{cm}^{-2}$, a

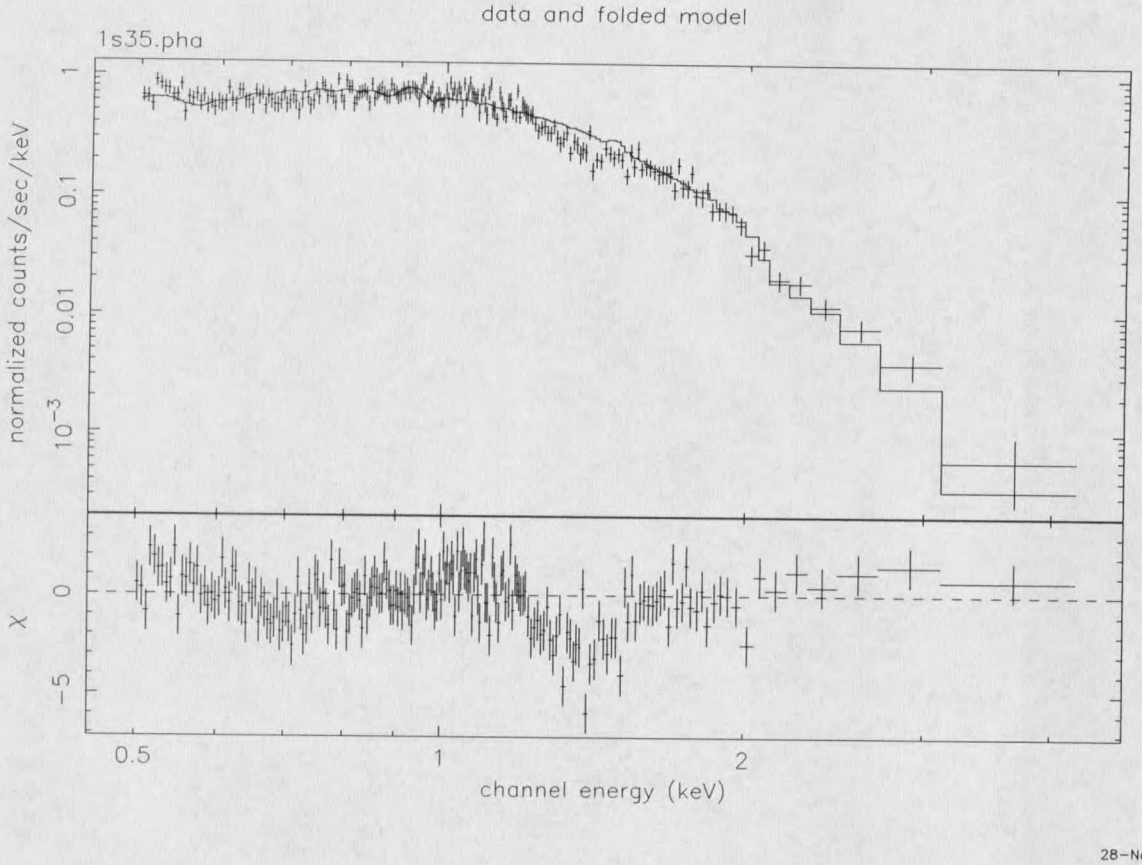

Figure 5.1: The spectrum of 1E1207.4-5209 *Chandra* data shows the absorption feature which prevented fitting. There is a large deviation in the residual in the range 1.2-1.5 keV.

little low to be in good agreement with any of the previous results. Our blackbody temperature was $0.255^{+0.006}_{-0.005}$ keV. Finally, our blackbody normalization was $58.9^{+8.2}_{-7.1}$ $(\mathrm{km/10kpc})^2$. Assuming a neutron star effective radius of 10 km, our distance to the source became d=12-14 kpc, which we regarded as an unreasonable value. Our analysis became that of characterization of the absorption feature so as to properly take it into account during fitting.

To begin to understand the nature of the absorption feature, we chose an absorp-

tion edge model from the xspec multiplicative models:

$$M(E) = \begin{cases} 1, E < E_o \\ e^{-\tau(E_o/E)^3}, E > E_o. \end{cases} \tag{5.1}$$

$M(E)$ is a multiplicative factor which adjusts the flux by $M(E)F(E)$ where $F(E)$ is the flux of the model to which it is applied. The parameter E_o is the threshold energy of the absorption edge, and τ is the absorption depth at the threshold energy. We multiplied our blackbody model by this factor to account for the absorption feature.

Including the absorption edge, we found the model parameters to be n_H=2.4-5.6$\times 10^{20}$ cm^{-2}, kT=0.26-0.28 keV, and N=38.8-51.2 (km/10kpc)^2. The threshold energy for the absorption edge was $1.264^{+0.017}_{-0.021}$ keV. The absorption depth parameter, τ=0.560$\pm$0.10, which decreases the flux by a factor of 0.57 at the threshold energy. For a 10 km effective radius neutron star, we found the distance to be 14-16 kpc. Consequently, the bolometric flux was found to be 2.5-2.8$\times 10^{-12}$ ergs cm^{-2} s^{-1}. We present the best fit model with the absorption edge in figure 5.2.

We attempted several other models to account for the absorption edge. None of them gave conclusive results. Most notably, we attempted a variable absorption model which accounted for absorption of elements in the column density that vary from the solar abundance. Using this model, we found a very large magnesium concentration; however, the value of the concentration of magnesium pegged at the value of 1000 times solar abundance which is the extreme value for that model. We determined that this was inconclusive because of the extreme overabundance plus the absorption

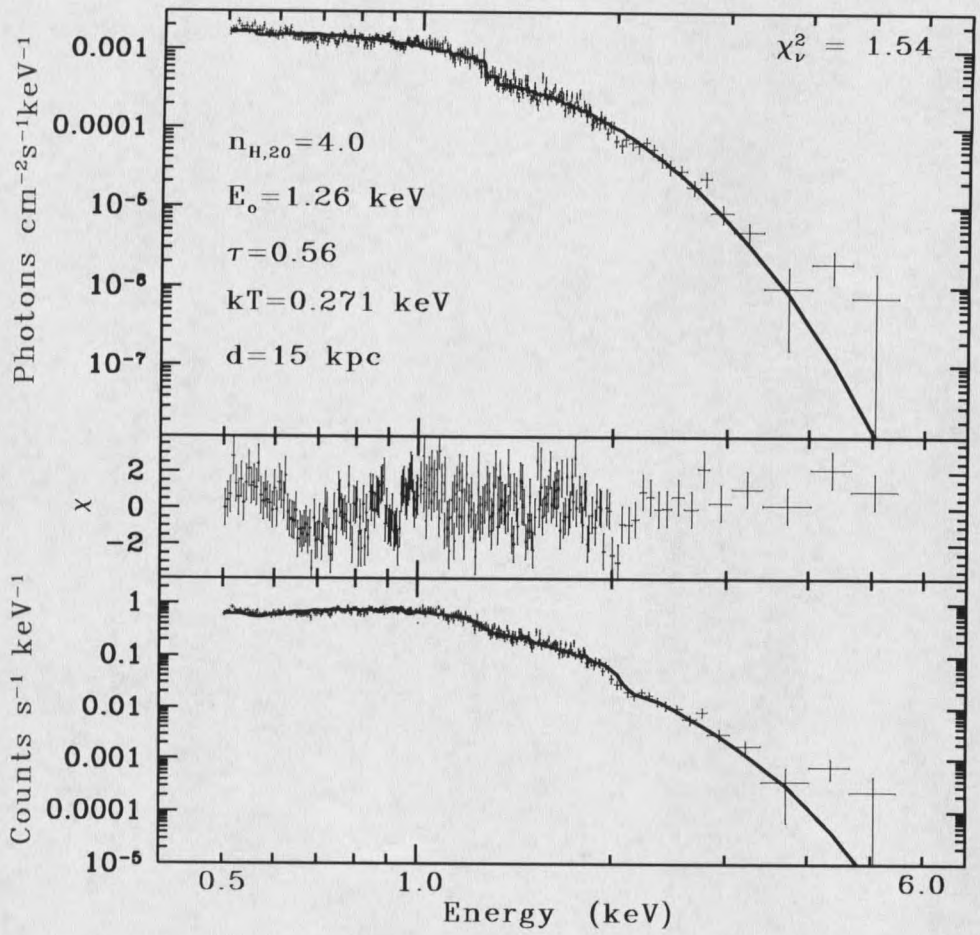

Figure 5.2: Fit of absorption edge model for 1E1207.4-5209. The last data point shows the beginning of the background dominated region, but was ignored for fitting purposes. The edge can be seen in the top panel where the best fit line steps down.

edge associated with magnesium, E_o=1.31 keV, was outside of the uncertainty of our absorption edge model best fit.

Results of Our Phase Resolved Spectral Analysis

For the purpose of phase resolved spectroscopy, we assumed that the hydrogen column density to be fixed at all phases at the phase integrated value. We based our

choice upon the fact that the time variability of the hydrogen absorption should not be on the same time scale as the period of the source. Furthermore, the absorption edge appeared to be present in all of the spectra for the the various phases so its value was assumed to be fixed in energy and in size. We assumed it to be a feature of the nebula, but it still could be associated with the source; however, our attempts to fit it in phase resolved spectroscopy were unsuccessful because the uncertainty of all model parameters became too large.

Both the temperature and normalization of the blackbody were fit to each of the spectra for each phase range, using 5 different phases. We present our results in figure 5.3. The temperature and the blackbody radius were anti-correlated, as we expected since the hotter surface areas would be smaller in size than the cooler areas. The variability of the temperature, though not as strong as the variability in the radius, showed that the overall surface temperature does not vary too much over the surface.

We noticed that similar result was apparent when the radius is held fixed at 10 km, though the bolometric flux was correlated with the temperature rather than being anti-correlated. In both cases, we found that the resulting bolometric flux had the same overall shape; furthermore, the pulsed fraction for the flux was $\sim$7% in both cases.

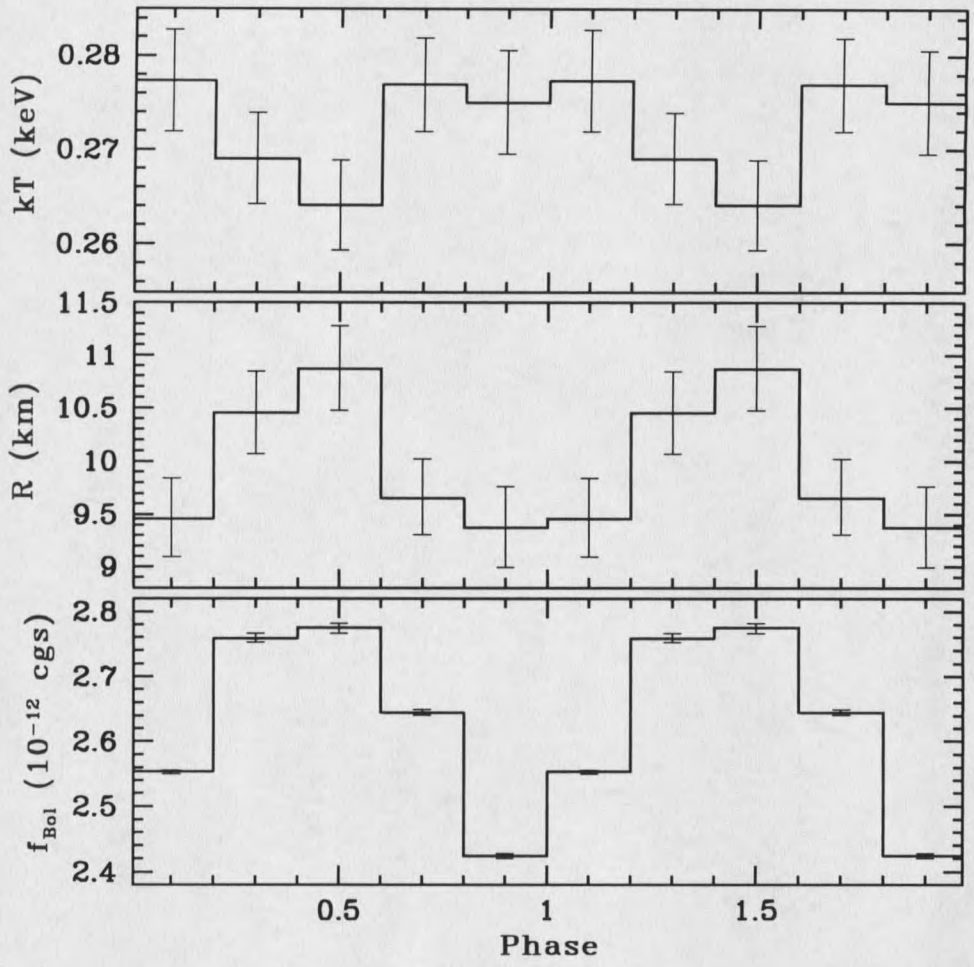

Figure 5.3: Phase resolved spectral fits for 1E1207.4-5209 . The cgs units of flux is erg $s^{-1}cm^{-2}$. The blackbody radius assumes a distance of 15 kpc.

Discussion

Other than the absorption feature, we found no evidence for additional components to the 1E1207.4-5209 spectra. There was no indication of either a missing magnetospheric power-law component nor was there any evidence of an additional thermal component. If either such component exists, the *Chandra* observation was too short to show them.

The blackbody results for the spectral fits are consistent with the values obtained by Zavlin, Pavlov, & Trümper (1998) found for the same model with the *ROSAT* and *ASCA* data. With this result, we expected that the hydrogen atmosphere results for the *Chandra* observation will also give similar results, thereby confirming the *ROSAT* and *ASCA* result. We estimate that the effective temperature should be a little lower, kT_{eff} ~0.08-0.11 keV, using the appropriate distance established from the *ROSAT* and *ASCA* result.

The absorption feature at 1.26 keV is close to the magnesium absorption edge, 1.3 keV. There is also the Mg Kα line at 1.25 keV which might be part of the structure if we assume that it is an absorption line. As to the absorption edge, little can be done with this data as it would need more counts than we had with this observation. For purposes of fitting the phase resolved spectra, we considered the edge as part of the absorption from the nebula or the interstellar medium, and not regarded as from the source. The existence of this feature will be determined by another *Chandra* observation of 1E1207.4-5209 scheduled in December, 2001. If it appears to be present, a more detailed analysis may be possible using the data from this and the new observation. We have two current explanations for the absorption feature, one is noise from the telescope, the second is absorption from the nebula. Our variable absorption modeling using different absorbing elements has been inconclusive. Our fits have shown a huge, $> 10^3$ times solar abundance, overabundance of magnesium, but it is at the limits of the model's range of accuracy so it gives no definite conclusion.

Assuming our modeling of the absorption feature is correct, the phase resolved

spectral results are interesting. The results show that the X-ray variability of 1E1207.4-5209 is thermal in origin. It can be best described as a moderate temperature distribution over the neutron star surface. There is no evidence of a hot-spot nor a non-thermal magnetospheric component. Our variability of the unabsorbed flux is a little low, only showing a pulsed fraction of $\sim$7%. A hydrogen atmosphere model may fit the data better and predict a larger pulse. Therefore, as a next step the data will be fit to a hydrogen atmosphere model. Furthermore, even without the hydrogen atmosphere model, we could begin modeling the temperature distribution using a magnetic dipole of Greenstein and Hartke (1983) or the off-center magnetic dipole of Halpern and Ruderman (1993). The overall shape of the distribution suggests that a multi-pole magnetic field, such as those used by Page and Sarmiento (1996), will not be necessary, but, at this early stage, we cannot definitely determine whether or not the multi-pole model will be necessary to explain the data. However, to determine the field strength, we do require the period derivative that is expected from the next observation.

CHAPTER 6

FUTURE OBSERVATIONS

Future Missions

Chandra X-ray observatory had its primary mission extended by at least 6 years, giving it the advantage of continued monetary support over that period (Weiler, 2001). *XMM-Newton* will also continue to be used extensively over that period. Furthermore, the Japanese mission *ASTRO-E* is being rebuilt after a catastrophic launch failure in 2000. So in the foreseeable future, there will be at least one X-ray observatory available.

In the future there are a number of exciting X-ray missions in various stages of development. One of the most exciting is *Constellation-X*, an X-ray interferometer giving outstanding advances in spatial, spectral, and timing resolution. For instance, weak spectral lines that are invisible to *Chandra* will stand out in a relatively short observation. The hopeful launch date for this fantastic instrument is in 2011.

Future Observations of Neutron Stars

Chandra has opened up some fantastic opportunities for neutron star observations. New sources are being detected due to the large effective area of *Chandra*, and more are certainly going to be found. Many controversies surrounding existing objects are being resolved.

As mentioned in chapter 5, 1E1207.4-5209 is due to be observed again in early December of 2001. Unless something completely unforeseen happens, a period derivative will be determined for that object. Furthermore, the nature of the spectral absorption feature between 1.2 and 1.5 keV will be determined as to whether it is inherent to the source or to the January 2000 observation. As more data becomes available, more details regarding the phase resolved spectroscopy can be improved.

XMM-Newton has also observed PSR B1055-52, though the results are yet to be released. The slope of the power-law component should be the most interesting result since *XMM-Newton* has better effective area at the higher energies than does *Chandra*. The phase resolved behavior of all of the components should also be improved as a result. There are no planned further observations of PSR B1055-52 by *Chandra*, though an HRC observation should be done, if possible, to determine if there is a compact nebula associated with this source.

The magnetar, SGR 1900+14, is being observed by *Chandra* again, with a longer exposure. Unless there is another burst, this observation should give a detailed look at the SGR in quiescence. A long observation might also determine if the blackbody

component is pulsing, in addition to the power-law component.

Overall, there are many new and exciting observations for *Chandra*. Many observations will determine if there are more non-standard cooling candidates besides Vela and RCW 103 (see chapter 7, for details). Furthermore, the surface temperature should be measured for many more isolated neutron stars, giving a better understanding of neutron star cooling. Additional observations might settle the issue regarding the lack of spectral lines that should be seen on neutron stars.

CHAPTER 7

COOPER PAIR NEUTRINO EMISSIVITY AND COOLING OF NEUTRON STARS

Introduction

In the core regions of a neutron star, the density of the material exceeds nuclear density. At these ultra high densities, constituent particles can form superfluids at relatively high temperatures, compared to terrestrial superfluids like liquid helium. Two fermions pairing in a superfluid is known as Cooper pairing. The superfluidity of particles in the core of the neutron star have a relatively well understood property of suppressing neutrino production processes associated with nucleons, pions, and other 'exotic' particles, thus changing the cooling curve for the neutron star. Superfluidity of the constituent particles is considered part of the conditions within the core in many cooling mechanisms considered in neutron star cooling theory; however, only recently, the fact that the formation and breaking of Cooper pairs themselves could produce neutrinos and thus affect the cooling mechanisms was rediscovered from the original work by Flowers, Sutherland & Ruderman (1979).

In this chapter, the effect of Cooper pair neutrino emission upon neutron star cooling will be presented. In the following section the theory behind superfluidity and cooper pair neutrino production will be discussed. This is followed by our exploration of the effects upon the standard cooling mechanisms, and the discussion of the important effect upon non-standard cooling. Finally, the results and their observational consequences will be discussed.

Theoretical Background

Recently, some additional neutrino processes have been suggested (Page, 1998). Of the new processes that have been suggested, we found the 'Cooper pair neutrino emission' to be the only one which gives a significant effect (Tsuruta & Teter, 2001). The neutrino emission due to the breaking and formation of Cooper pairs, takes place right after the stellar core temperature decreases below the critical superfluid temperature, T_{cr}, though it will soon decrease exponentially (Flowers, Ruderman, and Sutherland, 1979). The net effect is to enhance the neutrino emission right after the superfluidity sets in.

As the star cools after the supernova explosion and the stellar core temperature reaches below the superfluid critical temperature, T_{cr}, the core particles become superfluid. That causes exponential suppression of all neutrino processes involving core particles (nucleons, pions, etc.) which become superfluid. The net effect is that the star cools more slowly (the surface temperature and luminosity are higher) during the

neutrino cooling era (than in the absence of the suppression). The effects of superfluid suppression are well documented (see Tsuruta, 1998, and references therein). Many non-standard cooling situations are brought close to the standard cooling curve if the energy gap, and hence T_{cr}, are sufficiently high, while others will cause the cooling curve to deviate significantly from both standard and non-standard cooling without suppression. Furthermore, the superfluid state of the inner crust can also be a source of internal heating (Umeda et al., 1993, and Larson & Link, 1998). So, it follows that the thermal evolution depends greatly upon the superfluid model.

In general terms, the core temperature, T_o, of a neutron star evolves as

$$C_V \frac{\partial T_o}{\partial t} = -L_\nu - L_\gamma, \tag{7.1}$$

where C_V is the heat capacity of the star, L_ν is the neutrino luminosity from the interior of the neutron star, and L_γ is the photon luminosity from its surface. Both the core neutrino luminosity and the surface photon luminosity can be written as functions of T_o. If the neutron star cools primarily by neutrino emission from the core, then $L_\nu >> L_\gamma$, which we expect at early times; however, at later times, the photon cooling is expected to dominate and the relationship is reversed. Consequently, the early evolution of the star requires an accurate representation of the neutrino emissivity, luminosity per unit volume.

The neutrino processes for standard and non-standard cooling that we have considered are detailed in the following subsections, then the new process for Cooper

pair neutrino emissivity is discussed. However, since the Cooper pairing requires a superfluid, superfluid models will be considered in the last subsection.

Standard Neutrino Emission Mechanisms

There are many neutrino emission mechanisms, as outlined in chapter 1. The most important for standard cooling in the core are the processes developed by FM79. In the central core, they are the modified URCA neutrino, the neutron-neutron, and neutron-proton bremsstrahlung neutrino emissivities. The modified URCA is the strongest, followed by the two bremsstrahlung processes. They are given by

$$\varepsilon_{MU} \cong 2.7 \times 10^{21}\ f_{MU}(m_n^*, m_p^*, \rho)\ T_9^8\ erg\ cm^{-3}s^{-1}, \tag{7.2}$$

$$\varepsilon_{n-n} \cong 7.8 \times 10^{19}\ f_{n-n}(m_n^*, m_p^*, \rho)\ T_9^8\ erg\ cm^{-3}s^{-1}, \tag{7.3}$$

and

$$\varepsilon_{n-p} \cong 7.5 \times 10^{19}\ f_{n-p}(m_n^*, m_p^*, \rho)\ T_9^8\ erg\ cm^{-3}s^{-1}, \tag{7.4}$$

where ε_{MU} is the neutrino emissivity for modified URCA, ε_{n-n} and ε_{n-p} are the neutrino emissivities for the neutron-neutron and neutron-proton bremsstrahlung processes. The functions f_{MU}, f_{n-n}, and f_{n-p} are functions of effective neutron mass, m_n^*, effective proton mass, m_p^*, and density, ρ. The temperature is defined by $T_9 \equiv T/10^9$ K. In all cases, the rate of neutrino cooling is controlled by the coefficients, and the power of temperature. In the largest case the coefficient is $\sim 10^{21}$ erg $\mathrm{cm}^{-3}\mathrm{s}^{-1}$ for

the modified URCA process.

The modified URCA neutrino process is a modification of the beta decay and inverse beta decay of the free neutrons and protons in the core of a neutron star, $n + n \rightarrow n + p + e^- + \overline{\nu_e}$ and its inverse. These decays give off neutrinos and anti-neutrinos. Modified URCA is a modification of the direct URCA process for nucleons, which will be discussed with non-standard emission mechanisms.

The neutron-neutron and neutron-proton bremsstrahlung neutrino processes are scattering events which produce neutrinos. For the neutron-neutron bremsstrahlung neutrino process, the interactions are $n+n \rightarrow n+n+\nu+\overline{\nu}$ and the inverse. Similarly, the neutron-proton bremsstrahlung interactions are $n + p \rightarrow n + p + \nu + \overline{\nu}$ and the inverse. These processes result in slightly lower emissivities than the modified URCA process, but our cooling simulation will have all three processes included.

The other neutrino processes, that are included in our exact stellar evolution code, are the heavy ion URCA, the electron-ion neutrino bremsstrahlung, the plasmon neutrino, photo neutrino, and the electron-positron pair neutrino processes. The first three of these processes in the inner crust controls the surface temperature in the earlier stages of the evolution before the isothermal state is reached.

Non-standard Neutrino Emission Mechanisms

Depending upon the composition of the core, other drasticly fast processes may be present that produce neutrinos. Collectively, these are called non-standard neutrino emission mechanisms.

The fastest of the non-standard processes is the direct URCA neutrino process involving nucleons. It involves simple beta decay, $n \rightarrow p + e^- + \overline{\nu_e}$, and the inverse process. The neutrino emissivity for the direct URCA process is given by the equation,

$$\varepsilon_{DU} \cong 1.6 \times 10^{27} \; f_{DU}(m_N^*, \rho, \Theta_t) \; T_9^6 erg \; cm^{-3} s^{-1}, \tag{7.5}$$

where m_N^* is the nucleon effective mass (both the neutron and proton in this case), and Θ_t is the threshold factor (Tatsumi, 1995). By comparing with equation 7.2, it is clear that the direct URCA process for nucleons dominates for all reasonable core temperatures. In the non-standard cooling with direct URCA for nucleons, a neutron star will cool very rapidly. It can take place when the proton concentration is sufficiently high, $\sim$15% (Lattimer et al., 1991).

The next fastest non-standard cooling process is called the pion URCA process. The reaction is $n + \pi^- \rightarrow n + e^- + \overline{\nu_e}$ and its inverse. It is a similar process to the nucleon direct URCA, but it involves pions. The expression giving the emissivity for pion URCA is

$$\varepsilon_{\pi U} \cong 1.5 \times 10^{26} \; f_{\pi U}(m_N^*, \rho, \Theta_t) \; T_9^6 erg \; cm^{-3} s^{-1}, \tag{7.6}$$

where the parameters are the same for the direct URCA process involving nucleons (Tatsumi, 1995). Again, the comparison to equation 7.2 shows that pion direct URCA dominates over the standard cooling processes for all reasonable core temperatures.

The process can take place if the density is sufficiently high for a pion condensate to form in the core.

Similar arguments can be made for kaon and quark direct URCA process (Tsuruta and Teter, 2001). The processes will dominate the cooling of the neutron star in the core; however, the conclusion for quark cooling should be qualified as there are still many unknowns regarding a quark cooling process.

Cooper Pair Neutrino Emission Mechanisms

Leaving the choice of superfluidity aside until the next subsection, the superfluid state leads to an additional neutrino emission mechanism. When the Cooper pairs form and break apart, neutrinos are emitted by the process. The processes involved in the neutrino production are $\tilde{N} + \tilde{N} \rightarrow \nu + \overline{\nu}$, two quasi-nucleons annihilating into a neutrino pair (Yakovlev, Kaminkar, and Levenfish, 1999, YKL99 hereafter). The process is expected to occur because not all the nucleons will be in the superfluid state at just below T_{cr}, though as the temperature drops, more of the nucleons will be superfluid and thus suffer fewer collisions that break the pairs. By solving the complicated micro-physics, YKL99 developed the analytic expressions for the Cooper pair neutrino emissivity:

$$\epsilon_{cp} = 1.170 \times 10^{21} (m_N^*/m_N)(p_F/m_N c) T_9^7 N_\nu a F (erg\ cm^{-3} s^{-1}) \qquad (7.7)$$

where m_N^* is the nucleon effective mass, p_F is the Fermi momentum for the nucleons,

$T_9 = T/10^9$ K, N_ν=2 (for 2 neutrino flavors), a is a numerical factor depending upon the superfluid type and the interaction, and F is a function depending upon the gap energy of the superfluid.

The functions F, for the various superfluids, depend upon the gap parameter v which is given by

$$v = \frac{\Delta(T)}{k_B T} = f_x(\tau) \tag{7.8}$$

where $\Delta(T)$ is the gap energy for the superfluid, and $f_x(\tau)$ is a function of the critical temperature where $\tau = T/T_{cr}$ and x is the superfluid type A, B, or C. Subsequently, the simple expressions for the functions F are developed as

$$\begin{aligned} F_A = & (0.602v^2 + 0.5942v^4 + 0.288v^6) \\ & \times \left(0.5547 + \sqrt{(0.4453)^2 + 0.0113v^2}\right)^{1/2} \\ & \times exp\ \left(-\sqrt{4v^2 + (2.245)^2} + 2.245\right), \end{aligned} \tag{7.9}$$

$$\begin{aligned} F_B = & \frac{(1.204v^2 + 3.733v^4 + 0.3145v^6)}{1 + 0.3511v^2} \\ & \times \left(0.7591 + \sqrt{(0.2409)^2 + 0.3145v^2}\right)^2 \\ & \times exp\ \left(-\sqrt{4v^2 + (0.4616)^2} + 0.4616\right), \end{aligned} \tag{7.10}$$

and

$$F_C = \frac{0.4013v^2 - 0.043v^4 + 0.002172v^6}{1 - 0.2018v^2 + 0.02601v^4 + 0.001477v^6 + 0.0000434v^8}, \tag{7.11}$$

which are for superfluid types A, B, and C respectively (YKL99). Equations 7.7 through 7.11, along with the superfluid model, establish all that is needed to compute the neutrino emissivity for the Cooper pair process. In turn, v can be written as functions of the superfluid critical temperature so that v_A, v_B, and v_C, are given by (YKL99)

$$v_A = \sqrt{1-\tau}\left(1.456 - \frac{0.1507}{\sqrt{\tau}} + \frac{1.764}{\tau}\right), \tag{7.12}$$

$$v_B = \sqrt{1-\tau}\left(0.7893 + \frac{1.188}{\tau}\right), \tag{7.13}$$

and

$$v_C = \frac{\sqrt{1-\tau^4}}{\tau}(2.030 - 0.4903\tau^4 + 0.1727\tau^8). \tag{7.14}$$

Figure 7.1 shows the neutrino emissivities as calculated using equations 7.7 through 7.14 for a neutron superfluid. The superfluid critical temperature, $T_n^{cr} = 10^9$ K, was chosen as an example to show the cut off of the emissivity as the temperature goes above the critical temperature. The three superfluid types A, B, and C, denote the pairing for the superfluid, $^1S_0$, $^3P_2(m_J = 0)$, and $^3P_2(m_J = 2)$, respectively. The singlet and triplet states for the Cooper pairs are established as free parameters of choice, while the critical temperature will be calculated from the superfluid model.

The magnitude of equation 7.7 for the Cooper pair emissivity compares well with the magnitude of equation 7.2 for the modified URCA emissivity at a temperature of 10^9 K. Depending upon the superfluid gap and corresponding T_{cr}, Cooper pair neutrino emissivity will have a dominant roll in the thermal evolution over a range

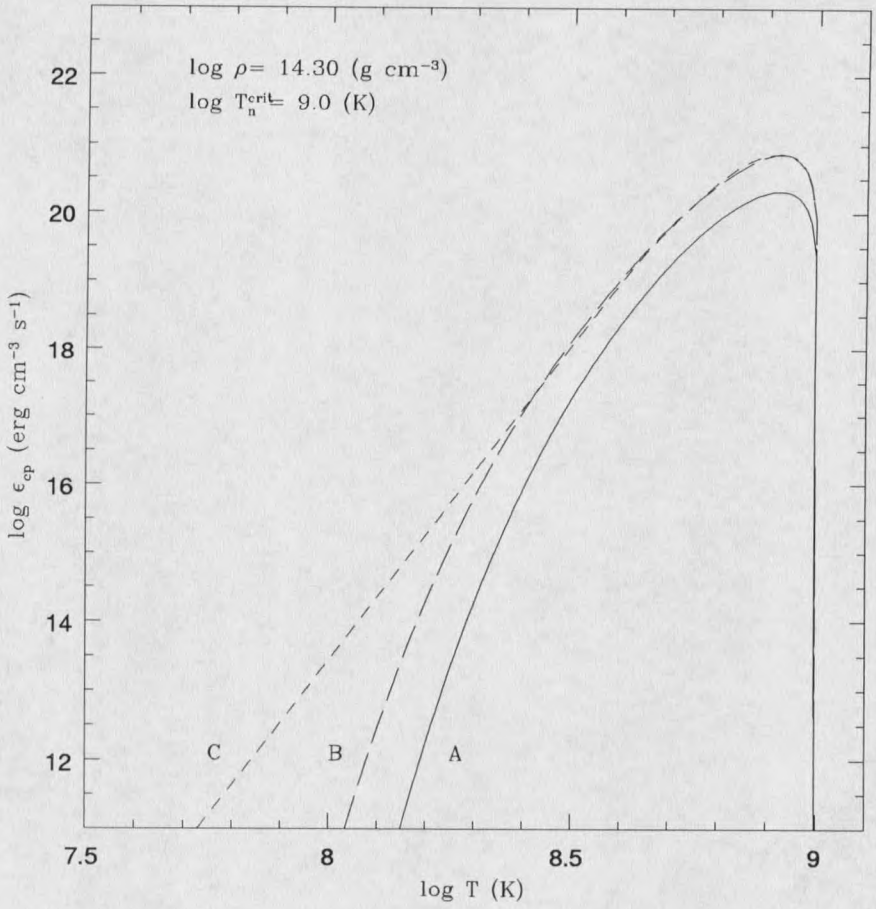

Figure 7.1: Neutrino emissivity for neutron superfluidity of types A, B, and C. The superfluid critical temperature is chosen to be $T_n^{cr} = 10^9$ K, and the Cooper pair emission mechanism is shut down beyond T_n^{cr} because of no superfluidity above the critical temperature.

of temperatures. Figure 7.2 shows this effect. At nuclear density the Cooper pair neutrino emissivity becomes dominant above temperatures of $10^{8.2}$ K, modifying the cooling curve. The effect will be different depending upon the density because the two processes have different density dependence.

The composition of the core is expected to be predominantly neutrons (with several percent of protons, electrons, and muons) if the density is moderate ($\rho <\sim 10^{15}$ g

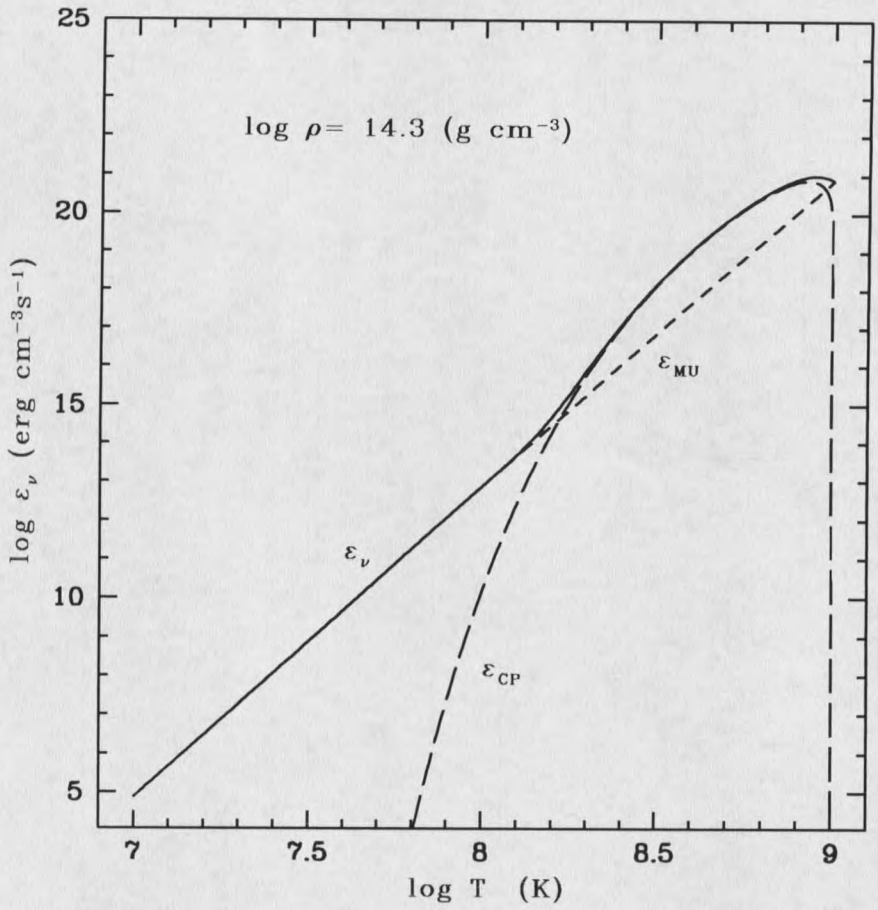

Figure 7.2: Comparison between modified URCA and type B superfluid with superfluid critical temperature of $T_n^{cr} = 10^9$ K.

cm^{-3}). For higher densities hyperons, pions, kaons, quarks, etc. could dominate the central core. Both observational and theoretical considerations support the view that the neutron star mass is close to 1.4 $M_\odot$ (Brown, Weingartner, and Wijers, 1996); consequently, the modeling will be done using a medium equation of state (EOS), FP, with masses near 1.4 $M_\odot$. To understand the effect that the EOS has upon the expected behavior, a stiffer PS EOS at 1.4 $M_\odot$ will also be tested. The softer EOS is not shown because it is most likely excluded (see discussion at the end of this

chapter).

The expected nature of the superfluid will be dependent upon the density, and the particle species. For the inner crust region, $\rho_{nuc} > \rho > \rho_{nd}$, where $\rho_{nuc} \sim 2.4 \times 10^{14}$ g cm^{-3} is nuclear density and $\rho_{nd} \sim 4 \times 10^{11}$ g cm^{-3} is neutron drip density, there will be no free protons; however, neutrons will form a singlet $^1S_0$, type A, superfluid. For $\rho > \rho_{nuc}$ free protons can appear and form a singlet $^1S_0$, type A, superfluid. Furthermore, the singlet state for neutrons at high density becomes repulsive rather than attractive at larger than nuclear densities; however, the triplet $^3P_2$ state is attractive in this regime. Consequently, a triplet $^3P_2$, type B or C, superfluid is used for superfluid neutrons in the core.

Superfluid Models

What remains is to choose the superfluid model which describes the behavior of the particles in the core, depending upon the state of matter in the core. If the core is nucleons, then the superfluid will be different than a core composed of primarily some other particles such as pions, kaons, hyperons, or quarks.

There are many superfluid models in use with varying gap energies and corresponding T_{cr}s. Figure 7.3 shows the density dependence of various superfluid models that are under consideration, for the ^{3}P$_2$ superfluids taken from Tsuruta 1998. There are a wide range of critical temperatures represented. For example the HGRR superfluid model has gap energy such that T_{cr} is large, greater than 10^9 K.

In general superfluids have the property to suppress the neutrino emission mech-

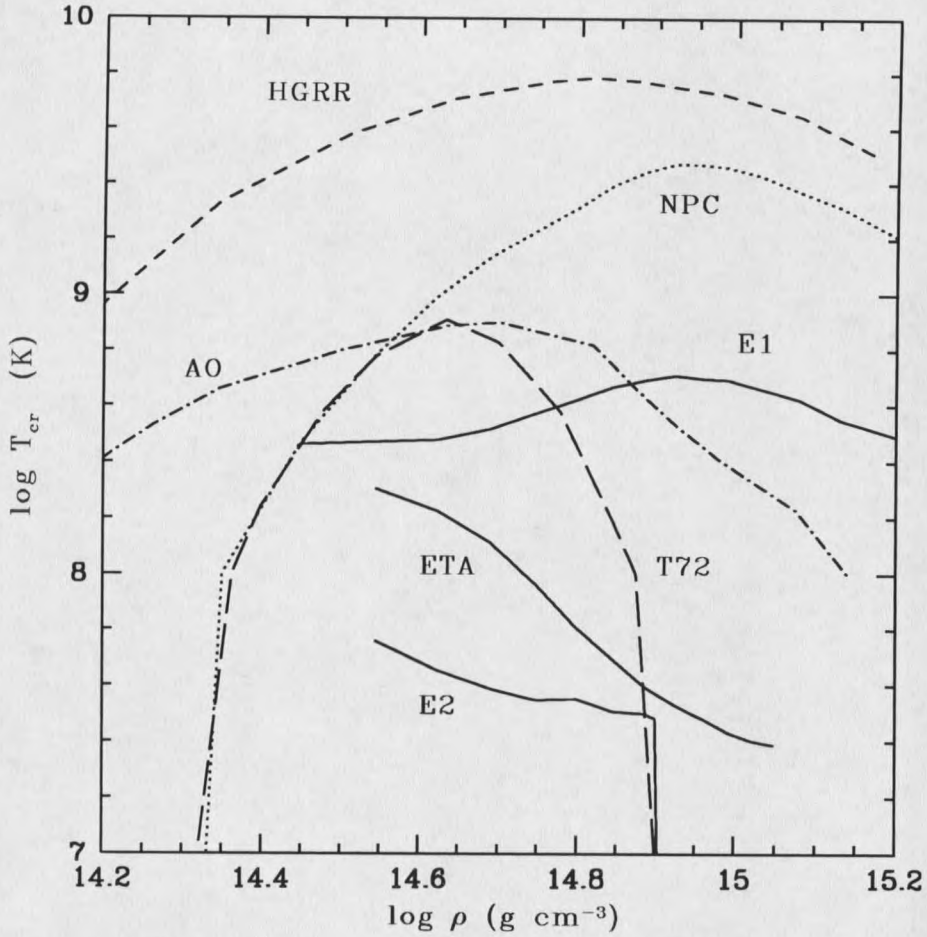

Figure 7.3: Comparison between several example superfluid models. For reference nuclear density is 2.8×10^{14} (g cm^{-3}). The models with solid lines are for pions, while all others are neutron $^3P_2$ superfluids.

anisms. The superfluid reduces the emissivity of the process by $\exp(-aT_{cr}/T)$ when the temperature is below T_{cr}.

The superfluid gap energy is strongly model dependent. Among other things, it can depend upon the effective mass of the particles that are to form the superfluid. In general, the superfluid gap energy decreases as the effective mass decreases.

The superfluid model of Amundsen and Ostgarrd (1985, AO hereafter) computes

the gap energy using a density dependent neutron effective mass. Similarly, Takatsuka (1972, T72 hereafter) had developed another superfluid model independently, using the same assumption. The AO model has slightly larger gap energies than those used in the T72 model, and it extends over a wider density range.

Some models, such as the one by Hoffberg et al. (1970, HGRR hereafter), did not use the density dependent effective mass. The HGRR model assumes that the effective neutron mass is constant with $m_n^*=m_n$.

For superfluidity in a pion core, Takatsuka and Tamagaki (1980, TT80 hereafter, and 1982, TT82 hereafter) developed superfluid models. One model (ETA) uses a variable pion effective mass as was used in the earlier T72 model for neutrons, but effective mass does not significantly decrease for densities above $3\rho_{nuc}$ (TT80). Another model (E1) uses a gap energy calculated of $m_n^*(\pi)=0.8m_n$ (TT82). Furthermore, they also developed a model (E2) in which $m_n^*(\pi)=0.7m_n$ (TT82). From figure 7.3 the E1 and E2 models are seen as upper and lower limits to the critical temperature of the pion superfluid. Taking into consideration the unknowns associated with the gap energy, the E1-ΔT model was developed to explore the possibilities between the upper and lower limits imposed by the E1 and E2 models (Umeda, et al., 1994). The solution was to multiply the energy gap of the E1 model by a factor $10^{-\Delta T}$, where ΔT is a free parameter allowed to vary but is constrained by the limits imposed by the gap of the E2 model. Therefore, the uncertainties of the pion superfluid can be estimated within the two extremes.

Effects Upon Standard Cooling

We chose, for neutrons in standard cooling, the superfluid model from Takatsuka 1972(hereafter referred to as T72) where the density dependent effective mass of neutrons, m_n^*, is used, since we considered it to be the most reliable for neutron matter.

Figure 7.4 shows our resulting cooling curves with standard cooling which include the Cooper pair emissivity We adopt a T72 superfluid, an FP EOS, and a mass of 1.4 $M_\odot$. The data points are labeled and summarized in figure 1.1 and table 1.1. Overall, we find a small difference. There is a large deviation between $10^{0.5}$ years and $10^{3.0}$ years. Only Cas A lies in this region, and it is still not certain if Cas A is an isolated neutron star. Furthermore, the Cas A upper limit is still consistent with either curve. The problem, however, comes from the Vela pulsar. Since Vela's luminosity is so low, standard cooling with or without Cooper pair neutrino emissivity will not explain its low luminosity. Variation of mass with standard cooling has been explored by Nomoto and Tsuruta (1987) showing that even masses as low as $1M_\odot$ and as high as $2M_\odot$ show little variation in their cooling curves. Furthermore, RCW 103, a historical pulsar, has been recently observed with *XMM-Newton* and its upper limit has been lowered to the point where standard cooling will not explain it (Slane, 2001).

For stiffer equation of state, PS, the cooling curves are shown in figure 7.5. It is clearly seen that the presence of the Cooper pair emissivity changes the evolutionary track for the PS EOS; however, the new track does not explain the Vela pulsar.

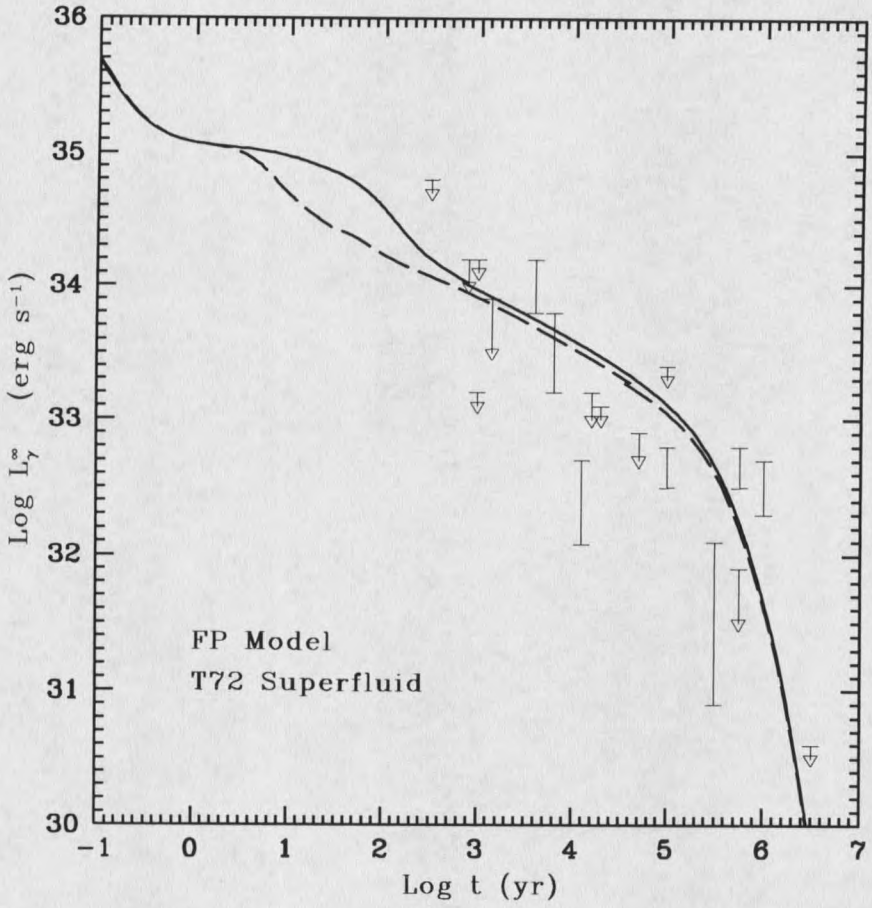

Figure 7.4: Standard cooling is shown for a $1.4M_\odot$, FP EOS star with a T72 superfluid. The solid line is the standard cooling curve. The dashed line is the standard cooling including the Cooper pair neutrino emissivity. See figure 1.1 and table 1.1 for summary of data points.

Overall, it has been seen that Cooper pair neutrino emissivity does not significantly change standard cooling for a 1.4 $M_\odot$ neutron star with T72 superfluid. Consequently, some sort of non-standard cooling must be considered in light of the new observations. The Vela detection, and the new RCW 103 upper limit, force some type of non-standard cooling scenario with superfluid suppression to be in effect.

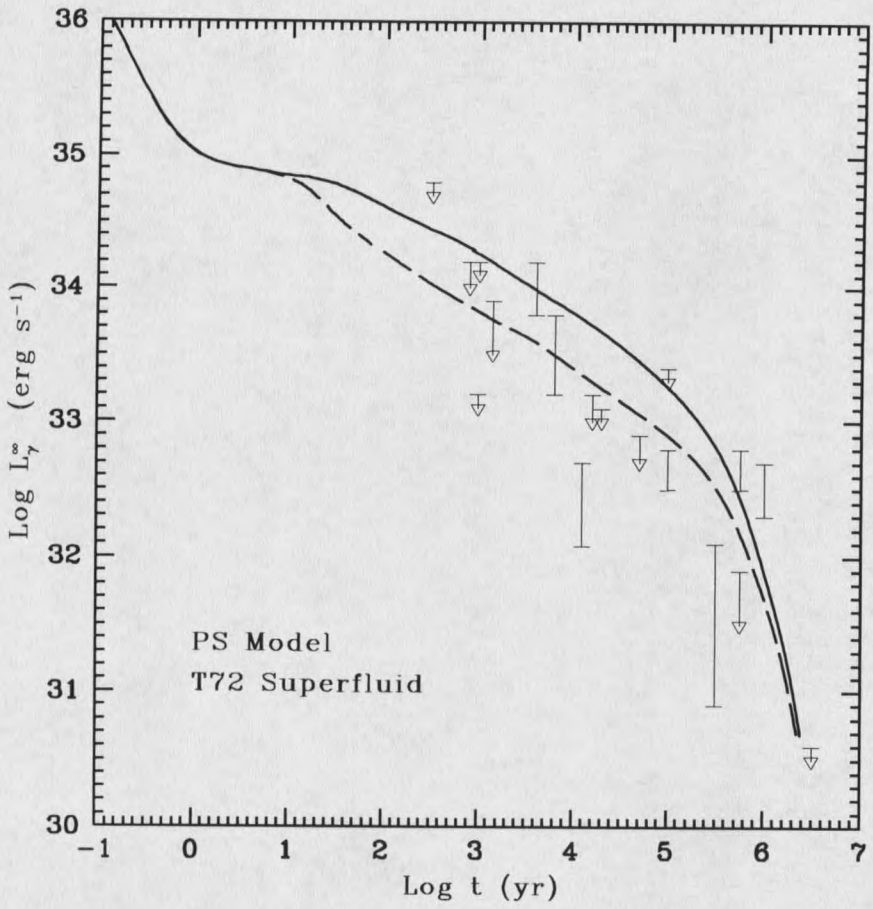

Figure 7.5: Standard cooling is shown for a $1.4M_\odot$ star with a PS EOS and a T72 superfluid. The solid line is the standard cooling curve. The dashed line is the standard cooling including the Cooper pair neutrino emissivity. See figure 1.1 and table 1.1 for summary of data points.

Effects Upon Non-Standard Cooling

For non-standard cooling, the Cooper pair neutrino emission effect upon the cooling depends upon two things. First, it depends upon the cooling mechanism. Secondly, it depends upon the superfluidity.

For the cooling mechanism, direct URCA for nucleons, pions, kaons, and hyperons are easily explained from the theoretical standpoint; however, quark direct URCA

cooling mechanisms could also exist within the core (Tsuruta 1998, and references therein). We rejected the Direct URCA process for nucleons because the effective mass at high densities affects the superfluid gap energy. Because direct URCA requires the ratio of number densities of protons to neutrons to be ~15% or more (Lattimer et al, 1991), the effective mass was found to be lower than normal neutron matter with only several percent of proton concentration (Takatsuka & Tamagaki, 1997, TT97 hereafter). Superfluid gaps have been calculated by TT97 for the direct URCA with nucleons. Their self consistent detailed calculations show that as the effective mass goes down the critical temperature for superfluidity also goes down. At the expected direct URCA densities, $\rho > \rho_{crit} \sim 2 - 3.5\rho_{nuc}$, where ρ_{nuc} is nuclear density, the effective mass of a neutron drops to $0.5\mathrm{m}_n$, while the proton effective mass goes down to $\sim 0.5\mathrm{m}_p$. At these effective masses, the critical superfluid temperatures for both protons and neutrons drop far below 10^8 K, giving no superfluid suppression for observed neutron stars which are as hot as $\sim 10^8$ K. The direct URCA emissivity would then be unaffected by the superfluid; consequently, neutron stars cooling by direct URCA for nucleons would then cool too fast to explain the observed data.

Recently several authors (Levenfish, Shibanov, & Yakovlev, 1999, Kaminker, Haensel, & Yakovlev, 2001, Kaminker, Yakovlev, & Gnedin, 2001, and Yakovlev, Kaminker, & Gnedin, 2001) calculated neutron star cooling for stars with a nucleon core where the direct URCA process can take place for densities higher than $\sim 2\ \rho_{nuc}$. By comparing their cooling curves with observational data, these authors conclude that by changing the mass all observation data can be explained, provided proton su-

perfluid critical temperature T_{cp} is sufficiently high, of the order of 5×10^9 K. However, they adopted phenomenological T_{cp} which is not supported by realistic micro-physical calculations by TT97. For instance, their selection of phenomenological T_{cp} is based on the assumption that the $^1S_0$ proton superfluid gap is the same as the $^1S_0$ neutron superfluid gap, the argument not justified from theoretical ground in a neutron dominated matter. Note that the gaps for normal nucleon matter (where number density of protons and neutrons are approximately equal) and neutron dominant matter are certainly different. This composition-dependent nature of the superfluid gaps of both protons and neutrons was completed ignored in the Kaminker, Yakovlev, & Gnedin (2001) work. Note that for neutrons, these authors adopted phenomenological T_{cn}, based on micro-physical models for neutron matter with smaller proton concentration which does not allow the direct URCA process, and hence their neutron gap also is not self-consistent.

On the other hand, TT97 did calculate both proton and neutron superfluid gaps realistically and self-consistently, by taking into account the actual density dependence of Y_p, proton concentration, as well as density dependent effective mass of both protons and neutrons. These authors adopted two extreme equations of state which allow the direct URCA process, to estimate the measure of theoretical uncertainty, both of which led to the same conclusion, that proton T_{cp} cannot be as high as 7×10^9 K. Therefore, their conclusion is model-independent. In this sense, the work by Kaminker, Yakovlev, & Gnedin (2001) only supports our conclusion that the direct URCA as a non-standard process is not an option for observed middle-aged neutron

stars.

Similar arguments can be made for kaon direct URCA. The effective mass of quasi-nucleons in a kaon condensate is lower than the effective mass for ordinary neutron matter, driving down the superfluid critical temperature below $\sim 10^8$ K (Takatsuka and Tamagaki, 1995), so we reject the kaon direct URCA. For quarks, there are still too many unknowns to say definitely as to how superfluidity can affect the cooling mechanism. Regardless, quark direct URCA without superfluidity cools too fast (Umeda, Tsuruta, & Nomoto, 1994).

The effective mass and the superfluid gap, and hence T_{cr}, for pion matter were calculated by Takatsuka and Tamagaki (1988). Both are relatively large as compared with the case for neutron matter. So using a pion superfluid model with higher T_{cr}, pion cooling should be suppressed sufficiently to explain the observed data. So for non-standard cooling, we chose pion direct URCA. For pion cooling, the degree of condensation is expressed by the Landau-Migdal (LM) parameter, $g' \equiv \tilde{g}'(f/m_\pi)^2$. This measures the degree of correlation in the spin-isospin channel, the strength of the pion-pion interaction, with typical values of 0.5 and 0.6 (Umeda et al, 1994).

For the superfluid model, initially we expected that the superfluidity would be the same as that chosen for standard cooling for ordinary neutron matter. However, the superfluidity for pion matter possesses different properties. The limits upon the superfluid will be two fold. First, the superfluid gap should be sufficient to suppress, but not eliminate, the pion cooling mechanism. Second, it should be able to explain the observed data for Vela.

Much of the superfluid work has already been done (Tsuruta 1998 for review, and references therein). For either pion model with $\tilde{g}'$=0.5 or 0.6, without superfluid suppression, 1.4 $M_\odot$ stars with the FP EOS with modification for a pion core cool to a luminosity of 10^{31} ergs s^{-1} within a thousand years regardless of the LM parameter. PS EOS stars do not even have pion cooling for 1.4 $M_\odot$, lacking the density for condensation. With superfluid suppression, 1.4 $M_\odot$ FP EOS stars evolved differently, depending upon the superfluid model chosen. The HGRR superfluid shuts down the pion cooling so effectively that it is almost indistinguishable from standard cooling. The T72 superfluid, which works well for neutron matter of standard cooling, fails to suppress much of the pion cooling mechanism. The two most promising superfluid models are the AO superfluid model, for $\tilde{g}' = 0.6$, and the E1 superfluid model, for $\tilde{g}' = 0.5$ or 0.6 (Tsuruta 1998, figure 6).

The AO superfluid suppression is insufficient to slow the rate of the pion cooling. Simulations showed that the Cooper pair emissivity for the AO superfluid model did not change the evolution significantly from the AO superfluid model without the Cooper pair effect; consequently, the AO cooling curve passes below the Vela observation by a factor of three or more. The AO superfluid in the $\tilde{g}' = 0.5$ case had already been eliminated from previous work (Tsuruta 1998), now the $\tilde{g}' = 0.6$ case has also been ruled out. Moreover, the AO superfluid model was constructed for neutron matter, not for pion matter.

Figure 7.6 shows our resulting cooling curves using pion cooling of the E1 superfluid model for the $\tilde{g}' = 0.6$ case, which is very similar to the $\tilde{g}' = 0.5$ case. In both

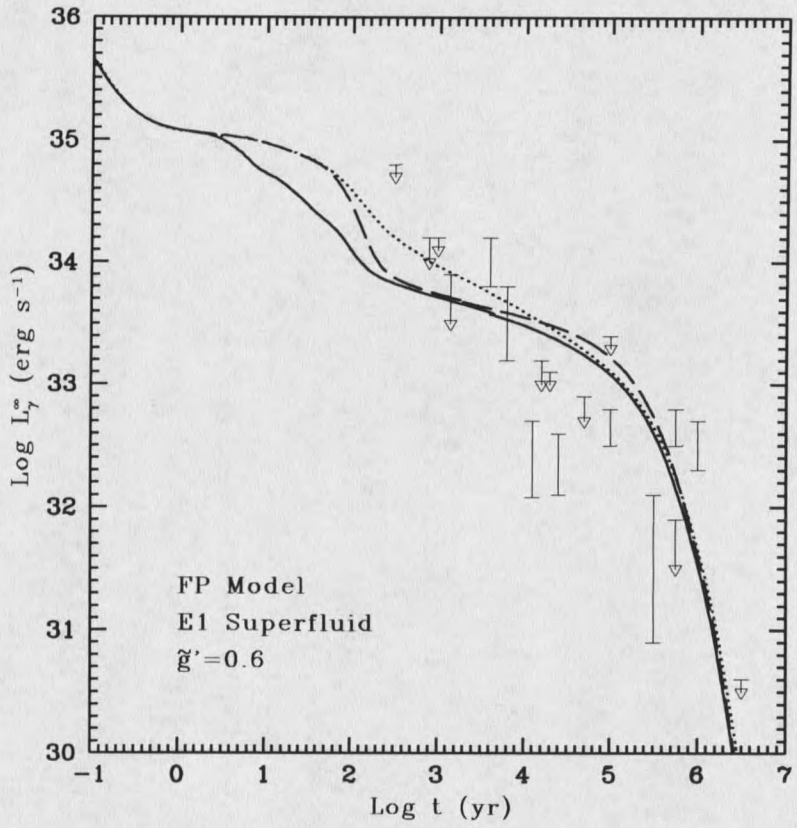

Figure 7.6: Pion cooling with E1 superfluid model a $1.4M_\odot$ star with for the FP EOS. The dotted curve is for standard cooling for a star with $1.4M_\odot$ FP EOS and a T72 superfluid model without Cooper pair emission. The dashed curve is the E1 superfluid suppression for pion cooling with the LM factor $\tilde{g}' = 0.6$ without the Cooper pair effect. The solid curve includes the effect of Cooper pair neutrino emission on pion cooling. See figure 1.1 and table 1.1 for summary of data points.

cases, the E1 superfluid suppresses the pion cooling too much to account for the Vela observation. The superfluid gap size is not accounted for by either LM factor. Since theory predicts the pion superfluid gap to lie anywhere between E1 and E2, the E1 model is reduced by a multiplying factor $10^{-\Delta T}$, using the device developed by Umeda et al. (1994). These superfluid models are known as E1-ΔT (Umeda et al., 1994). Umeda et al. (1994) detailed the effects for the superfluid gap size upon cooling for

LM factor, $\tilde{g}' = 0.5$, and pointed out that the results are similar for the $\tilde{g}' = 0.6$ case.

Using a variable gap size and including the neutrino emissivity due to Cooper pairs, figure 7.7 shows our modified cooling curves for the variable gap size. The best values for the Vela data point use a gap size of at least ΔT=0.6. This indicates that the best model uses a phase transition between nucleons and pions in the core of a neutron star, changing phase once the mass reaches the level for pions to be present in the core. Once the pions become present, the superfluid properties change, so that they efficiently suppress the neutrino emissivity. The variable gap size suggests that the two models with ΔT between 0.6 and 0.8 will explain all of the data. Figure 7.8 shows the time evolution of the neutron star temperature distribution over the stellar interior for standard and non-standard cooling. For the non-standard cooling, the distribution of temperatures refers to a $1.4M_{\odot}$ neutron star with the E1-0.6 superfluid model, from figure 7.7. The standard cooling is for the $1.2M_{\odot}$ neutron star with a T72 superfluid model from the same figure. The most important difference is the lack of the pion cooling dip in the standard case; furthermore, the temperature distribution at late times indicates that the cooling for the non-standard scenario is much quicker.

Discussion

Many superfluid models exist for neutron star densities, but some are not matched to the observational evidence, especially in light of the new observations of *Chandra* and *XMM-Newton*. The newer observational results make it possible for us to

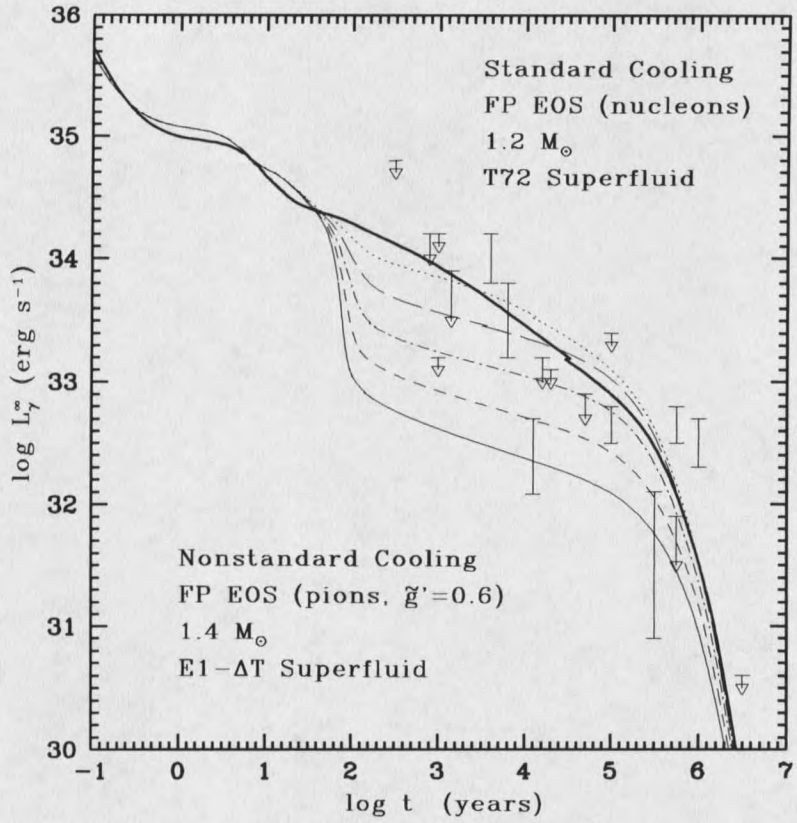

Figure 7.7: Pion cooling with the modified E1 superfluid model a star with the pion FP EOS and $1.4M_{\odot}$. The heavy solid curve is for standard cooling with a T72 superfluid and $1.2M_{\odot}$, including Cooper pair emission. The other curves are for nonstandard (pion) cooling with the LM, $\tilde{g}' = 0.6$. Each curve represents a different value of ΔT: dotted (ΔT=0), long dashed (ΔT=0.2), chain (ΔT=0.4), dashed (ΔT=0.6), and solid (ΔT=0.8).

make serious sense of the nonstandard cooling theories. With *ROSAT* only 3 isolated neutron stars had surface temperatures detected with certainty: Geminga, PSR B0656+14 and PSR B1055-52. With the opening of the new era of X-ray and optical astronomy with second generation satellite missions such as *Chandra*, *XMM-Newton*, and HST, Vela immediately joined the list of detections along with determining that it has a hydrogen atmosphere (Pavlov et al, 2001). Furthermore, the detection of the

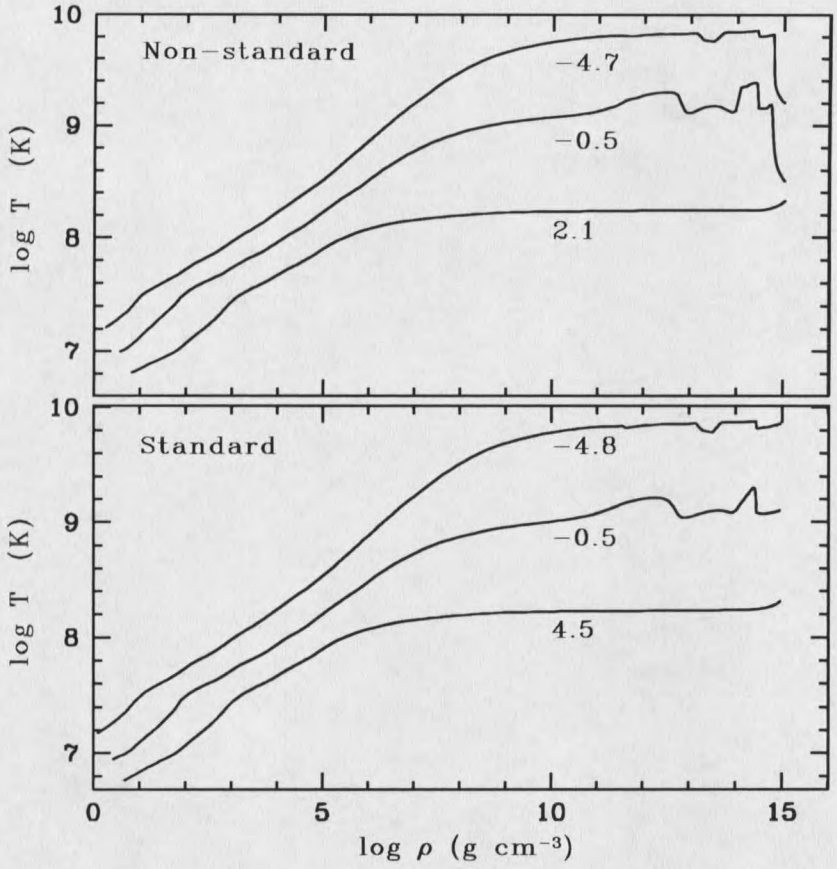

Figure 7.8: Interior temperatures of non-standard and standard cooling as a function of internal density. The labels are the age in log (years). See text for explanation.

surface temperature of 1E1207.4-5209 is certain (Zavlin, Pavlov, & Trümper, 1998), along with RX J0720.4-3125 (Haberl et al, 1997), RX J0822-4300 (Zavlin, Trümper, & Pavlov, 1999) and RX J185635-3754 (Walter, Wolk, & Neuhäuser, 1996). Furthermore, refined measurements modified the upper limits of other cooling neutron stars, as in the case with RCW 103 which had a lower limit reduced and may have had its surface temperature detected (Slane, 2001). PSR B1823-13 is another candidate which will be determined within this year by our group; it will have either its temperature measured or its upper limit will be further decreased with a 40 ks *Chandra*

observation.

The existence of Vela's low luminosity and the recent establishment of RCW 103's new upper limit, require nonstandard cooling to explain them. No other uncertainty, such as the ages of non-historical pulsars, being off by a factor of $\sim$2, will explain these data. An age uncertainty or crust heating, in the case of PSR B1055-52 and RX J185635-3754, will explain their data easily by standard cooling with heating. Thus, we require both standard and non-standard cooling to explain all the currently observed temperatures of isolated neutron stars.

The pion critical density should occur at approximately $\rho_{crit} \sim 2 - 3\rho_{nuc}$. Pion stars, neutron stars with pion cores, must have central densities exceeding ρ_{crit}. And, neutron stars must have central densities below ρ_{crit}. If the masses of binary neutron stars, $\sim 1.4 M_{\odot}$, are also to be believed as the masses for isolated neutron stars, then the EOS for the star should have a mass near $1.4 M_{\odot}$ with a central density of $\sim \rho_{crit}$.

Figure 7.9 shows the central density versus mass relations of three different EOS. The stiffest EOS shows that stable neutron stars will lack the internal density to have pions in their cores at all; consequently, EOS which are too stiff will not explain low data points such as Vela. The correct EOS has central densities that exceed ρ_{crit}. The softer EOS, such as BPS, do not match the expected masses for neutron stars, being 0.3-0.4$M_{\odot}$ near ρ_{crit} and hence should be considered questionable as a possible EOS for isolated neutron stars.

Our results suggest that the FP EOS is close to the ideal EOS. In figure 7.7, the transition from neutron to pion phase takes place for stars with mass $\sim$0.8-1.0$M_{\odot}$.

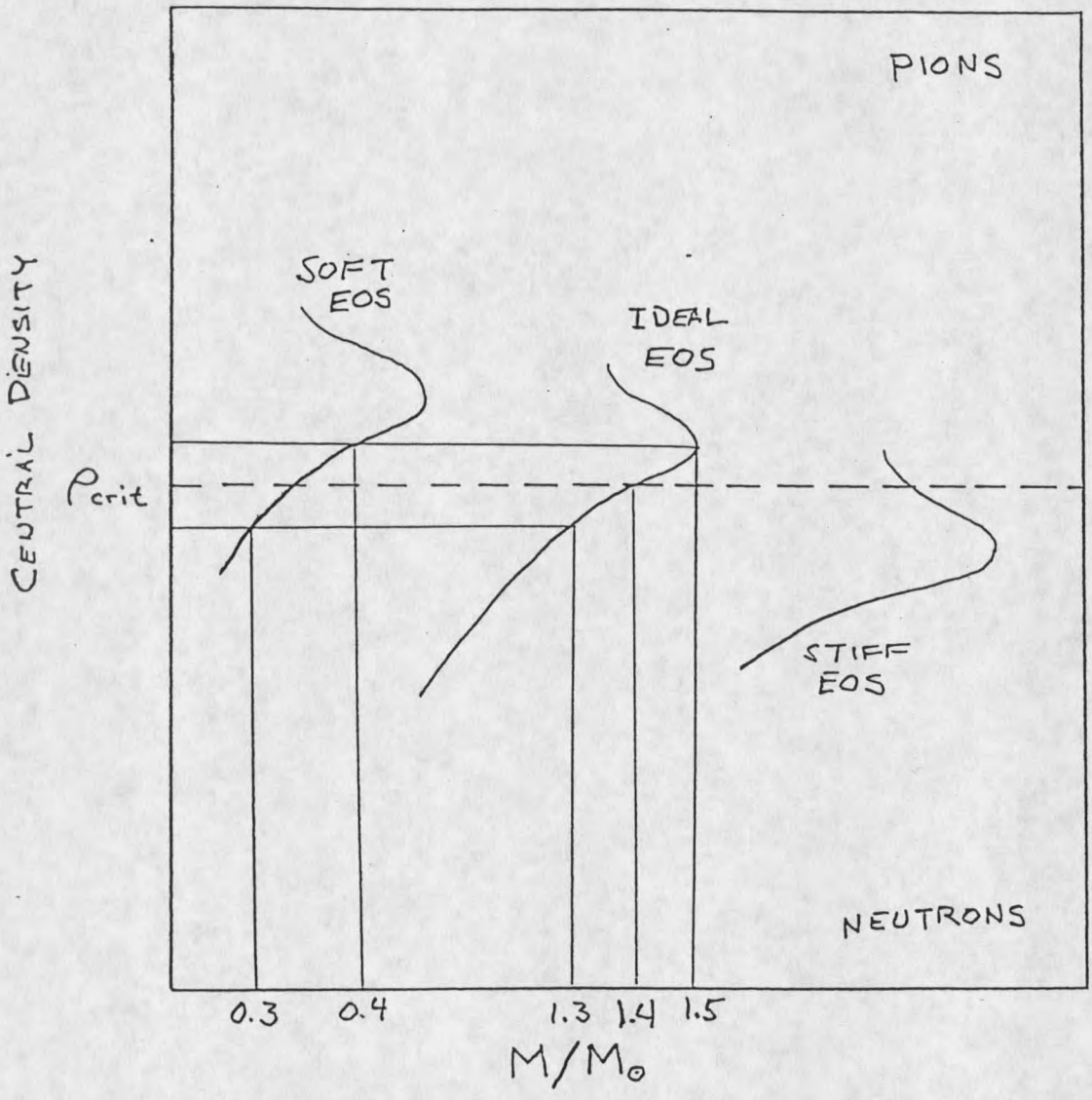

Figure 7.9: Comparisons between equations of state. The critical density for pions, ρ_{crit}, establishes the correct equation of state for neutron stars with masses near $1.4M_\odot$. EOSs become unstable when their masses begin to decrease with increasing density.

To model the effect of the transition at masses that are closer to a $1.4M_{\odot}$ neutron star, a $1.2M_{\odot}$ with a FP EOS and a neutron core and a $1.4M_{\odot}$ star with FP EOS and a pion core are used. However, the central density of a $1.2M_{\odot}$ star with the FP EOS is somewhat higher than ρ_{crit} for neutron-pion phase transition. This means that the correct EOS should be somewhat stiffer than the FP model, if the mass of an isolated neutron star is regarded as very close to $1.4M_{\odot}$.

Another possibility is the direct URCA cooling involving hyperons, which implications are still under investigation. Initial indications have shown that the hyperon EOS is softer than the FP EOS, but the effect of the hyperon direct URCA is still under investigation.

To account for all of the data, there has to be a phase change. First, the mass has to increase to the point where particles for non-standard cooling appear in the core. Secondly, the superfluid gap energy has to change from the neutron matter case when the other particles are present. The only way for the superfluid gap energy to change is for there to be a phase transition.

CHAPTER 8

SUMMARY

As pointed out in the introduction, the thermal evolution of neutron stars has become a serious observational problem, because the new generation of instruments such as *Chandra* and *XMM-Newton* has made realistic advances in measuring the surface temperature of a neutron star. We demonstrated this with the observation of three neutron stars, PSR B1055-52, SGR 1900+14, and 1E1207.4-5209, using data collected by *Chandra*. Furthermore, we applied the new results to explain a reasonable interpretation of neutron star cooling theories with cooper pair emissivity and superfluid suppressed neutrino emission processes.

From the observational standpoint, we found more details of the radio pulsar PSR B1055-52. The energy resolved light curves and pulsed fractions were used to make a clearer picture of the environment of the surface radiation and the magnetospheric radiation. From the spectroscopic standpoint, we found that no physically reasonable two component model will fit the data. We favor a three component model with two blackbody radiators and a power-law component. The coolest blackbody, of a temperature $\sim$ 70 eV, is thought to come from the whole of the neutron star surface. The range of the measured effective radius is well within expected neutron star radii

at a distance of 1 kpc. We interpret the second blackbody of higher temperature as a hot-spot associated with one of the magnetic poles. The temperature of $\sim$0.14 keV and effective radius of 1.3 km, for the hot-spot, are consistent with the earlier results. Furthermore, the power-law index, Γ=1.66, is reasonable for non-thermal magnetospheric radiation.

The phase resolved spectroscopy of PSR B1055 improved our understanding of the overall structure of the neutron star. The pulse from the hot spot is clearly seen in the phase resolved results. This, combined with the light curves, will improve the modeling for this pulsar. Already, the clear results show that there is only one hot-spot, as we found no indication of a second in either the light curve or the phase resolved spectroscopy. The phase resolved dependence of the power-law component is still uncertain, though its pulse profile is somewhat complex.

For cooling theory purposes, we find that PSR B1055-52 does not have a hydrogen atmosphere. This in itself is important, as it shows that not all isolated neutron stars have hydrogen atmospheres. Furthermore, the blackbody temperature measured with *Chandra* has not significantly moved the data point on the cooling curves. Without the hydrogen atmosphere, PSR B1055-52 has to be explained as well as the lower temperature hydrogen atmosphere cases such as Vela, within the context of a reasonable cooling theory.

Our results for the *Chandra* observation of SGR 1900+14 are less spectacular than those for PSR B1055-52, but are interesting nonetheless. Though not conclusive, the energy resolved pulsed fraction indicate that there might be some complex behavior

associated with the burst that disappears by the second observation. Furthermore, the second observation's shorter duration might have made this feature disappear into the noise. Timing results have shown that SGR 1900+14 has a complex timing history since the 1998 outburst, as our period derivative found for the 2001 observations do not predict the periods of the 1998 observations, or vice versa.

The radiation from SGR 1900+14 is mostly magnetospheric in origin, as a non-thermal power-law model fits the data well. The photon index, however, is inconsistent with non-thermal magnetospheric radiation. Because of this, we prefer a two component blackbody plus power-law model. The blackbody temperature is 0.5 keV and the radius is 1.3-1.9 km. Even with this model, the non-thermal magnetospheric component is still dominant, though its index more consistent.

Our phase resolved results for SGR 1900+14 are inconclusive because of poor counting statistics. A single power-law model pulses with varying indexes for the first observation, but does not for the second, using a simple two phase binning. The results for the blackbody plus power-law model are inconclusive, as we could not find any variation within the error of the parameters.

Our initial results for the radio quiet pulsar 1E1207.4-5209 are much more exciting. First, the absorption feature at 1.25 keV is very interesting. If it is confirmed by the next *Chandra* observation, a detailed analysis of its nature will be required. Our spectral results, accepting that the absorption edge exists, show that the blackbody temperature is consistent with earlier combined *ROSAT* and *ASCA* results by Zavlin, Pavlov and Trümper (1998). We conclude that 1E1207.4-5209 has a hydrogen

atmosphere.

Our phase resolved results are also very interesting. The variation of the bolometric flux of the surface emission with phase has a ~7% pulsed fraction. The small uncertainties for the bolometric flux are encouraging, allowing the improvement of the phase resolution with more phase bins. Also, phase resolved spectroscopy should also produce very interesting results for the hydrogen atmosphere model.

Finally, the new results for Vela and RCW 103 have made the case that standard cooling alone is insufficient to explain all of the observed neutron stars. Our cooling calculations including Cooper pair emissivity have shown that we require pion cooling with superfluid suppression to explain these new observational results.

Our first key point is that some lower mass neutron stars will not have pions in their cores and thus will have to be explained by standard cooling scenarios. Higher mass neutron stars, on the other hand, will have the pions present and thus have different cooling mechanisms. Our results placed a constraint on the EOS, assuming that the masses of isolated neutron stars are consistent with the measured mass of neutron stars, $\sim 1.4 M_{\odot}$, in binary systems. The EOS will be stiffer than medium, but it will not be as stiff as the PS model. Soft equations of state, like the BPS model, will be unlikely because the masses of the stars near the point where the transition between neutron and pion cores takes place too low, 0.2-0.3$M_{\odot}$.

Our next key point is that one superfluid model will not explain both the cooling for hotter and cooler neutron stars. For the superfluid gap energy to change, there has to be a phase change to accompany it. Without such a phase change, changing

the gap energy is unphysical. The phase change is easily explained by the transition from neutron cores to pion cores with an increase of central density and hence mass.

To explain the data, pion cooling has to be used with superfluid suppression. We used a modified E1 superfluid model using an adjustable gap energy, ΔT, to find the range where the data of Vela and RCW 103 could be explained. A value of $\Delta T \sim 0.6$-0.8 works well. Consequently, data that lies between the standard and non-standard cooling curve with superfluid suppression are assumed to have masses that are between 1.2 and $1.4 M_{\odot}$ for the FP EOS.

Hyperon cooling is still unknown, but if our initial findings of the hyperon EOS as being too soft is true, then the picture presented in chapter 7 is a reasonable and simple explanation of neutron star cooling based upon the current data.

Future observation will constrain the picture even further, giving smaller uncertainties to the observed parameters. Currently, Vela is the lower limit for the non-standard cooling scenarios, but as more detections are made that lie off the standard cooling line, more constraints will be placed upon the superfluid model that explains the data. Essentially, the neutron star offers itself as a site for exciting experiments in high energy physics done by nature where the observer has the opportunity to determine the details by measuring its surface temperature.

BIBLIOGRAPHY

BIBLIOGRAPHY

Allen, G. 2000, private communication.

Amunddsen, L. and Ostgarrd, E., Nucl. Phys. A, **442** (1985) 163.

Australian Pulsar Timing Data Archive, (www.atnf.csiro.au/research/pulsar/archive/)

Baym, G., Pethick, C., and Sutherland, P., ApJ, **170** (1971) 299.

Becker, W., PhD Thesis, Max Plank Institut für Extraterrestrisch Physik, (1995).

Biggs, J. D., MNRAS, **246** (1990) 341.

Bremer, M., GCN GRB Observation Report Number **1049** (2001).

Brinkman, W. and Ögelman, H., A&A, **182** (1987) 71.

Brown, G. E., Weingartner, J., C., & Wijers, R., ApJ, **463** (1996) 297.

Chakrabarty, D., et al., ApJ, **458**(2001) 800.

Chandra Proposers Observatory Guide Version 3.0 (2000).

Cheng, A. F., and Helfand, D. J. ApJ, **271** (1983) 271.

Chandra Data Products Guide,
asc.harvard.edu/ciao/download/doc/data_products_guide/event_descrip.html (2001).

DeDeo, S., Psaltis, D., and Narayan, R., astro-ph/0004266 (2001).

Duncan, R. C., astro-ph/0106041 (2001).

Feroci M., et al., GCN GRB Observation Report Number **1055** (2001).

Finley, J. P., Srinivasan, R., and Park, S., ApJ, **466** (1993) 938.

Flowers, E., Ruderman, M., and Sutherland, P., ApJ, **205** (1976) 541.

Fox, et. al., astro-ph0107520 (2001).

B.,Friedman, and V. R., Pandharipande, Nucl. Phys. A, **361** (1981) 502.

Friman, and Maxwell, ApJ, **232** (1979) 541, FM79.

Frontera, F., et al., GCN GRB Observation Report Number **1041** (2001).

Gotthelf, E. V., and Vasisht, G., (2000) in ASP Conf. Ser. 202, Pulsar Astronomy–2000 and Beyond, ed. M. Kramer, N. Wex, & R. Wielebinski (San Francisco: ASP), 699.

Greiveldinger, et al., ApJ, **465** (1996) L35, G96.

Greenstien, G., and Hartke, G. J., ApJ, **271** (1983) 283.

Haberl, F., et al., A&A, **362** (1997) 662.

Halpern, J. P., and Ruderman, M., ApJ, **415** (1993) 286.

Heyl, J. S., and Hernquist, L., ApJ, **491** (1997) L95.

Hoffberg, M., et al., Phys. Rev. Lett., **24** (1970) 775, HGRR.

Hurley, K., et al, ApJ, **510** (1998) L111.

Hurley, K., et al, astro-ph/9811388 (1998c).

Hurley, K., astro-ph/9912061(1999)

Hurley, K., et al., GCN GRB Observation Report Number **1043** (2001).

Itoh, N., and Kohyama, K., ApJ, **275** (1983) 858.

Iwamoto, N., Ann. Phys., **141** (1982) 1.

Kaminker, A. D., Haensel, P., & Yakovlev, D. G., A&A, **373** (2001) L17.

Kaminker, A. D., Yakovlev, D. G., & Gnedin, O. Y., astro-ph/0111429 (2001).

Klose, et al., GCN GRB Observation Report Number **1044** (2001).

Kouveliotou, C., astro-ph/0107170 (2001).

Kulkarni, S., R., et al., preprint (2000).

Larson, M. B., and Link, B., ApJ, **521** (1999) 271L.

Lampton, M., Margon, B., and Bowyer, S., ApJ, **208** (1976) 177.

Lattimer, et al., Phys. Rev. Lett., **66** (1991) 2701.

Levenfish, K. P., Shibanov, Y. A., & Yakovlev, D. G., Astron. Lett., **25**, 417.

Lynn, A. G., and Manchester R. N., MNRAS, **234** (1988) 477.

Mereghetti, S., and Stella, L., ApJ, **442** (1995) L17.

Mereghetti, S., Bignamai, G. F., and Caraveo, P. A., ApJ, **464** (1996) 842.

Mignani, R., Caraveo, P. A., and Bignami, G. F. ApJ, **474** (1997) L52.

Munakata, H., Kohyama, Y., and Itoh, I., ApJ, **296** (1985) 197.

Muto, T., et al., Prog. Theor. Phys. (Suppl. No. 112) Ch. 8, (1988) 221.

Nishizaki, S., Takatsuka, T., & Hiura, J., Prog. Theor. Phys., **86** (1991) 853.

Nomoto, K., and Tsuruta, S., ApJ, **250** (1981) L19.

Nomoto, K., and Tsuruta, S., ApJ, **305** (1986) L19.

Ögelman, H., and Finley, J. P., ApJ, **413** (1993) L27, OF93.

Page, D., PhD Thesis, Stony Brook (1990).

Page, D., and Sarmiento, A., ApJ, **473** (1996) 1067.

Page, D., In the Many faces of Neutron Stars, R. Buccheri et al., eds. (1998).

Pandharipande, V. R., Pines, D., & Smith, R. A., ApJ, **208** (1976) 550.

Pavlov, G. G., et al., A&A, **289** (1994) 837.

Pavlov, G. G., et al., ApJ, **531** (2000) L53.

Pavlov, G. G., Zavlin, V. E., & Trümper, J., ApJ, **511** (1999) L45.

Pavlov, G. G., et al., ApJ, **552** (2001a) L129.

Pavlov, G. G., et al., in preparation, (2001b).

Perna et al., astro-ph/0103273 (2001).

Romani, R., W., ApJ, **313** 1987 718.

Slane, P., Presentation at 2 years of Science with *Chandra* Symposium (2001).

Takatsuka, T., Prog. Theor. Phys., **48** (1972) 1517, T72.

Takatsuka, T., and Tamagaki, R., Prog. Theor. Phys., **64** (1980) 2270, TT80.

Takatsuka, T., and Tamagaki, R., Prog. Theor. Phys., **67** (1982) 1649, TT82.

Takatsuka, T., and Tamagaki, R., Prog. Theor. Phys., **94** (1995) 457.

Takatsuka, T., and Tamagaki, R., Prog. Theor. Phys., **97** (1997) 345, TT97.

Tatsumi, T., Prog. Theor. Phys. Suppl., **120** (1995) 111.

Tatsumi, T., Prog. Theor. Phys., **80** (1988) 22.

Tennant, A., wwwastro.msfc.nasa.gov/xray/ACIS/cctime (2001).

Thompson, D. J., et al., ApJ, **516** (1999) 297.

Thompson, C., and Duncan, R., C., ApJ, **473** (1996) 322.

Tsuruta, S., Phys. Rep., **56** (1979) 237.

Tsuruta, S., Phd Thesis, Columbia Unviversity (1964).

Tsuruta, 1998, Phys. Rep., **292** (1998).

Tsuruta, S., and Teter, M. A., in Relativistic Astrophysics: 20th Texas Symposium, J. C. Wheeler and H. Martel eds. (2001) 507.

Tuohy, I. R., and Garmire, G. P., ApJ, **239** (1980) L107.

Vesisht, G., ApJ, **476** (1997) L43.

Ulmer, M. P., ApJ Suppl., **90** (1994) 789.

Umeda, H., et al., ApJ, **408** (1993) 186.

Umeda, H., et al., ApJ, **431** (1994) 309.

Umeda, H., Tsuruta, S., & Nomoto, K., ApJ, **433** (1994) 256.

Umeda et al., ApJ, **543** (2000) L193.

Walter, Wolk, Neuhäuser, Nature, **379** (1996) 233.

Wang, F. Y.-H., et al., ApJ, **498** (1998) 373, W98.

Weiler, E., presentation at 2 years of Science with *Chandra* Symposium (2001).

Wiringa, R. B., Fiks, V., & Fabrocini, A., Phys. Rev. C, **38** (1988) 2518.

Woods, P. M., et al., astro-ph/9907173 (1999).

Yakovlev, D. G., Kaminker, A. D., & Levenfish, K. P., A&A, **343** (1999) 650.

Yakovlev, D. G., Kaminkar, A. D., & Gnedin, O. Y., A&A, **379** (2001) L5.

Zavlin, V. E., Trümper, J., & Pavlov, G. G., ApJ, **525** (1999) 959.

Zavlin, V. E., Pavlov, G. G., & Trümper, J., A&A, **331** (1998) 821.

Zavlin, V. E., et al., ApJ, **540** (2000) L25.